Directed and Elliptic Flow in Au + Au Collisions at a Center of Mass Energy of 19.6 GeV Per Nucleon-Nucleon Pair

By
Michael George Anderson
B.A. (University of California, Davis) 1995
M.S. (University of California, Davis) 1998

DISSERTATION
Submitted for partial satisfaction of the requirements for the degree of
DOCTOR OF PHILOSOPHY
in
Physics
in the
OFFICE OF GRADUATE STUDIES
of the
UNIVERSITY OF CALIFORNIA
DAVIS

Approved:

_____

_____

_____

Committee in Charge
2006

Abstract

The STAR experiment analyzes the results of nucleus-nucleus collisions at the RHIC facility at Brookhaven National Laboratory. The STAR detector is mainly composed of a solenoidal Time Projection Chamber that was designed to provide wide coverage of the resulting outgoing particles. Over a 24-hour period on November 25th and 26th of 2001, the RHIC facility ran a Au + Au collider beam with a center of mass energy of 19.6 GeV per nucleon-nucleon pair. This dissertation examines directed and elliptic flow measurements at this energy and compares the results to experiments run at similar energies. A discussion of the analysis methods, along with the event and track quality requirements, are included in this paper.

Acknowledgements

I would like to thank everyone who has helped me over the many, many years that I have been working on this dissertation. First of all, I would like to thank Dr. Daniel Cebra for giving me countless opportunities and plenty of moral support. I would also like to acknowledge Dr. James Draper for spending many hours helping me to understand the basis of heavy-ion physics. Dr. F. Paul Brady first gave me a chance to study in this field by mentoring me during my undergraduate time; for that I owe him a great deal.

I would like to thank the STAR collaboration in general for many years of help and understanding. I would like to thank Dr. Spencer Klein for treating me with respect and allowing me to give my input on his projects. Special thanks to Alexei Lebedev for keeping me company and giving me advice while I was at BNL in New York. I would also like to thank Dr. Howard Wieman for all of his help and encouragement. In particular, I would like to acknowledge Dr. Blair Stringfellow, for teaching me all there is to know about the STAR detectors.

I would like to thank all of those that encouraged me over the years while I was taking breaks from research. Dr. Wendell Potter gave me more lecturing opportunities than I deserved and for that I am eternally grateful. I would like to thank the Lockheed-Martin employees, especially Blue Crew, for helping me out when I needed it. I am very thankful to the American River College Physics Department for giving me a chance to pursue my dream. I would like to thank Dr. Charles DeLeone and Dr. Patrick Len for always making sure that I saw the big picture.

Suzette Wright, thank you for always being there for me. I will be forever grateful to Brooke Haag for her unyielding support and love during these trying times. Yo quireo dar muchas gracias a mi abuela, Emilia Gonzalez, para todo su amor. My family, (Rebecca Anderson, Olga Anderson and Thomas Anderson) have been very understanding and have kept my dreams possible with their unwavering support.

Table of Contents

Table of Contents

Table of Contents

List of Figures

List of Figures

List of Figures

List of Figures

List of Figures

List of Tables

Chapter Five: Results

Chapter 1

General Introduction

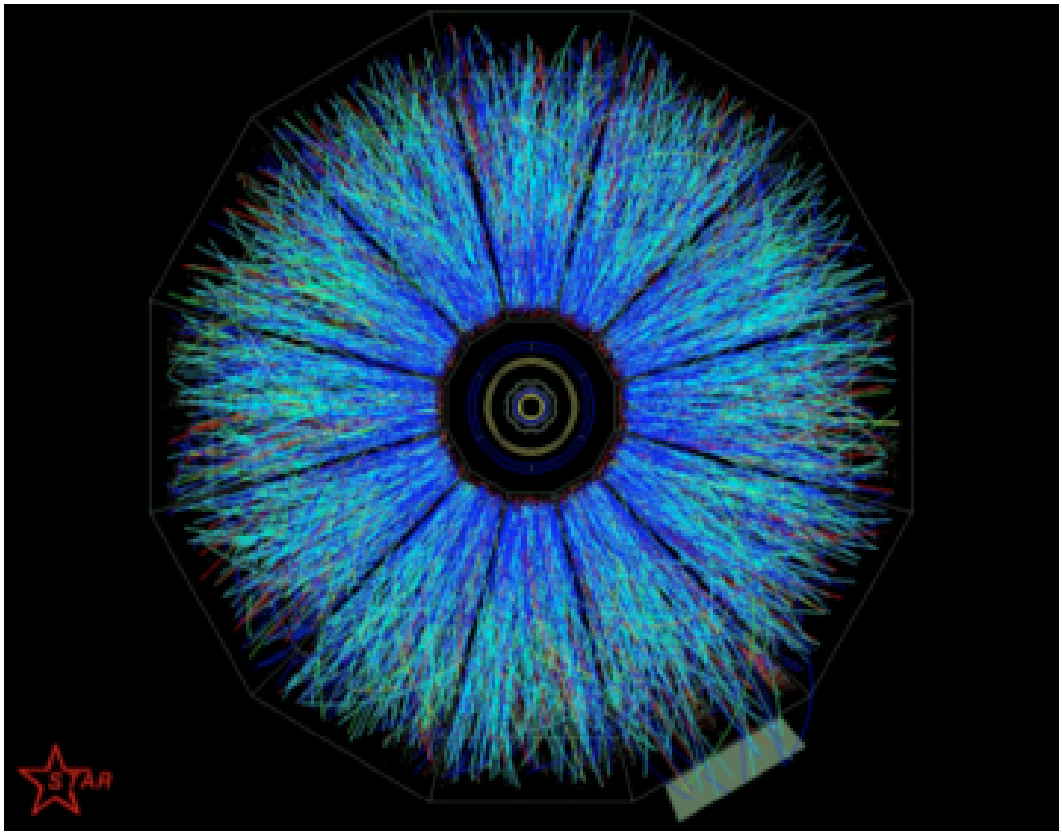

Figure 1.1: An end view of a collision in the STAR TPC [STAR 2006].

1.1 Overview of High Energy Goals

Scientists have spent countless years breaking matter into its basic forms; from molecules to atoms and nuclei to nucleons. We have explored matter with amazing advances in technology and the use of probes ever decreasing in size and ever increasing in energy. The next step for nuclear scientists is to discover and explore the nearly unbound quark. In order to study nearly free quarks, we must create an environment with extreme temperatures and densities. Highly relativistic collisions between nuclei present the opportunity to create such an environment due to the enormous amount of energy that can be deposited by the participants of the collision [Bjorken 1983].

The conditions created in relativistic heavy ion collisions (an example of such a collision is pictured in Figure 1.1 on the previous page) are close to those that existed immediately following the Big Bang, where the universe was a dense sea of unbound quarks and gluons known as the Quark-Gluon Plasma (QGP) [Ludlam and McLerran, 2003]. Figure 1.2 on the following page shows the various phases of nuclear matter depending on the temperature and baryon density. During the Big Bang, the universe cooled off quickly changing the QGP into normal nuclear matter that we observe today. In heavy-ion collisions we attempt to increase both temperature and density in order to achieve quark deconfinement. Neutron stars, on the other hand, are very dense (about five times as dense as normal nuclear matter) and relatively low in temperature.

Identification of a QGP state of nuclear matter is an important goal of high-energy nuclear physics, however we can also learn a great deal about other disciplines by studying high-energy nuclear collisions. The Equation Of State (EOS) is important to understanding the nature of nuclear matter. The compressibility of nuclear matter is an aspect of the EOS, about which we can learn more.

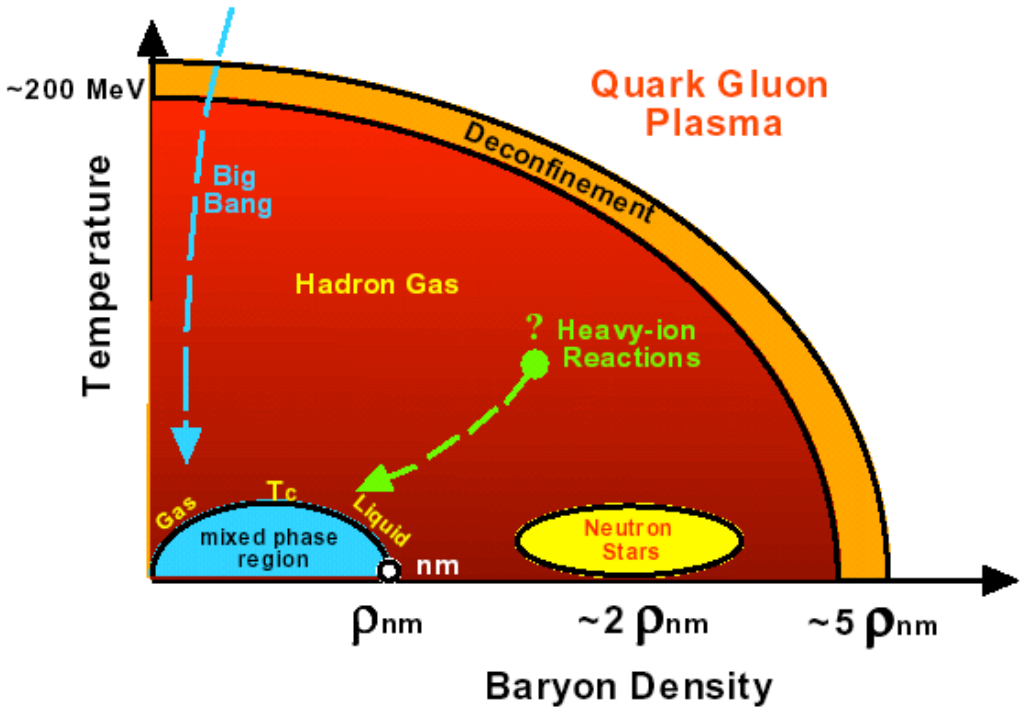

Figure 1.2: The phase diagram of nuclear matter [Wood 1998].

1.2 The Meaning of "Flow"

The result of a relativistic heavy ion collision is highly compressed, hot dense matter. Flow measures the collective motion and the bulk properties of this matter as it responds and expands to a cooler, less dense phase following the initial compression.

Figure 1.3, on the following page, shows a typical heavy-ion collision about to occur (side view). The projectile nucleus is defined to move in the +z direction as it moves toward the target nucleus. The impact parameter vector, $\vec{b}$, is defined as the perpendicular distance from the center of the target nucleus to the projectile nucleus' velocity vector. The direction of the impact parameter is defined to be the +x direction. The reaction plane, which is defined by the projectile velocity vector and the impact parameter vector, is thereby constrained to be in the x-z plane. Collisions with high impact parameters are said to be peripheral collisions, while collisions with low impact parameters are said to be central collisions

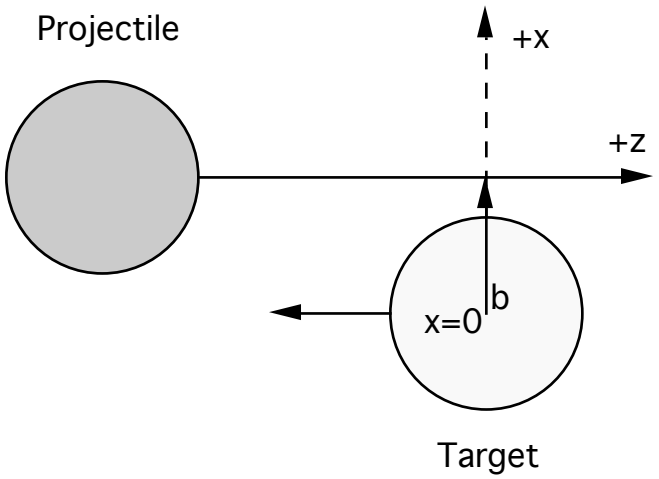

Figure 1.3: A heavy-ion collision about to occur (side view).

Figure 1.4, below, shows a typical heavy-ion collision occurring (head-on view). As the target (moving out of the page in the –z direction) and projectile (moving into the page in the +z direction) nuclei now collide, we see an almond shaped interaction region of nucleons known as the "participants" as we now look at the x-y plane. The nucleons

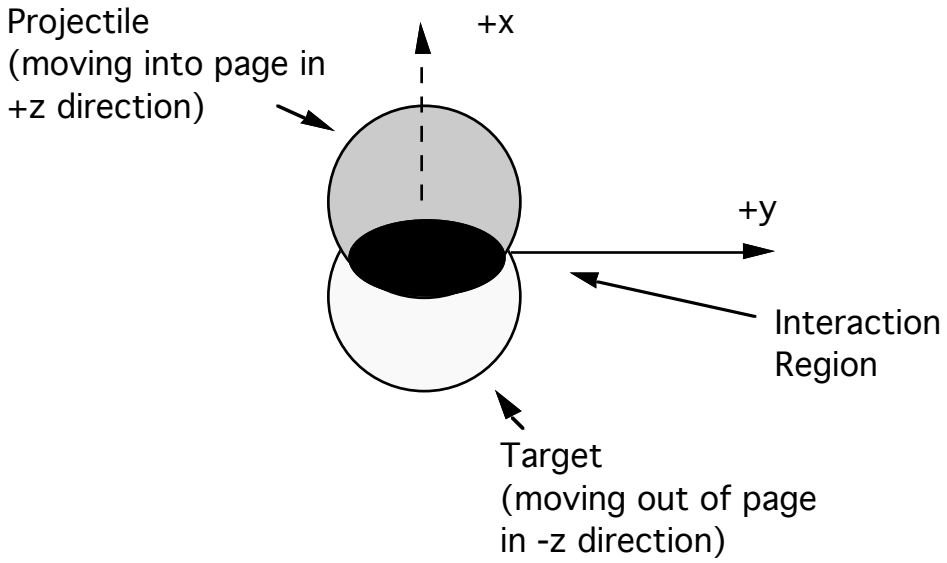

Figure 1.4: A heavy-ion collision occurring (head-on view).

in the target and projectile nuclei that do not directly interact with each other are known as "spectators."

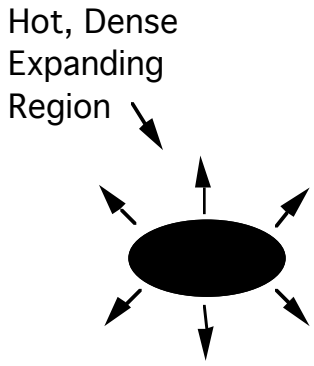

Figure 1.5: A heavy-ion collision aftermath.

Figure 1.5, above, shows the time immediately following the typical nuclear collision with the spectators now out of the picture. The hot, dense interaction region begins to expand. The compression and resulting expansion in the interaction region produces a collective "flow" of particles. There are four types of particle flow terms: longitudinal, radial, directed and elliptical. Longitudinal flow is the flow of particles along the beam direction (z direction). Radial flow is an azimuthally symmetric overall flow measurement. Directed and elliptic flows measure the azimuthal asymmetry of the particle distribution (which are together known as transverse flow).

Rescattering within the interaction region's almond shaped spatial anisotropy will give rise to a momentum anisotropy that may be observed. We may examine this momentum anisotropy by performing a Fourier decomposition of the momentum space particle distribution in the x-y plane [Ollitrault 1993]. This gives us the following equation

$$\frac{dN}{d(\Delta\phi)} \propto 1 + 2v_1\cos\Delta\phi + 2v_2\cos\left[2(\Delta\phi)\right] + \ldots$$

where N is the number of particles, v_1 (the first Fourier coefficient of anisotropy) is known as directed flow, v_2 (the second Fourier coefficient of anisotropy) is known as elliptic flow, and $\Delta\phi$ is the angle between flow of particles and the reaction plane. This thesis will examine both directed and elliptic flow.

1.3 How Studying Flow Addresses High Energy Goals

Directed and elliptic flows are important observables for investigating the QGP. Directed flow is caused by the pressure built up between the colliding nuclei during the time of their mutual overlap [Kolb 2000]. The affected particles leave the interaction region rather quickly. Thus, directed flow is sensitive to the earliest collision stage. Directed flow becomes small at higher energies due to a decrease in the transition time between the two colliding nuclei [Zhang 1999].

Thus, at higher energies it is easier to study elliptic flow [Ollitrault 1993]. At higher beam energies the projectile and target spectators rapidly leave the interaction region, leaving it to freely expand without hindrance. The total elliptic flow signal becomes interplay between the time the spectator passes and the expansion time of the dense interaction region [Soff 1999].

Elliptic flow is probably the most direct signature of QGP formation at the Relativistic Heavy-Ion Collider (RHIC) [Shuryak 2002]. Elliptic flow, in particular, has been recognized as being particularly sensitive to the early stages of a collision [Kolb 2000], so it is a measure of early time thermalization, well before hadronization has occurred. In a given collision, elliptic flow is self-quenching (*i.e.* it shuts itself off). This is because the pressure gradient is greater in the reaction plane direction as opposed to perpendicular to the reaction plane. As the transverse shape becomes more circular, this pressure gradient difference vanishes and the flow ceases.

1.4 Different Signatures of the Quark-Gluon Plasma

It is highly unlikely that the QGP will be unquestionably revealed by one unique signature. The revelation of QGP formation may need many observables verifying each other in order to be confirmed. Thus, it is important to familiarize ourselves with some of the different signatures of the QGP other than transverse flow.

J/ψ suppression is a signature of the QGP [Matsui 1986]. A J/ψ is a particle that is composed of a charm quark and an anti-charm quark in a bound state. When the J/ψ is placed in a QGP, the unbound quarks and gluons will cause Debye screening between the two quarks, thereby reducing their attraction and causing the particle to lose its bound state [Wong 1994]. Thus, a collision that creates the QGP should have fewer J/ψ particles than an identical collision that does not create the QGP. In addition, J/ψ production cross sections are directly calculable via perturbative Quantum ChromoDynamics (pQCD) methods. The observed cross section can test directly for the existence of the QGP. Experimental observations of an anomalous J/ψ suppression in ^{208}Pb +^{208}Pb collisions by the NA50 Collaboration have aroused interest [Gonin 1996]. Yet, there are also other absorption processes for the J/ψ particle that take place in normal hadron matter that hinder J/ψ particle creation [Vogt 1991]. The existence of the QGP in a collision will lead to more "open charm" mesons such as the D meson (composed of either a charm quark and an anti-up quark, a charm quark and an anti-down quark, an anti-charm quark and an up quark, or an anti-charm quark and a down quark).

Strange/anti-strange quark production is another predicted signature of creation of the QGP [Rafelski 1982]. Normal ground state nuclear matter contains no net strangeness, although there may be some strange and anti-strange quark content in the sea quarks. In high-energy nuclear collisions, some energy of the collision will go toward producing strange quarks (along with up, down, and charm quarks; as well as bottom and top quarks at increasingly small cross sections). A hadron gas (at about T = 200 MeV) should have a strangeness content of about 0.2, meaning that the number of strange and

anti-strange quarks produced is about twenty percent of the total down, anti-down, up, and anti-up quarks produced [Wong 1994]. In a QGP that has reached chemical equilibrium, the density of the three light (up, down, and strange) quarks should be nearly equal. This will lead to more strange quarks created compared to the hadron gas [Wong 1994]. Thus, strange/anti-strange quark production should be a signal for the creation of the QGP. To determine the strangeness content, most experiments measure particle yields, such as K^+/π^+ ratios (with K^+ having quarks: $u\bar{s}$, and π^+ having quarks: $u\bar{d}$). A particularly sensitive signal is the production of multi-strange baryons such as Ω^- (sss) or Ξ^o (uss) [Caines 2002], [Suire 2003], [Manzari 2003].

The energy spectrum of direct photons is yet another signature of creation of the QGP [Shuryak 1978]. Direct photons are photons produced in the early stages of the collision. They are very valuable in determining initial conditions of the process. Unlike hadrons formed in the collision, photons, which only interact electromagnetically, have a low probability of interacting with the surrounding material [Kapusta 1991]. A QGP will have photons characteristic of a greater temperature than the photons from the later hadron gas [Wong 1994]. Unfortunately, there are many sources of photons, such as π^o decays, η decays, annihilation processes, Bremsstrahlung, and Compton processes which can contribute to the overall yield in a nuclear collision [Wong 1994]. This leads to a rather large background that must be identified and subtracted from the direct photons, which increases the error of the process significantly. There have been many recent direct photon measurements trying to find the QGP [Lebedev 2002], [Johnson 2003]. Results [Bathe 2005] are consistent with Next-to-Leading-Order (NLO) pQCD calculations at high transverse momentum (p_T).

As normal nuclear matter transitions over to the QGP, a softening of the EOS will occur leading to a prolonged system lifetime and an expanded radius [Rischke 1996], [Bass 1999]. We can measure this enlarged source size through pion interferometry. This technique was developed by Hanbury-Brown and Twiss in 1956 to measure the

angular diameter of a star using the correlation between two photons (bosons) [Hanbury-Brown 1956]. Hanbury-Brown and Twiss measured one photon at one detector and compared it to an identical photon at another detector. A correlation was found with width depending on the diameter of the source due to interference between the photons' intensity [Wong 1994]. This correlation is known as the Hanbury-Brown-Twiss (HBT) effect. The theory of coherent states [Glauber 1963] identifies chaotic sources (sources with particles created in random phases) as exhibiting HBT correlations and coherent sources as not exhibiting HBT correlations. The emission of pions from a high energy, heavy ion collision can be considered a partially chaotic source [Wong 1994]. Three separate, orthogonal radius measurements (R_{out}, R_{side}, R_{long}) are made by examining the momentum differences (Δp_{out}, Δp_{side}, Δp_{long}) of two bosons. Thus, two boson HBT correlations can be used to deduce the pion-emitting source size and lifetime in heavy ion collisions. A system's chaoticity can be measured using three-boson HBT; verifying two boson results [Willson 2002]. One of the main and most interesting discrepancies between conventional theory and experiment is the collision energy independence of HBT radii. In spite of this and other anomalous results, there remains confidence in the method [Adams 2003], [Enokizono 2003], [Lisa 2005].

1.5 Experiment Overview

A key component to this work will be to compare the results of this work to results in other experiments. We should familiarize ourselves with the other main high energy heavy ion experiments, which have made measurements of flow.

1.5.1 SPS Experiments

The Super Proton Synchrotron (SPS) is an accelerator at CERN. It is able to accelerate Lead (Pb) ions up to 158 AGeV, leading to fixed target ^{208}Pb + ^{208}Pb collisions with center of mass energies of $\sqrt{S_{NN}}$ = 17.2 GeV (GigaElectronVolts). Many

experiments there studied the collective effects of collisions. Although the SPS can accelerate various species, all of the center of mass energies quoted in this sub-section are for ^{208}Pb +^{208}Pb collisions.

NA49 is a fixed target experiment that consists of four Time Projection Chambers (TPC), two large dipole magnets, Time-Of-Flight (TOF) detectors, calorimeters, and scintillators [Afanasiev 1999]. NA49 studied both directed and elliptic flow of charged pions and protons at $\sqrt{S_{NN}}$ = 8.7 GeV and $\sqrt{S_{NN}}$ = 17.2 GeV [Alt 2003].

NA50 is a fixed target experiment that consists of a muon spectrometer, an ElectroMagnetic Calorimeter (EMC), a Zero Degree Calorimeter (ZDC), a silicon microstrip multiplicity detector, and a beam hodoscope [Abreu 1997]. NA50 studied both directed and elliptic flow at $\sqrt{S_{NN}}$ = 17.2 GeV [Abreu 2001].

CERES is a fixed target experiment that consists of a spectrometer, two Ring Imaging Cherenkov (RICH) detectors, two silicon drift detectors, and a TPC [Agakichiev 1996]. CERES studied elliptic flow of charged particles at $\sqrt{S_{NN}}$ = 17.2 GeV [Slivova 2003].

WA98 is a fixed target experiment that consists of a Plastic Ball (a 655 detector module sphere that encloses the target region), silicon drift detectors, avalanche chambers, two time-of-flight detectors, pad chambers, streamer tubes, photon multiplicity detectors, and multiple calorimeters [Aggarwal 1996]. WA98 studied both directed and elliptic flow of positively charged pions and protons at $\sqrt{S_{NN}}$ = 17.2 GeV [Schlagheck 1999].

1.5.2 AGS Experiments

The Alternating Gradient Synchrotron (AGS) is an accelerator at Brookhaven National Laboratory (BNL). It is able to accelerate Gold (Au) ions up to 10.8 AGeV/c, leading to fixed target ^{197}Au +^{197}Au collisions with center of mass energies of $\sqrt{S_{NN}}$ = 4.86 GeV. Many experiments studied the collective effects of the collision.

Although the AGS can accelerate various species, all of the center of mass energies quoted in this sub-section are for ^{197}Au +^{197}Au collisions.

E895 is a fixed target experiment that consists of a TPC [Rai 1990], a MUltiple Sampling Ionization Chamber (MUSIC) [Bauer 1997]. E895 studied elliptic flow of protons [Pinkenburg 1999] at bombarding momenta of 2, 4, 6, and 8 AGeV which lead to corresponding center of mass energies of $\sqrt{S_{NN}} = 2.68$ GeV, $\sqrt{S_{NN}} = 3.31$ GeV, $\sqrt{S_{NN}} = 3.83$ GeV, and $\sqrt{S_{NN}} = 4.29$ GeV.

E917/E866 is a fixed target experiment that mainly consists of Cherenkov counters, a TOF wall, Lead-glass arrays, a target multiplicity array, scintillators, calorimeters, and a spectrometer [Abbott 1990]. The spectrometer consists of four tracking chambers and the "Henry Higgins" magnet. E917 studied directed flow at bombarding momenta of 10.8 AGeV/c, which leads to corresponding center of mass energies of $\sqrt{S_{NN}} = 4.86$ GeV [Back 1999].

E877 is a fixed target experiment that consists of a high-resolution magnetic spectrometer, two calorimeters, two drift chambers, four Multi-Wire Proportional Chambers (MWPC), a TOF hodoscope, and a forward scintillator array [Barrette 1999]. E877 studied directed flow of light nuclei [Barrette 1999], anti-protons [Barrette 2000], protons and pions [Voloshin 1998] at a bombarding momentum of 10.8 AGeV/c, which leads to corresponding center of mass energies of $\sqrt{S_{NN}} = 4.86$ GeV. E877 also studied elliptic flow of protons and pions [Filimonov 1999] at a bombarding momentum of 10.8 AGeV/c, which leads to corresponding center of mass energies of $\sqrt{S_{NN}} = 4.86$ GeV.

1.5.3 RHIC Experiments

RHIC is an accelerator facility at BNL [Roser 2002] with two coupled synchrotrons. Both synchrotrons are able to accelerate Au ions up to 100 AGeV, leading to ^{197}Au +^{197}Au collisions of counter-rotating beams with center of mass energies of

$\sqrt{S_{NN}} = 200$ GeV. RHIC can also produce proton-proton and deuteron-nucleus collisions at the same nucleon-nucleon center of mass energies; thus, allowing a direct comparison of heavy ion collisions with nucleon-nucleon and nucleus-nucleus collisions with the same detectors (and detectors biases). All four RHIC experiments (Solenoidal Tracker At RHIC (STAR) [STAR 1992], PHENIX [PHENIX 1992], PHOBOS [PHOBOS 1991], and BRAHMS [BRAHMS 1994]) studied the collective effects of the collisions.

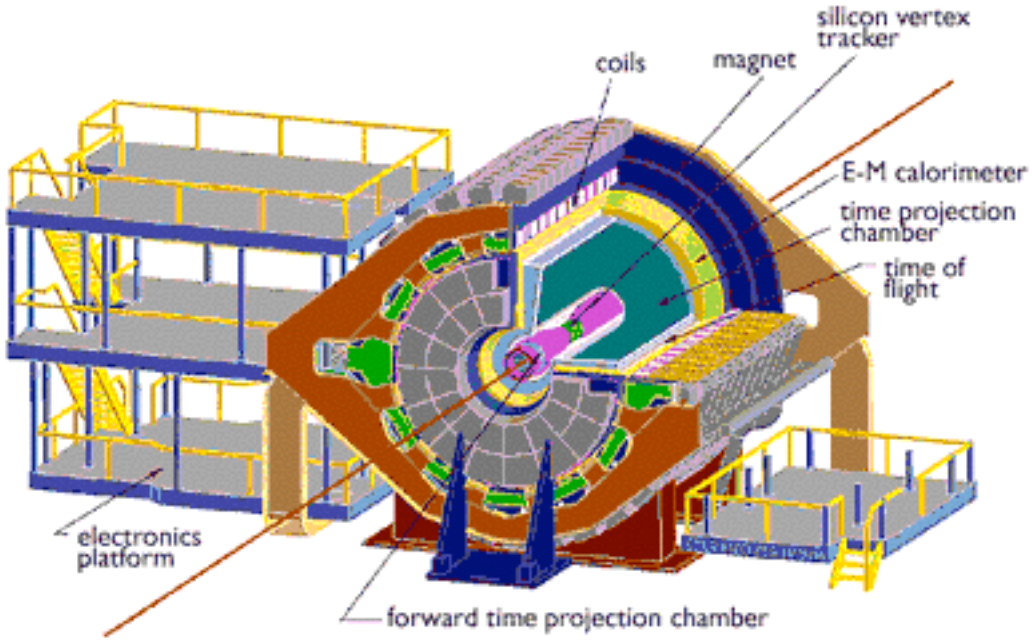

Figure 1.6: The STAR detector with its subsystems [STAR 2006].

STAR is an experiment that will be discussed at length in Chapter Two. STAR has studied directed and elliptic flow at $\sqrt{S_{NN}} = 200$ GeV, $\sqrt{S_{NN}} = 130$ GeV, $\sqrt{S_{NN}} = 62.4$ GeV [Ackermann 2001], [Adams 2004], [Wang 2005], [Tang 2005], and $\sqrt{S_{NN}} = 19.6$ GeV [present work]. Figure 1.6, above, shows a diagram of the STAR detector with its subsystems.

PHENIX is an experiment that mainly consists of four spectrometer arms: two central and two forward [Adcox 2003]. The central spectrometer arms consist of silicon vertex detectors, RICH detectors, TOF detectors, Time Expansion Chambers (TEC), pad chambers, drift chambers, and EMCs. The two forward arms consist of muon trackers and muon identifiers interleaved with steel. PHENIX is designed to favor detection of leptons and photons at high event rates. PHENIX has studied elliptic flow at $\sqrt{S_{NN}}$ = 62.4 GeV [Adler 2005], $\sqrt{S_{NN}}$ = 130 GeV [Adcox 2002] and $\sqrt{S_{NN}}$ = 200 GeV [Adler 2003]. Figure 1.7 shows the PHENIX detector with its subsystems.

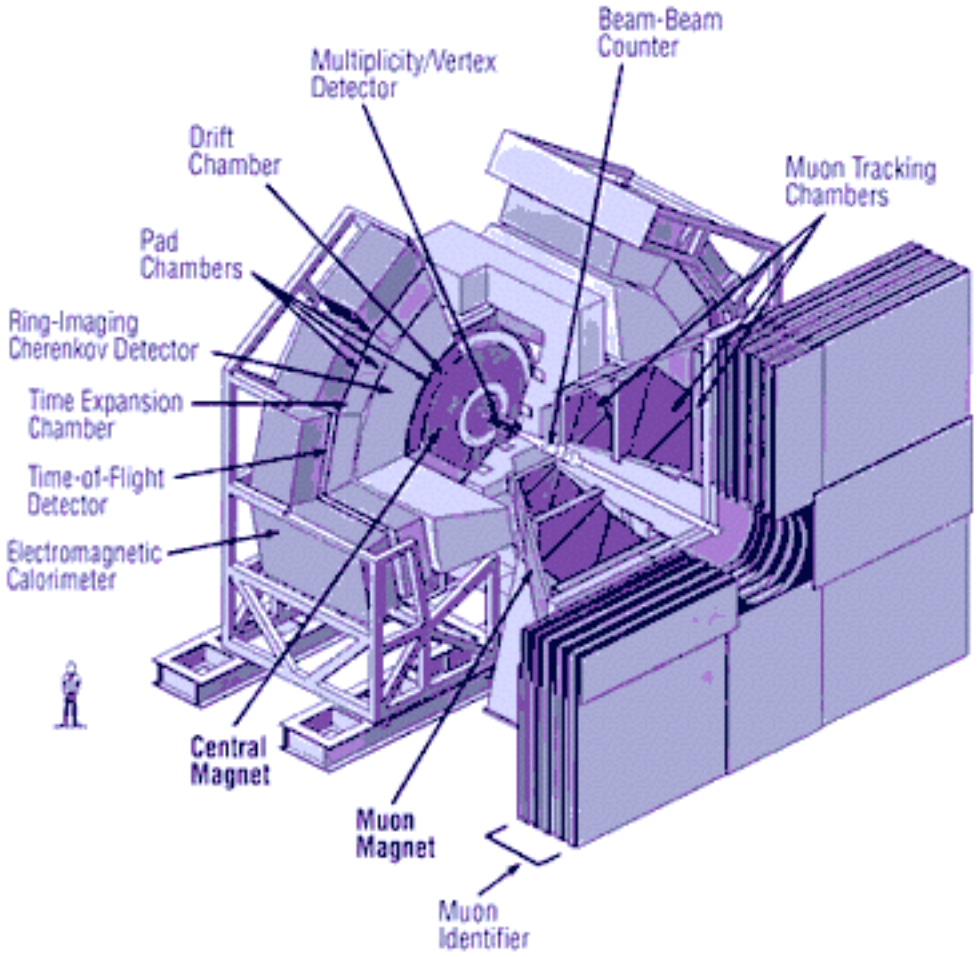

Figure 1.7: The PHENIX detector with its subsystems [BNL 2006].

PHOBOS is an experiment that mainly consists of a multiplicity detector and a two-arm spectrometer at mid-rapidity [Nouicer 2001]. The multiplicity detector covers an enormous pseudorapidity region. Pseudorapidity (η) is a geometrical measure of the coverage of a detector; it is given by: $\eta = -\ln\left(\tan\frac{\theta}{2}\right)$, where θ is the polar angle relative to the beam axis. PHOBOS has studied elliptic flow at $\sqrt{S_{NN}} = 19.6$ GeV, $\sqrt{S_{NN}} = 62.4$ GeV, $\sqrt{S_{NN}} = 130$ GeV, and $\sqrt{S_{NN}} = 200$ GeV [Manly 2003], [Back 2005]. PHOBOS has studied directed flow at $\sqrt{S_{NN}} = 19.6$ GeV, $\sqrt{S_{NN}} = 62.4$ GeV, $\sqrt{S_{NN}} = 130$ GeV, and $\sqrt{S_{NN}} = 200$ GeV [Mignerey 2005]. Figure 1.8, below, shows the PHOBOS detector with its subsystems.

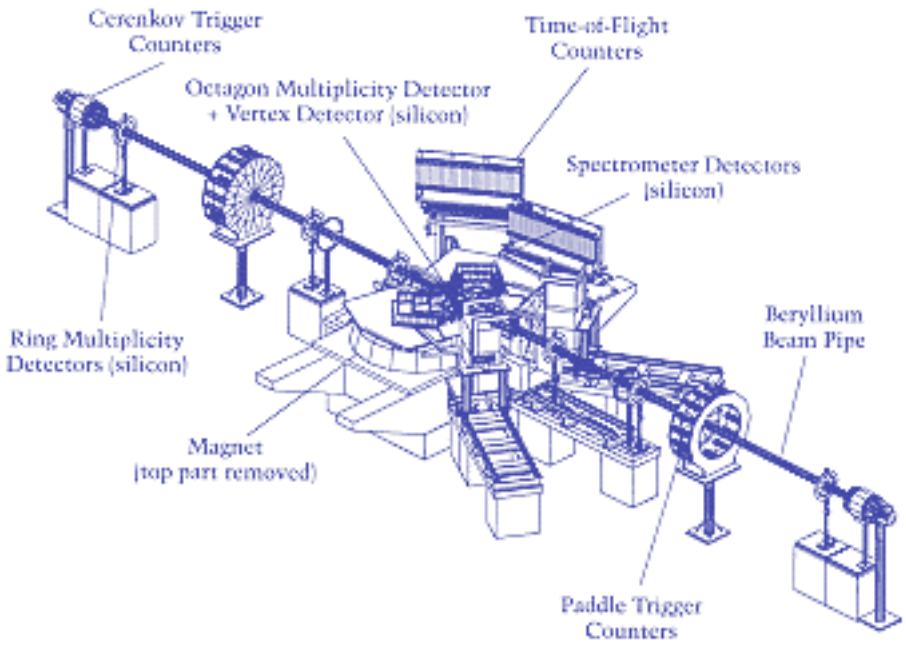

Figure 1.8: The PHOBOS detector with its subsystems [BNL 2006].

Broad Range Hadron Magnetic Spectrometers (BRAHMS) is an experiment that mainly consists of three different spectrometers: a mid-rapidity spectrometer, a front forward spectrometer, and a back forward spectrometer [Adamczyk 2003]. The mid-rapidity spectrometer consists of two TPCs, a TOF wall, and a Cherenkov counter. The

two forward spectrometers consist of three TPCs, drift chambers, a TOF hodoscope, a RICH, and a Cherenkov counter. BRAHMS is designed to measure and identify charged hadrons. Because of its small acceptance, BRAHMS is not able to study elliptic or directed flow. Figure 1.9, on the following page, shows the BRAHMS detector with its subsystems.

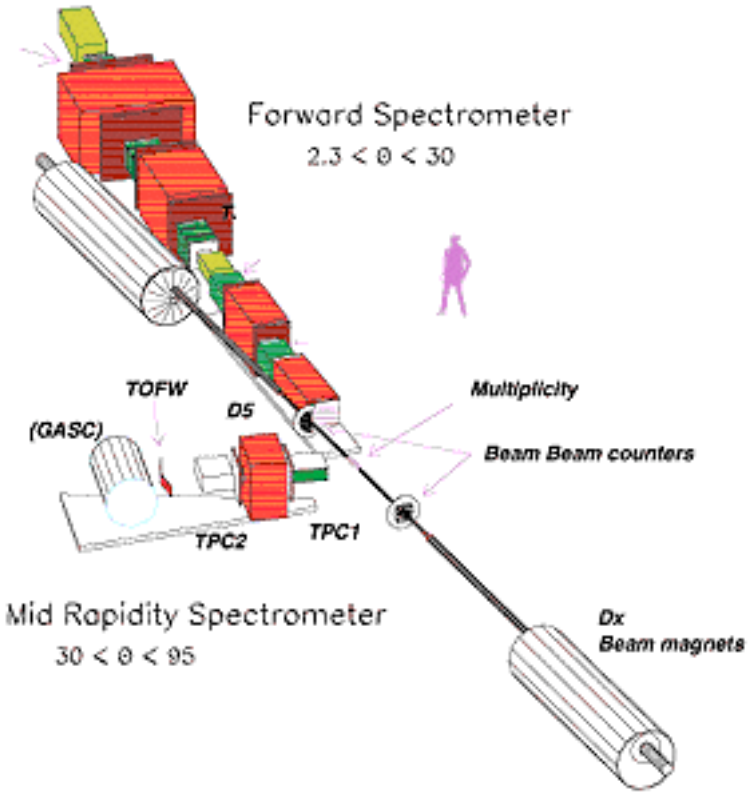

Figure 1.9: The BRAHMS detector with its subsystems [BNL 2006].

1.6 Specific Goals of This Thesis

This thesis examines directed and elliptic flow measurements at the STAR experiment for the 19.6 GeV data run. This data run is important since it is the one data point that STAR can compare with the nearby energies of the SPS experiments.

Chapter 2

Experimental Methods

Figure 2.1: An aerial view of Brookhaven National Lab [STAR 2006].

2.1 Relativistic Heavy-Ion Collider

The RHIC facility [Roser 2002] located at BNL in Long Island, New York (see Figure 2.1 on the previous page) allows particle and nuclear physicists the opportunity to study nuclear matter at energy densities that have never been observed before. It is designed to probe nuclear matter at high densities, pressures, and temperatures. RHIC is the first heavy ion facility to collide two beams of heavy ions rather than use a beam incident on a fixed target.

The RHIC facility creates $^{197}\mathrm{Au} + ^{197}\mathrm{Au}$ collisions at energies up to $\sqrt{S_{NN}} = 200$ GeV. This is more than an order of magnitude greater than the center of mass energy previously achieved. The center of momentum energy for colliders is [ ]. The fixed target center of momentum energy of $\sqrt{2}M_{beam}\sqrt{1+E_{beam}/M_{beam}}$ can be approximated at ultra-relativistic beam energies as [ ] (where M_{beam} is the mass of the beam nucleus and E_{beam} is the total energy of the nucleus). Prior to the construction of RHIC, the highest energy heavy ion collisions were provided by the SPS at CERN, which has a center of mass energy of 17.2 GeV per nucleon for $^{208}\mathrm{Pb} + ^{208}\mathrm{Pb}$ collisions.

The RHIC facility is a complicated system of electrostatic accelerators, bending magnets, and transfer lines. Figure 2.2 on the following page shows an overview of the facility. RHIC starts out by heating thin strips of gold foil to liberate gold atoms. An electron is added to each of the atoms to give them an overall negative charge. Then, the atoms are directed toward the Tandem Van de Graaf via an electric force. The Tandem Van de Graaf consists of a 15 MegaVolt (MV) electrostatic accelerator. It accelerates the negative gold ions toward a positive 15 MV potential terminal. The accelerated gold atoms are then stripped of numerous electrons resulting in positively charged gold ions. These gold ions are then repelled by the accelerator's positive potential resulting in another boost of energy. The gold ions leave the Tandem Van de Graaf accelerator with

a total energy of about 1 MeV per nucleon and a charge state of +32 (*i.e.* it has lost thirty-two electrons) [Nagle and Ullrich, 2002].

The Tandem to Booster (TtB) line transfers these gold ions from the Tandem Van de Graaf to the Booster synchrotron. The ions are traveling about 5% the speed of light when they leave the TtB. The Booster synchrotron pre-accelerates these particles before they enter the AGS. The gold ions attain an energy of 1 GeV per nucleon as they leave the Booster synchrotron and head to the AGS. The Booster synchrotron, along with the AGS and RHIC, uses a Radio Frequency (RF) cavity tuned to accelerate the ions with each pass around the ring. Carbon stripping foils between the Booster and the AGS fully strip the ions. Figure 2.3 on the next page shows a view of the accelerators leading up to RHIC.

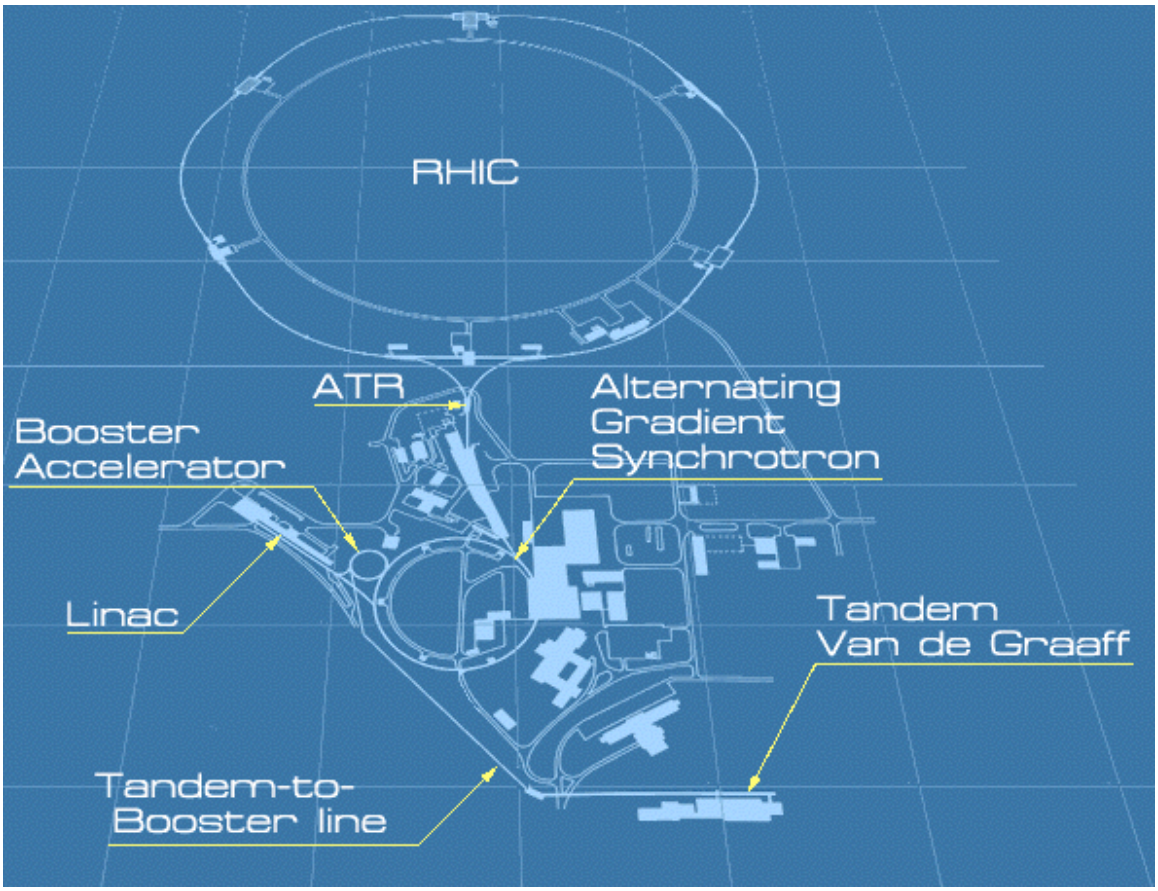

Figure 2.2: RHIC facility overview [BNL 2006].

The AGS takes these gold ions and accelerates them to an energy of 9.8 GeV per nucleon. Thus, the AGS takes in particles that are traveling 37% the speed of light and accelerates them up to 99.5% the speed of light. In order to keep the gold ion beam stable the AGS uses 240 magnets. The magnets are alternated inward, and outward creating magnetic field gradients which focus the gold ions both horizontally and

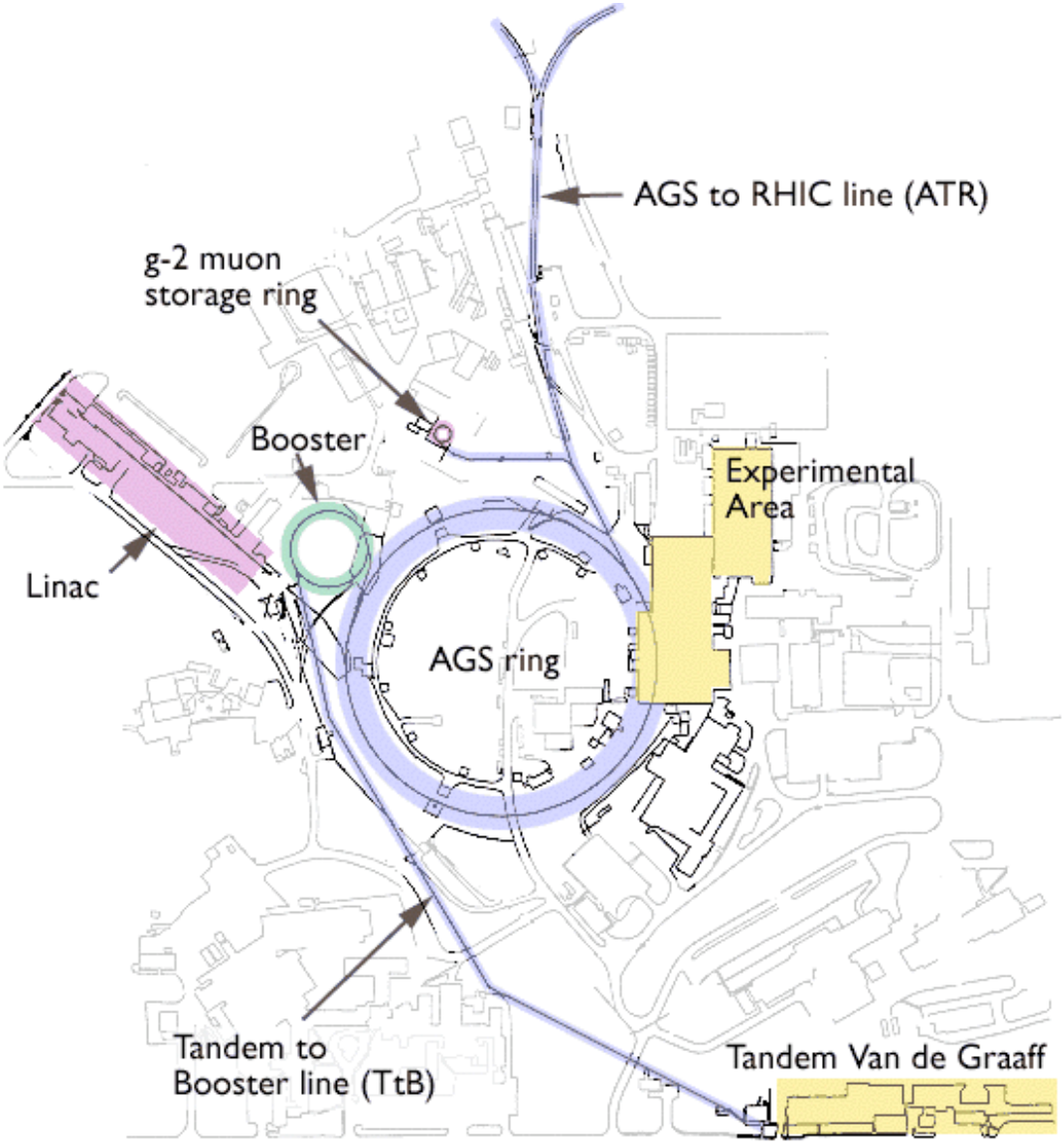

Figure 2.3: An up-close view of the accelerators leading to RHIC [BNL 2006].

vertically, hence the system of diverging and converging lenses is net focusing.

The AGS-to-RHIC transfer line (ATR) takes these gold ions to their final destination. The ATR has a switching magnet at its end that allows the gold ion beam to move in 'bunches' traveling either clockwise or counter-clockwise as it enters RHIC. Each of these 'bunches' contains billions of gold ions. When fully loaded each RHIC ring will contain 57 'bunches.'

RHIC has two interlaced rings in which the 'bunches' of gold ions move clockwise and counter-clockwise. These rings are called the blue ring and the yellow ring respectively. These rings have an average radius of 610 m and a circumference of 3833.8 m. They are made up of 1,740 superconducting magnets, which are cooled by a liquid helium bath to a temperature of about 4.5 Kelvin. It takes 15 MegaWatts of electrical power to chill the supply of liquid helium necessary to keep the rings cold. 1,600 miles of superconducting niobium titanium wire are wrapped around the magnets. The RHIC magnets can achieve a magnetic field of 3.45 Teslas at full energy.

RHIC accelerates the gold ions to a full energy of 100 GeV per nucleon. Consequently, the final speed of these particles is 99.995% the speed of light. Thousands of subatomic collisions take place every second. These collisions deliver 200 GeV of energy per nucleon when RHIC is at full energy. RHIC has also been run at $\sqrt{S_{NN}} = 130$ GeV, $\sqrt{S_{NN}} = 65$ GeV and $\sqrt{S_{NN}} = 19.6$ GeV. $\sqrt{S_{NN}} = 19.6$ GeV is the lowest kinetic energy that can be achieved at RHIC since the gold beams enter from the AGS at 9.8 GeV per nucleon. My work has focused on the 19.6 GeV run which occurred only over a 24-hour period on November 25th and 26th of 2001 on the final day of the heavy ion operation during RHIC Run II.

After the beams reach collision energy, they are then tuned to collide at four interaction regions. This is known as beam cogging. These regions are located at 2, 6, 8, and 10 o'clock when imagining RHIC as a clock from an aerial view. Figure 2.4 shows

the interaction regions. 2 o'clock holds the BRAHMS experiment. 4 o'clock holds the RF cavities. 6 o'clock holds the STAR experiment. 8 o'clock holds the PHENIX experiment. 10 o'clock holds the PHOBOS experiment. 12 o'clock held the pp2pp experiment. The data discussed in this paper were taken from the STAR experiment.

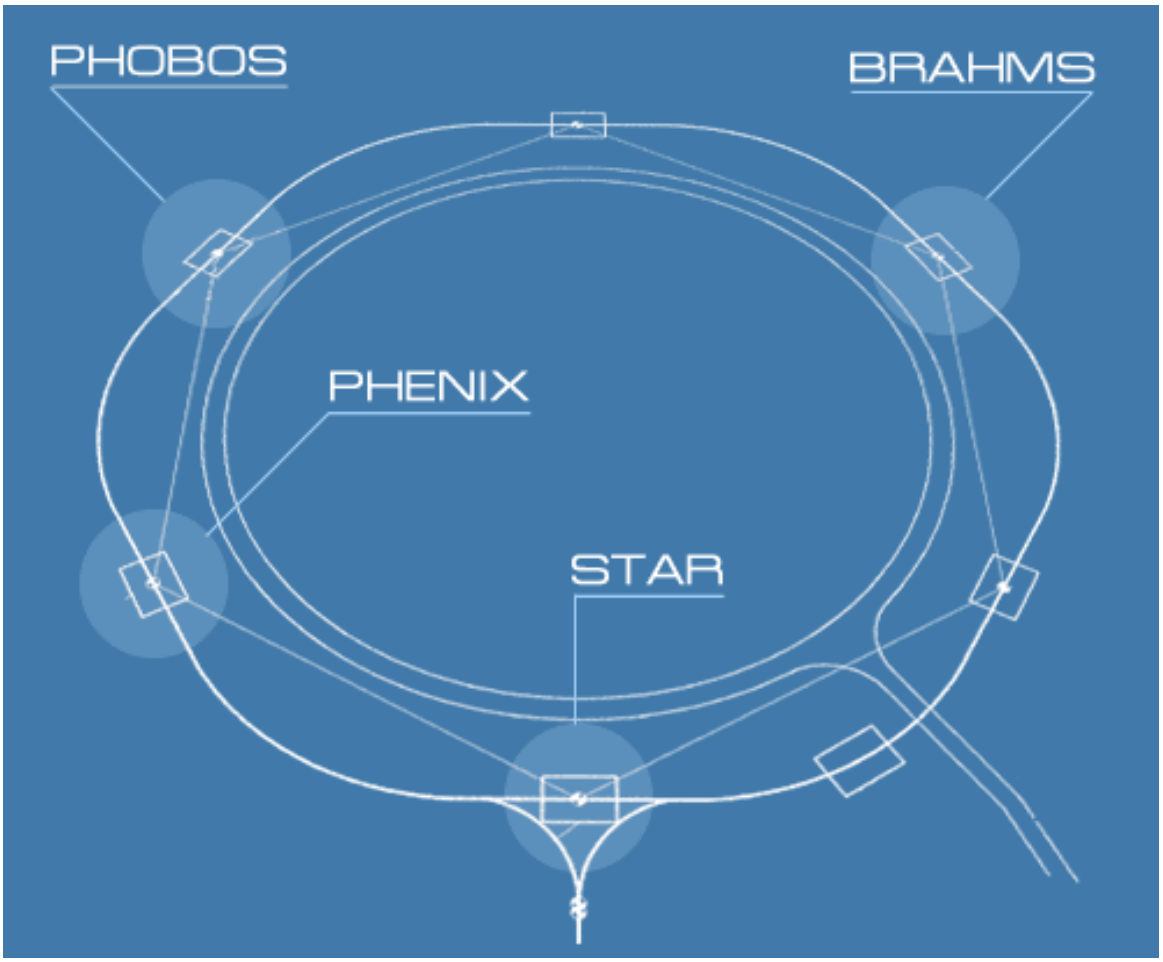

Figure 2.4: RHIC interaction regions [BNL 2006].

2.2 The STAR experiment

The STAR experiment is one of the major detector facilities at RHIC [STAR 1992]. During the 2001 data run (RHIC Run II) it was composed of a central TPC [Anderson 2003], two Forward Time Projection Chambers (FTPC) [FTPC 1998], a Silicon Vertex Tracker (SVT) [Bellwied 2003], a TOF patch [Bonner 2003], an EMC

[Beddo 2003], a RICH [Braem 2003], two ZDCs [Adler 2001], barrel scintillators, and a rather large Solenoidal Magnet [Bergsma 2003]. Figure 2.5 below shows the STAR detector systems. The following sections will describe the components of STAR relevant to this thesis.

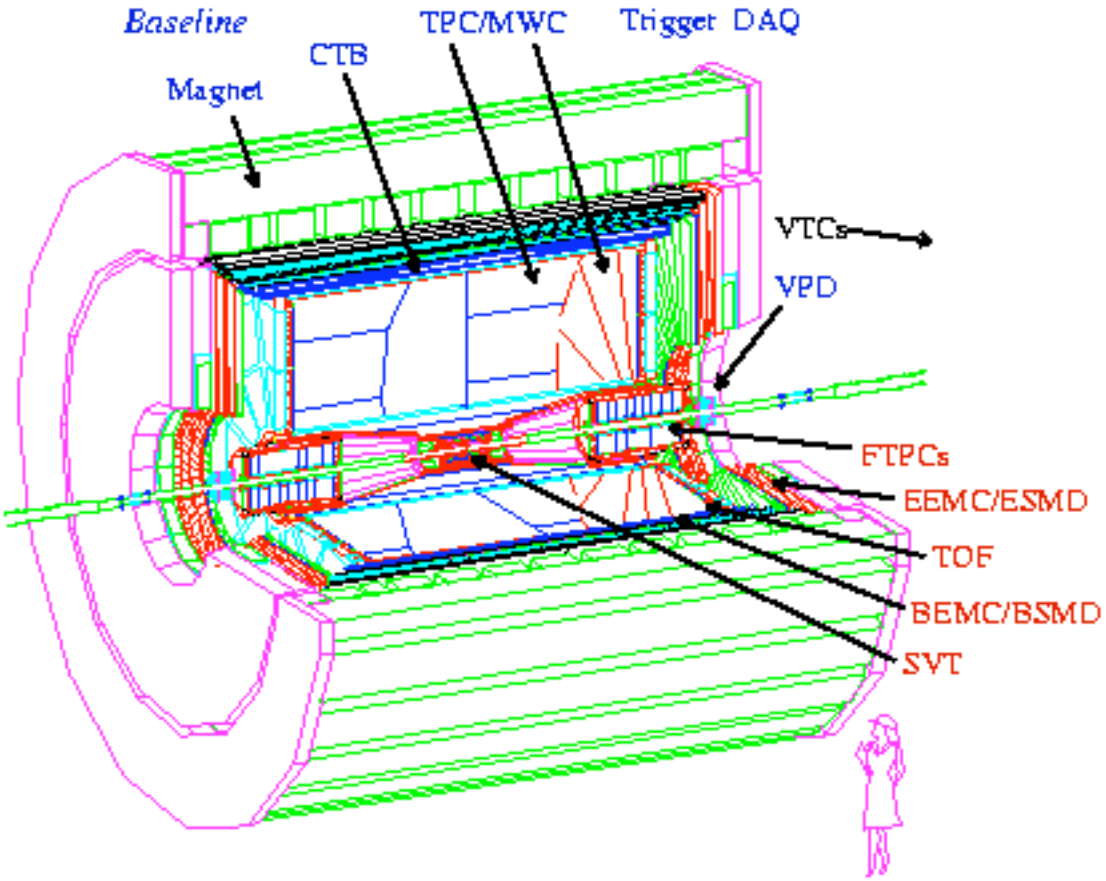

Figure 2.5: The STAR detector with its subsystems [STAR 2006].

2.2.1 A General Description of Time Projection Chambers

A TPC is an enclosed gas-filled chamber (it could also be filled with a liquid). Charged particles traverse the chamber, ionizing the gas. An applied axial electric field created by a high voltage plane causes the newly freed electrons to move axially toward a fine grid of pads and their electronic readouts. An applied magnetic field, mostly parallel

to the electric field, minimizes the transverse diffusion as the ionization cloud drifts along the electric field lines to the readout chamber. The charged particles leave a trail of these ionization electrons, which is referred to as a track. The three dimensional trajectory of this track can be reconstructed. Two coordinates are generated from the locations of the anode pads, and the third coordinate is projected using the drift time and drift velocity of the ionization cloud.

The transverse momenta of the particles can be determined from the radius of curvature of the track due to the magnetic field. Charged particles that move through a magnetic field follow a helical trajectory. Once you find the radius of this helix, then you can find the momentum of the charged particle via the equation: $p = qBr \sin\theta$ (where θ is the angle between the velocity of the charged particle and the magnetic field). The induced signals on the cathode pads can measure energy loss, dE/dx, and thus allow one to identify particle species via the Bethe-Bloch equation. The main electric field cage

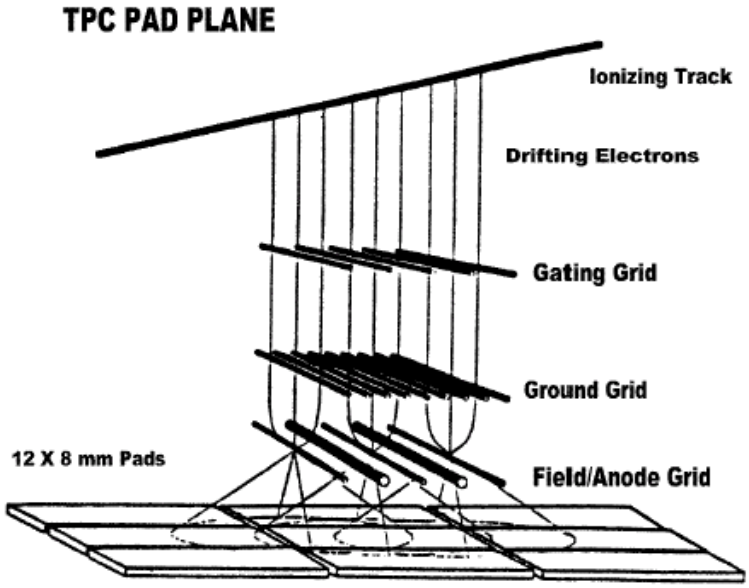

Figure 2.6: An ionizing track being recorded by the pad plane [Lohse and Witzeling n.d.].

needs to be structurally secure, yet also thin so that the material traversed by the particles is minimized in order to limit multiple scattering.

The readout region of a TPC consists of several wire planes and an MWPC which provides nearly noiseless signal amplification. Figure 2.6, on the previous page, shows an ionizing track traveling through the MWPC and being recorded by the pad plane. The first wire plane is the gating grid. This plane is designed to keep ionization by non-triggered events from reaching the MWPC. This helps to avoid the build up of space charge from slowly drifting positive ions. The gating grid can be set in two different modes. It can be "open" such that all of the wires are at the same ground voltage, therefore making them transparent to the drifting electrons. It can also be "closed" such that the wires are alternating positively and negatively biased, creating an electric field barrier that the electrons cannot pass. Figure 2.7 below demonstrates the gating grid in its "closed" and "open" modes.

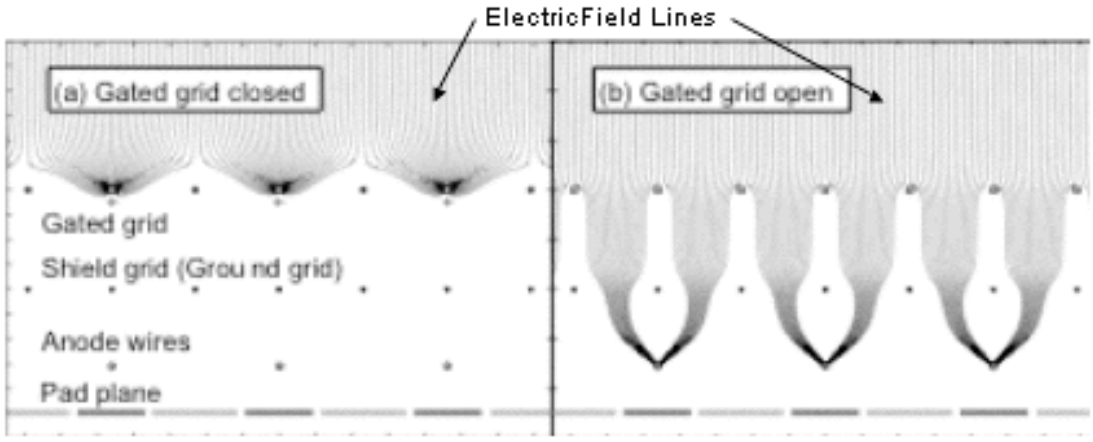

Figure 2.7: The gating grid in its "closed" and "open" modes [Lohse and Witzeling n.d.].

The next layer of the TPC readout is a plane of ground wires, which maintains the uniformity of the drift field, and separates the uniform drift field from the rapidly varying high fields of the MWPC. After the ground wires is a layer of anode wires. The anode

wires are sometimes alternate field/sense wires. The field wires are very thin and carry a high positive voltage. The sense wires decouple the field wires in order to reduce cross-talk between adjacent field wires (Note: STAR has no field wires). The drift electrons are in the high fields around the field anode gaining enough energy between collisions to cause an avalanche effect. These extra electrons induce an image charge on the cathode pads. The induced current pulse is then amplified, digitized, and interpreted by the electronics.

TPCs have various strengths. One strength is that a TPC can cover almost the full solid angle. Nearly all of the particles in the collision will go through the TPC. This is ideal for examining collision aspects such as total particle yield. Another strength of a TPC is that it has very good spatial resolution. It can determine the location of tracks to a precision of 200 μm orthogonal to the drift direction and better than 1 mm along the drift direction. This makes the TPC an excellent detector for tracking.

TPCs also have weaknesses. One weakness of the TPC is that it usually has a slow readout due to long drift lengths. The drift velocity in P-10 (90% Argon, 10% CH_4), a typical TPC gas, is 5.6 cm/μs at Standard Temperature and Pressure (STP). Typical TPCs are meters long, giving us a maximum drift time of around 20 μs. The maximum drift time for STAR is about 40 μs. This is quite slow when compared to detectors such as scintillators that have response times of about 0.01 μs.

2.2.2 A Brief History of TPCs

The first TPC was the PEP4 TPC [Nygren 1975] at the PEP storage ring at the Stanford Linear Accelerator Center (SLAC). David Nygren initially proposed the TPC in 1974. It was constructed in 1981 and began taking data in 1982. The PEP4 TPC was created to study particle production in electron-positron annihilations. The ability of the TPC to reconstruct nearly all of the particles in a dense event made it ideal for the experiment. The PEP4 TPC was the first to employ a gating grid to reduce space charge

[Hofman 1983]. Experiments that need to emphasize particle identification usually increase the pressure inside the TPC. The PEP4 TPC was pressurized to 8.5 atms, unfortunately this will reduce the momentum resolution ability of the TPC due to increased multiple scattering [Lohse and Witzeling n.d.].

Other experiments may want to enhance their momentum resolution. The ALEPH TPC [ALEPH 1989] (at the CERN LEP) was optimized for momentum resolution by operating at atmospheric pressure. The ALEPH TPC is one of the larger TPCs in existence measuring 3.6 meters in diameter and 4.4 meters in length [Atwood 1991].

Heavy ion fixed target experiments that have high track densities need to separate many tracks. NA35 was a heavy ion fixed target experiment at the CERN SPS that had large track densities [Eckhardt 1992]. The NA35 TPC was operated at atmospheric pressure in order to help with two-track separation.

The EOS TPC began taking data in early 1992 at the Lawrence Berkeley National Laboratory (LBNL) Bevalac [Rai 1990]. It was moved in 1995 to the BNL AGS. The innovative thing about the EOS TPC was that nearly all of the electronics were placed on the detector to reduce the number of cables going into and out of the detector. The Switched Capacitor Array (SCA), which consists of 128 capacitors, allowed for digitization and readout of the data at a reduced rate.

The NA49 experiment starting taking data in 1994 [Afanasiev 1999]. The NA49 experiment at the CERN SPS employs four large volume TPCs. Two vertex TPCs are located inside dipole magnets in order to find momentum for a particular track. Then two rather large main TPCs are located downstream in order to determine energy loss of a particular track. NA49 also went to a lighter aluminized Mylar field cage in order to help with minimizing multiple scattering [Wood 1998].

TPCs are for the most part used as the main part of the detector, but they may also be used to compliment other main systems. The BRAHMS experiment [Adamczyk

2003] at the BNL RHIC (which started taking data in mid 2000), for example, is mainly composed of two magnetic spectrometers but uses four smaller TPCs for extra information. The particle tracks are completely straight through the TPCs since they are located outside of the magnetic fields. The TPCs are located before and after the spectrometer magnets allowing for reconstruction of the particle momenta.

TPCs do not need to be filled with gas. The Imaging Cosmic And Rare Underground Signal (ICARUS) T600 TPC [Arneodo 2001], which is filled with liquid argon, was proposed in 1985 and began testing in 2001. This enormous underground detector located at the Grand Sasso Lab contains over 600 tons of liquid argon and is used to detect rare events such as proton decays and neutrino interactions.

2.2.3 The STAR TPC

The main detector in the STAR experiment is the central TPC. The STAR TPC is a large gas-filled cylinder with an inner radius of 0.5 meters and an outer radius of 2 meters. It has a length of 4.2 meters. The volume of the STAR TPC is 50 cubic meters. The gas circulation rate is 36,000 L/hr., which, given the volume, means that there is one volume change every 1.4 hrs. [STARnote 270]. The STAR TPC operates at atmospheric pressure. The STAR TPC is divided by a large central membrane into two equal halves with a length of 2.1 meters each: the west end and the east end. Each end has MWPCs to detect the drifting electrons. Figure 2.8 on the following page shows a conceptual drawing of the STAR TPC. The TPC sectors are numbered according to the STAR specification. The numbering is similar to that of a clock. The +z sectors are numbered 1-12 while the –z sectors are numbered 13-24 [STARnote 229]. Each end of the TPC will appear numbered clockwise from the perspective of a person looking into the TPC. A sector is divided into an outer part and an inner part.

The field cage, which surrounds the gas filled region, is composed of different material for the outer and inner portions. The outer field cage is made of copper for

strength. The inner field cage is made of aluminum (a lower Z material than copper) in order to minimize the multiple scattering induced as the particle traverses the material. Located at the top of the field cage is a resistor chain composed of 2 MΩ resistors which connect the 28 kV central membrane to the end caps (which are at ground) [Wieman 1997]. These resistors are used to create the electric field inside the TPC.

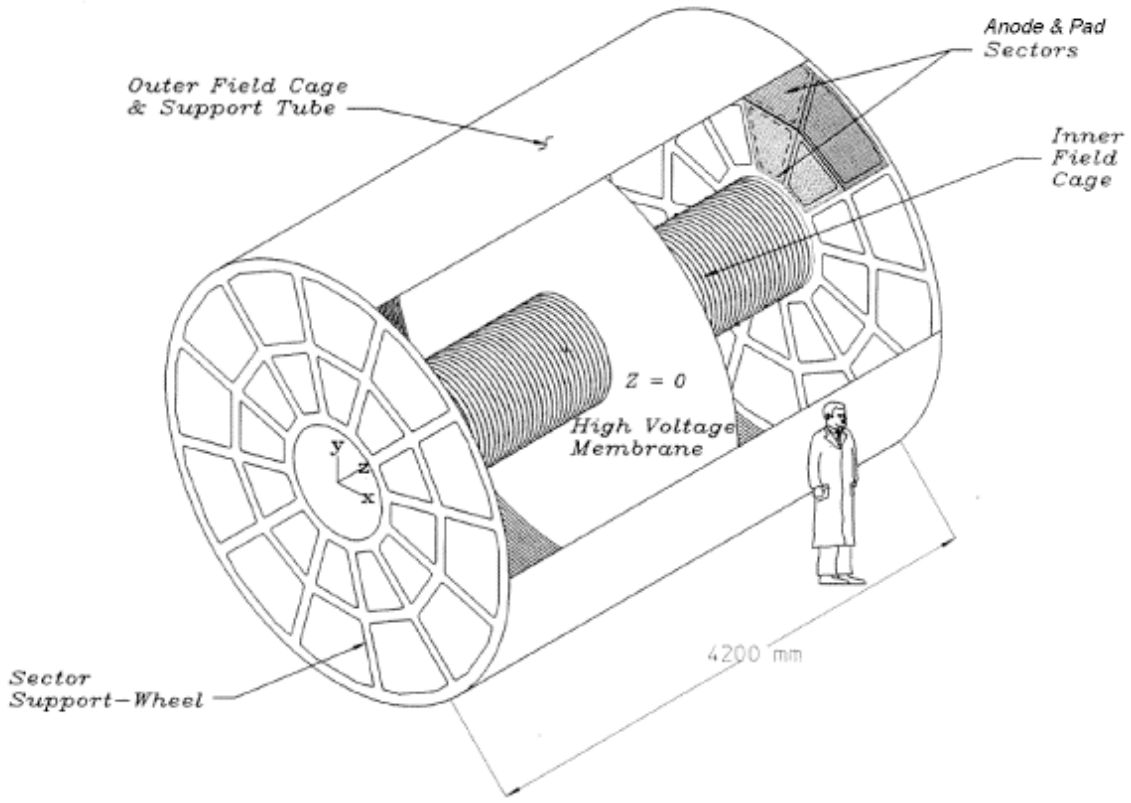

Figure 2.8: Conceptual picture of the STAR TPC [Anderson 2003].

The gas used in the STAR experiment was P-10. Recalling that the drift velocity of P-10 is 5.6 cm/μs at STP and with an electric field of 130 V/cm, and knowing that the maximum drift length is 2.1 m, this means that the maximum drift time for an electron is 37.5 μs. The anode plane is composed of 20 μm diameter gold plated tungsten wires with a 4 μm pitch and is strung with 0.5 Newton tension. The two edge wires on the anode plane are larger, 125 mm, (lower maximum electric field) gold plated Beryllium-

Copper to prevent excessive gain on the last wires. The inner sector anode wires are set to 1170 Volts and the outer sector anode wires are set to 1390 Volts. The next layer, the ground plane, is composed of 75 μm diameter wires [Wieman 1997]. The STAR TPC has no field wires separating the anode wires.

The pseudorapidity for charged particles in the STAR TPC is [ ]. The STAR TPC covers nearly the entire region surrounding the collision. Particle IDentification (PID) is obtained via multiple measurements of energy loss.

The STAR TPC is equipped with a temperature monitoring system that is composed of 120 thermistors placed on the cooling pipes of the West and East ends of the TPC. The thermistors are strategically placed on the electronics manifolds at the places most likely to encounter overheating. The temperature system takes readings every 60 seconds. These readings are plotted and directly put on the Internet so that they may be accessed at any time. The most recent measurements are available on the World Wide Web at http://tpctemp.star.bnl.gov. If the readings (which are typically between 68° and 78°) are out of specifications, they are written to a file so that they may be examined at a later time [STARnote 407].

2.2.4 The STAR LASER System

The Light Amplification by Stimulated Emission of Radiation (LASER) system in the STAR experiment is used to calibrate the TPC and FTPC [Abele 2003]. Distortions in the electric or magnetic field can cause electrons to divert as they approach the MWPCs. LASER systems can also be used to accurately measure the drift velocity of the gas. Focused LASER beams have a well-known position and will not have their positions altered by the surrounding magnetic and electric fields. This makes LASER beams ideal for detecting any drift anomalies. The STAR LASER system is composed of two (λ_{output} = 266 nm) Neodymium-Yttrium Aluminum Garnet (Nd-YAG) LASERs, one on the east end of the TPC and one on the west end of the TPC. The quantum energy

associated with the LASER $\left(E_{LASER} = \hbar c / \lambda_{output}\right)$ is enough to ionize the Argon in the P-10 through two-photon ionization. The STAR LASER fills nearly the entire TPC volume with approximately 450 LASER tracks.

2.2.5 The STAR Magnet

The STAR magnet is a solenoidal magnet with a poletip on either end. It is aligned so that the magnetic field will be parallel to the electric field created by the STAR TPC. The maximum field created by the magnet is 0.5 Teslas, which requires 4500 Amps through the ten main coils. The poletips, which weigh 73 tons each, have 1330 Amps running through them at maximum field. The poletip current helps maintain a uniform magnetic field. When the magnet is run at maximum field it has a power consumption of 3.5 MegaWatts [Bergsma 2003]. STAR has run the magnet with full-field and half-field. The full-field setting provides better high transverse momentum resolution. The half-field setting has a larger acceptance for low transverse momentum tracks. Both field settings have been run at standard and reversed polarity. Switching the magnetic polarity allows us to better understand detector biases.

2.2.6 STAR Electronics

After the image charges are read off of the pad plane, the signal immediately goes to the Front End Electronics (FEE) cards. The FEE cards are approximately 14 cm in length and 5 cm in width. Inside the FEE card the signals go to the STAR preAmplifier/Shaper (SAS), they are then sent to the Switched Capacitor Array/ Analog to Digital Converter (SCA/ADC), which temporarily stores and then digitizes 512 time samples. There are 4,300 FEE cards in 45 rows on the two end caps of the TPC. Each FEE card is connected to 32 cathode pads. This leads to about 136,000 channels and 70 million pixels for the TPC in a given event. Figure 2.9 on the following page shows a typical FEE card.

Up to 36 FEE cards can be controlled by a single FEE ReaDOut (RDO) board. The RDO board sends data from the FEE cards to the Data AcQuisition (DAQ) system via a fiber optic link. The RDO board also provides trigger and diagnostic functions. All electronics are mounted on the detector. This reduces time for processing and expense for cabling. Currently over 99% of individual channels are working and within specifications.

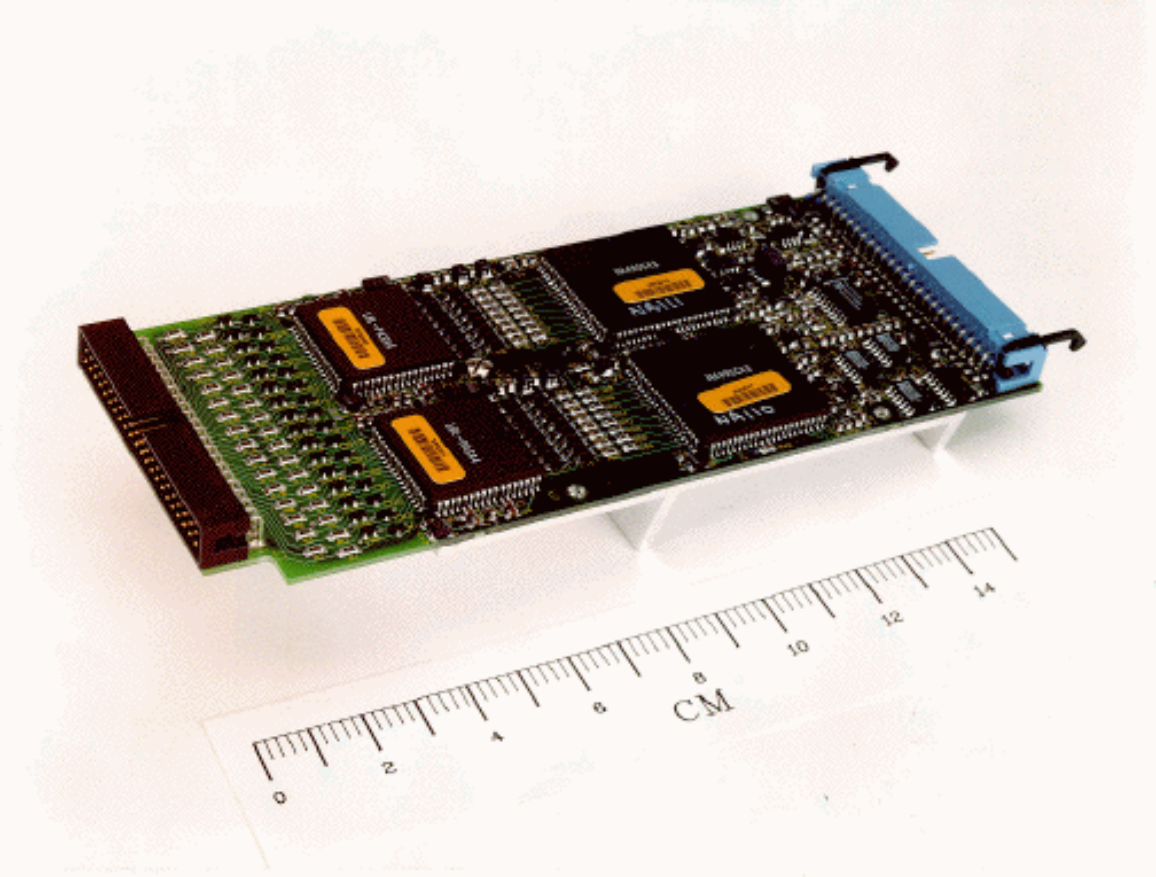

Figure 2.9: A FEE card [STAR 2006].

Chapter 3

Data Quality Assurance

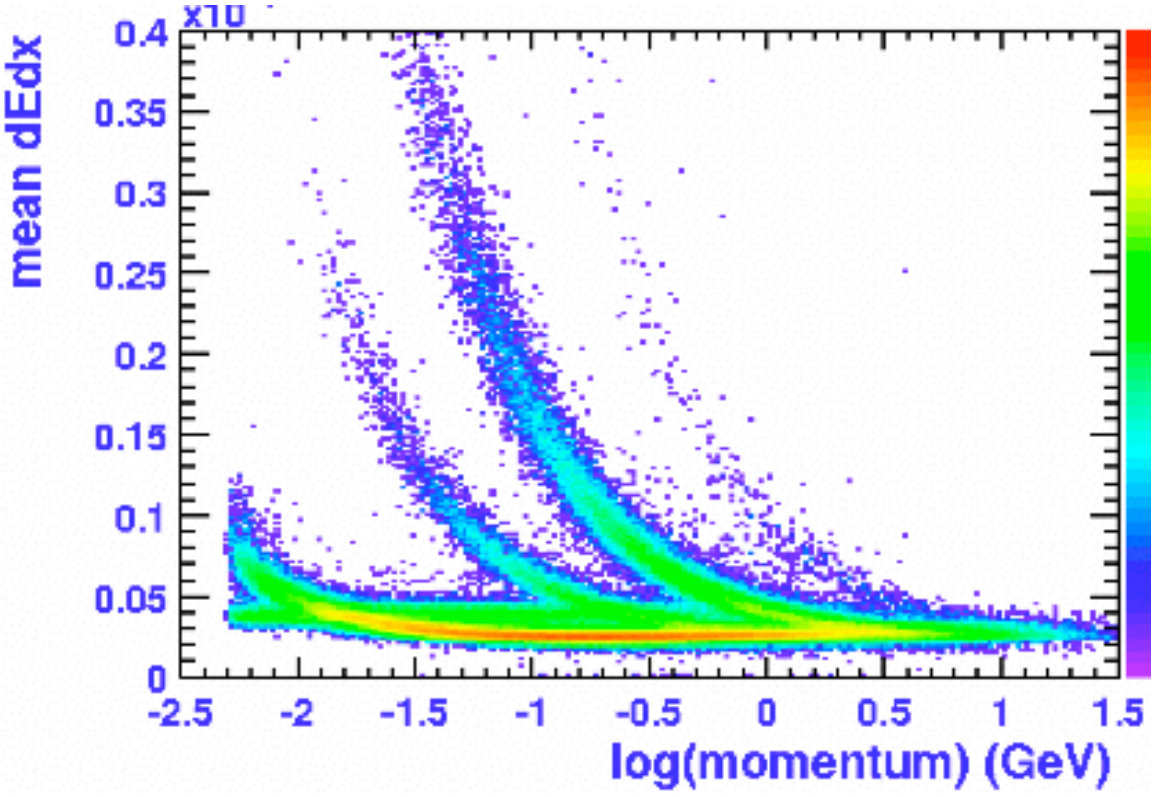

Figure 3.1: A Particle identification plot.

3.1 Event Quality Cuts

Not all collision events that were recorded during the 19.6 GeV data run were used in this analysis. Many collision events are eliminated due to undesirable traits. Also, in a given event, particle tracks coming from the vertex could be eliminated due to undesirable traits. Eliminating these undesirable traits is essential to making physical conclusions from plots and histograms that are based on these collision events. Figure 3.1 on the previous page shows a typical PID plot that will be analyzed. The following are requirements (cuts) we imposed to eliminate so-called "bad" events and tracks.

3.1.1 Vertex Z Cut

Au + Au collisions will occur randomly in a three–dimensional space in a diamond–shaped window centered in the middle of the TPC. Any collisions that occur outside of this diamond will most likely not be a Au + Au collision. The 20 GeV data set

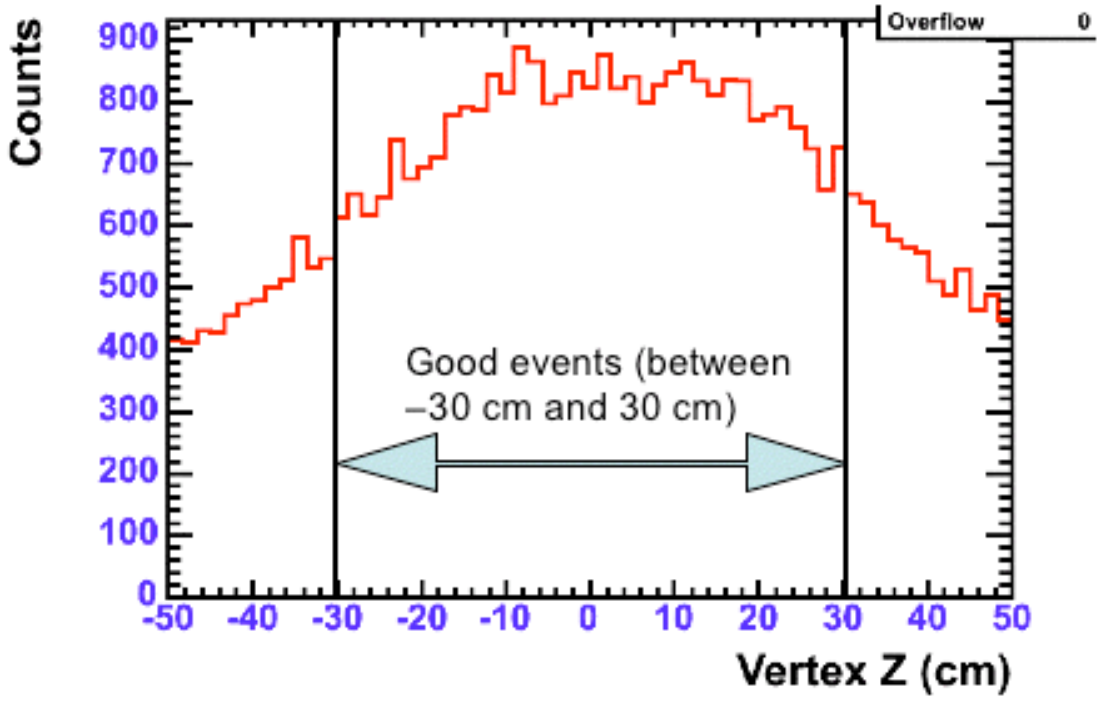

Figure 3.2: A histogram plot of vertex z.

was run with little warning and planning. The beams were not tuned properly. This left the event vertex distribution in the z dimension quite random compared to the other data runs.

One requirement imposed was the vertex z cut. For this event cut, every collision event must have had its vertex between –30 cm and 30 cm in the z-direction (the positive z direction is defined to be the projectile beam direction which is the clockwise RHIC blue ring). z = 0 is defined to be at the center of the STAR TPC, at the location of the central membrane (*i.e.* the center of the solenoid) [STARnote 229]. Figure 3.2 on the previous page shows a histogram of the track vertices of the collision events that survived the vertex z cut.

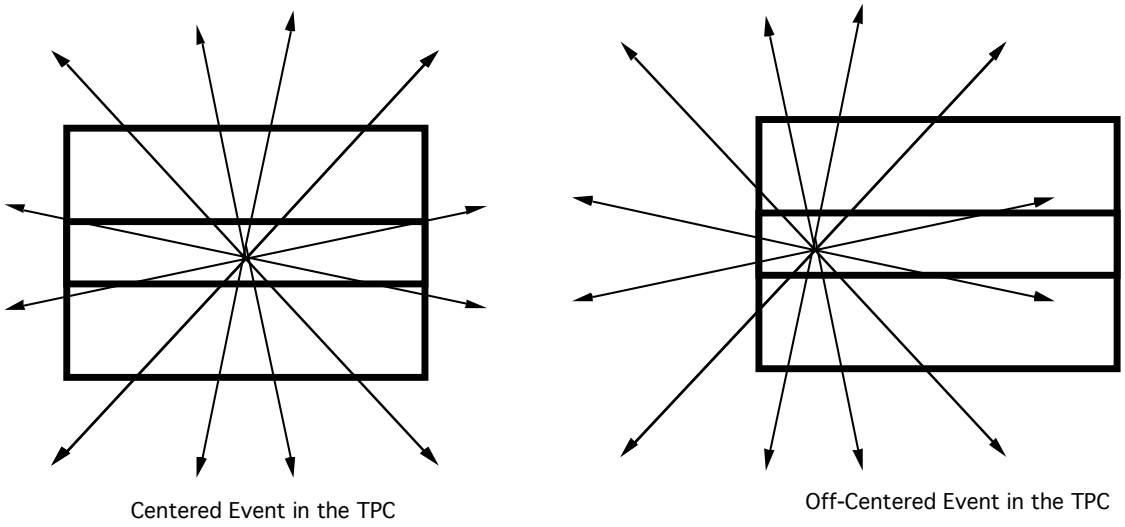

Figure 3.3: Centered and Off-Centered Events in the TPC.

The reason for the vertex z cut is that collision vertices that occur outside of this range may seriously impact acceptance corrections. Acceptance could drastically change on an event-by-event basis. Figure 3.3, above, shows a schematic of two identical collision events which occur at different locations inside the STAR TPC. When the collision event is centered in the detector, the TPC observes nearly all of the particles leaving the vertex with cylindrical symmetry. When the collision event is offset severely

to one side of the detector, the STAR TPC may not observe a fair number of particles that were emitted in one specific direction. It would complicate matters to have the acceptance corrections take this into account for every event.

3.1.2 Vertex XY Cut

There will also be a collision distribution in the x and y directions. Another requirement imposed was the vertex xy cut. For this event cut, every collision event must have had their vertex between –1.246 cm and 0.754 cm in the x-direction and –0.622 cm and 1.378 cm in the y-direction. In the STAR geometry framework, the positive x-direction is defined to point toward geographic South and the positive y-direction is defined to point upwards (radially outward from the center of the Earth) [STARnote 229]. Figure 3.4 below shows a plot of collision y vertex positions vs. x vertex positions.

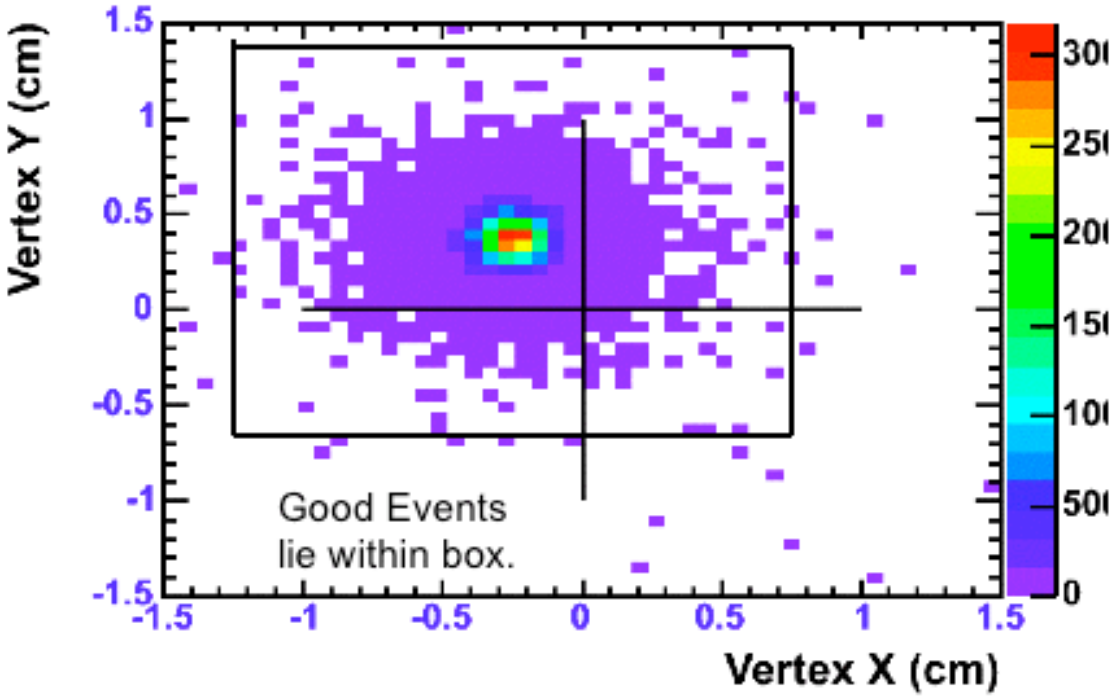

Figure 3.4: A plot of vertex y vs. vertex x.

The reason for this vertex xy cut is that nearly all $^{197}Au + ^{197}Au$ collisions occurred in that area. Collisions that occurred outside of this range are mostly events where one of the ^{197}Au beams struck a random gas molecule (a so-called beam-gas event) creating the illusion of a $^{197}Au + ^{197}Au$ collision.

3.1.3 Eta Symmetry Cut

Another requirement imposed was the eta (pseudorapidity) symmetry cut. For this event cut, every collision event must have had an eta symmetry between –1.25 and 1.25. Eta symmetry is a way to measure how many particles are traveling in a certain z-direction as opposed to the other. Eta symmetry is given by the following equation

$$EtaSym = \sqrt{\eta_+ + \eta_-}\left(\frac{\eta_+ - \eta_-}{\eta_+ + \eta_-}\right) + 0.003z$$

where η_+ is the number of detected particles that traveled in the positive z-direction, η_- is the number of detected particles that traveled in the negative z-direction, and z is the location of the vertex (in cm). The second term in the equation is a correction term for acceptance biases that may come about from collision events off-centered in the z-direction. Figure 3.5 on the following page shows a plot of eta symmetry versus z vertex positions.

The reason for the eta symmetry cut is to eliminate events which are obviously not symmetric in the laboratory frame, such as beam-gas events.

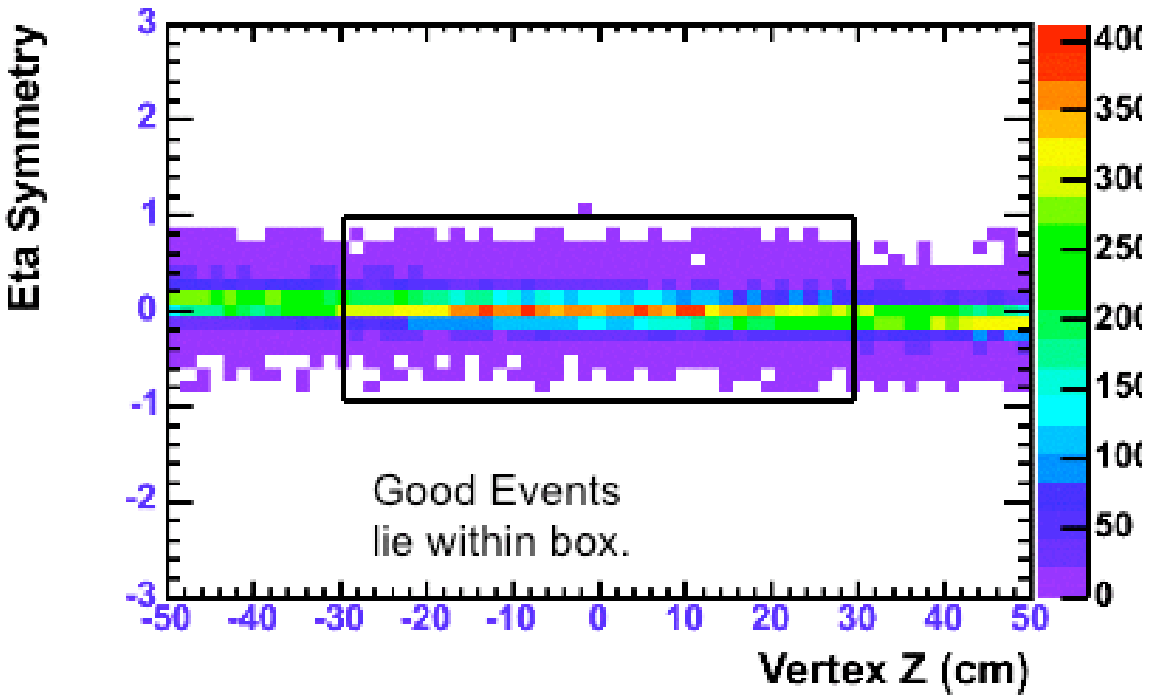

Figure 3.5: A plot of eta symmetry vs. vertex z.

3.1.4 Multiplicity Cut

Another requirement imposed was the multiplicity cut. For this event cut, every collision event must have had a multiplicity between 10 and 10,000. Multiplicity is the number of particles from the collision observed by the detector. Figure 3.6 on the following page shows a histogram plot of multiplicity.

At this beam energy level there will not be a nominal event with a multiplicity above 10,000. An initial guess of 10,000 for an upper limit was made prior to the analysis. Subsequent analysis revealed that this number was well above the observed maximum, but it was not changed to a lower number because it did not affect the analysis. Any collision event that has a multiplicity less than 10 was cut because it will be predisposed to giving a false particle flow signal.

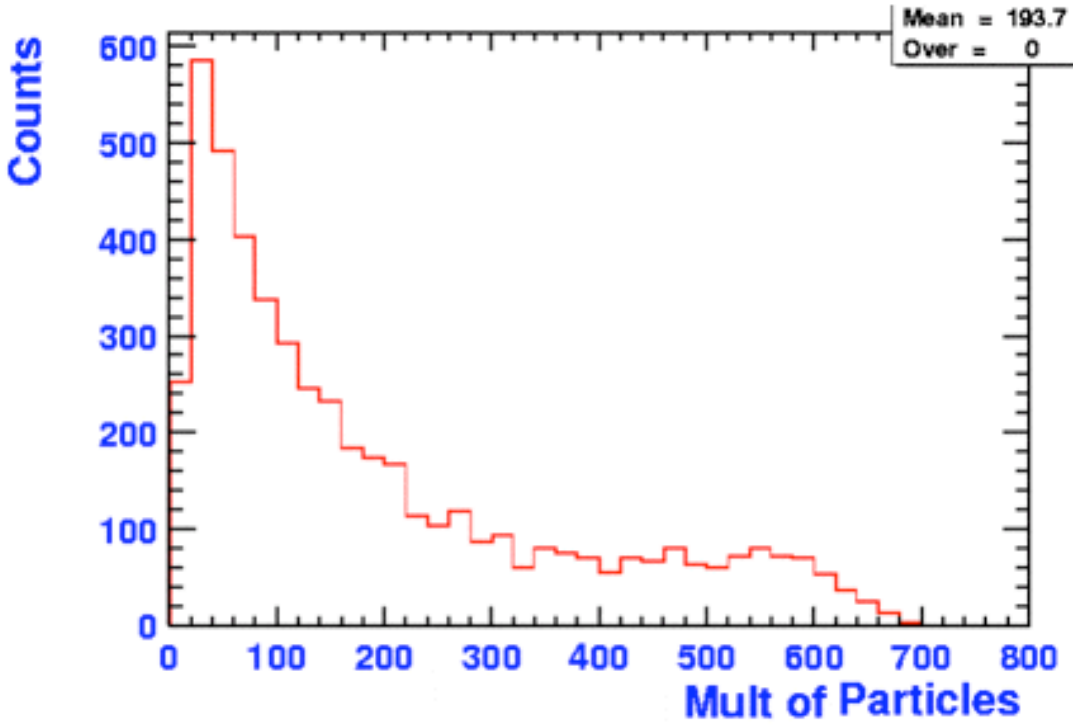

Figure 3.6: A histogram plot of multiplicity.

3.1.5 Overall Event Cuts

Of the nearly 170,000 triggered events in the 20 GeV data set, about 19% passed the event overall quality cuts. The multiplicity cut removed around 5% of the triggered events. The vertex XY cut removed about 0.75% of the triggered events. The vertex Z cut removed about 74% of the triggered events. The eta symmetry cut removed about 7% of the triggered events. This left around 31,250 events that passed all of the event quality cuts.

3.2 Track Quality Cut

Not all particle tracks that were recorded during a desirable collision event were used. Many particle tracks coming from the vertex were eliminated due to undesirable traits. Eliminating these undesirable traits is essential to making physical conclusions from plots and histograms that are based on these particle tracks.

3.2.1 Fit Points Cut

A requirement imposed was the fit points cut. STAR software reconstructs particle tracks by using various ionization hits made on the cathode pads. For this track cut, every particle track must have been fit with between 15 and 50 fit points.

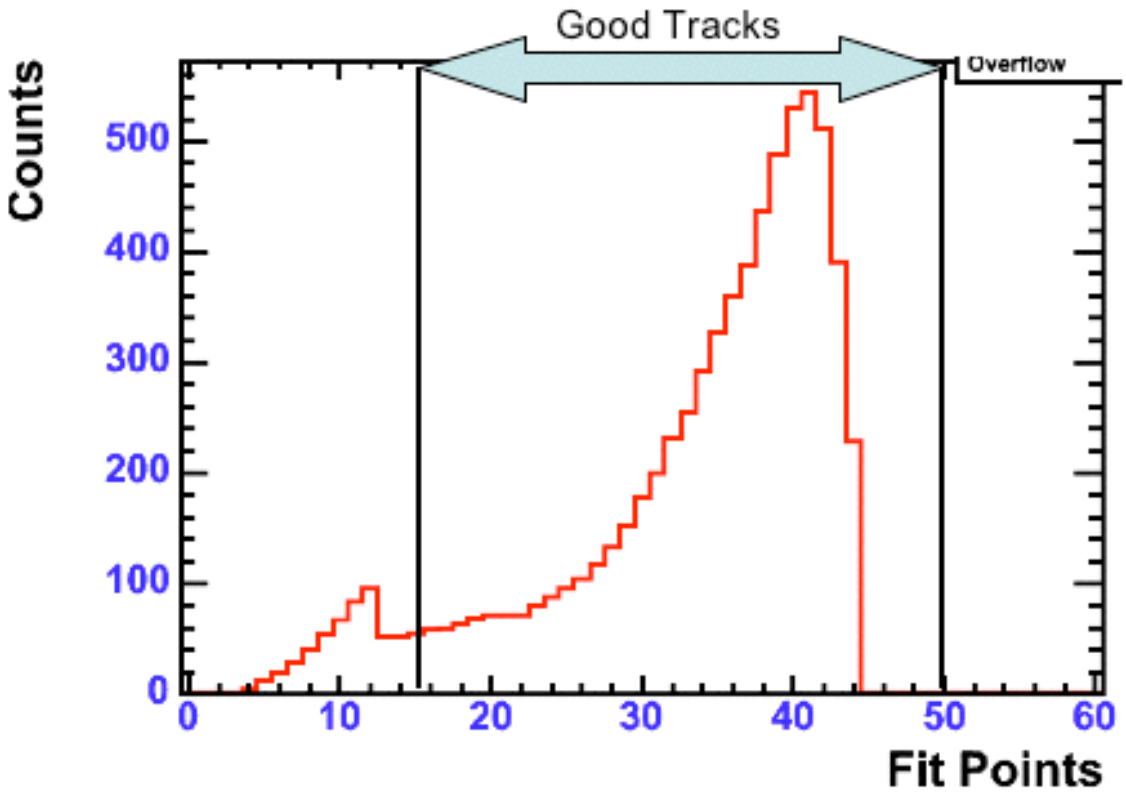

Figure 3.7: A histogram plot of fit points.

The maximum possible number of fit points for a straight track in the STAR TPC is 45 (46 if you count the primary event vertex). The upper boundary of 50 fit points is to eliminate an anomalous track. The lower boundary of 15 fit points was used to eliminate short tracks. Short tracks may be tracks that split from another longer one. This could lead to 'double' counting of tracks and could invalidate particle flow results. Figure 3.7 shows a histogram plot of the fit points of particle tracks that survived the fit points cut.

3.2.2 Fit Points Per Maximum Points Cut

Another requirement imposed was the fit points per maximum points cut. Particle tracks were determined by their number of actual hits divided by the geometrically possible number of hits for the helix. For this track cut, the fit points per maximum points ratio must be a number greater than 0.51 and less than 1.07. The upper boundary of 1.07 is meant to eliminate an anomalous track. Figure 3.8 shows a histogram of fit points per maximum points for particle tracks that survived the cut.

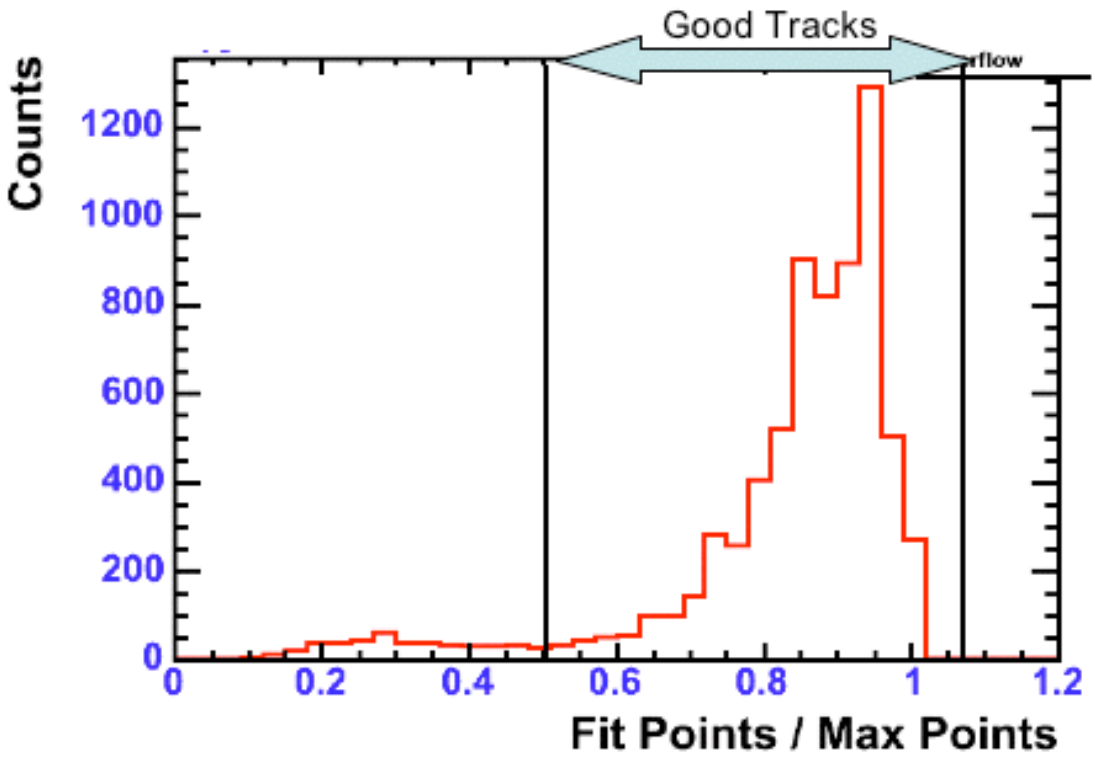

Figure 3.8: A histogram plot of fit points per max points.

The reason the ratio must be greater than 0.51 is to eliminate split tracks. A split track occurs when one track is identified as two separate tracks by the STAR reconstruction software. This could lead to 'double' counting of tracks and could disrupt particle flow results.

3.2.3 Chi Squared Cut

Another requirement imposed was the chi squared cut. For this track cut, chi squared per degree of freedom for any given track must be less than 2.5. Chi squared is a measure of how well the software reconstructed track matched the fit points from the cathode pads. Figure 3.9 below shows a histogram plot chi squared of per degree of freedom for particle tracks.

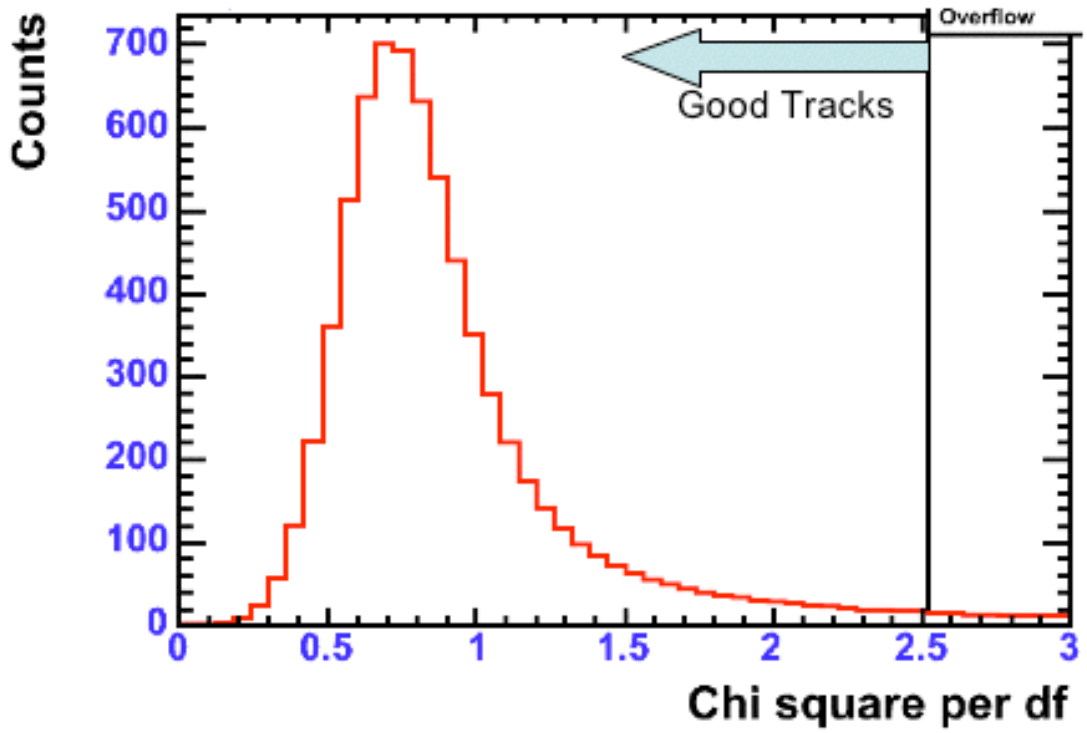

Figure 3.9: A histogram plot of chi squared per degree of freedom.

The reason for this cut is to eliminate poorly reconstructed tracks, which could corrupt the analysis.

3.2.4 DCA Cut

Another requirement imposed was the Distance of Closest Approach (DCA) cut. For this track cut, every used particle track must have passed within 3 cm of the primary vertex. Figure 3.10 shows a histogram plot DCA for particle tracks that survived the cut.

The reason for this cut is to minimize the admixture of tracks from secondary vertices.

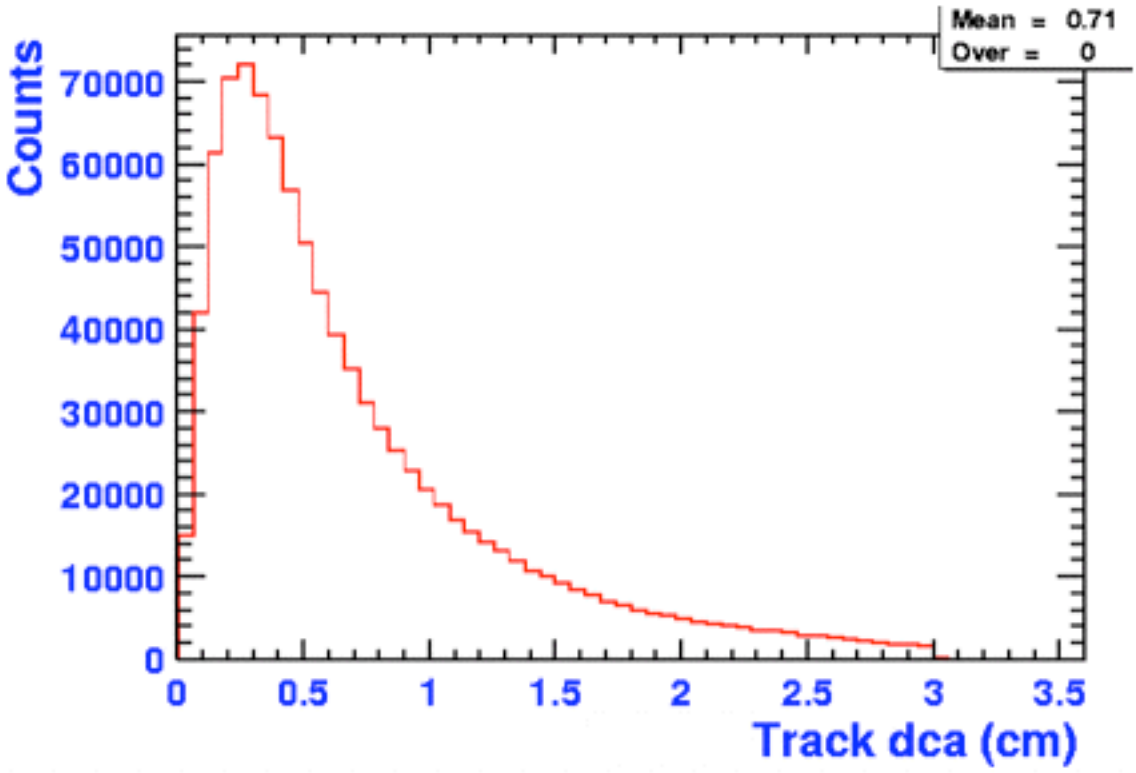

Figure 3.10: A histogram plot of DCA.

3.2.5 Overall Track Cuts

Of the "good" events in the 20 GeV data set, about 66% particle tracks passed the track quality cuts. The fit points cut removed around 18% of the particle tracks. The fit points per maximum points cut removed about 1% of the particle tracks. The chi squared cut removed about 9% of the particle tracks. The DCA cut removed about 3% of the

particles. Depending on what type of analysis that is being performed, particle tracks can also be cut based on their transverse momentum and pseudorapidity range.

3.3 Trigger Settings

The STAR trigger relies on many separate parts linked together with computer logic to ultimately make the decision to open the TPC gating grid and record the event. The following describes how the main parts work in conjunction with nominal triggers for a few different beam energies.

3.3.1 The Central Trigger Barrel

The Central Trigger Barrel (CTB) is an annular ring just outside of the STAR TPC. It consists of 240 scintillator slats, which cover the pseudorapidity range of –1 to 1. Photo-Multiplier Tubes (PMT) read out the light generated by the scintillators and output the signal to the detector electronics. Figure 3.11 on the following page shows a schematic drawing of the CTB.

The CTB can make a trigger decision in 1.5 microseconds. Since the drift velocity in the TPC is 5.6 cm/μs, this allows ample time to open the gating grid for the event. A central $^{197}Au + ^{197}Au$ collision at 200 GeV should yield 10 particles per slat.

3.3.2 The Zero Degree Calorimeters

Another main component of the STAR trigger are the ZDCs. The ZDCs are small transverse area hadron calorimeters that are located downstream of the DX dipole magnets, 18 meters downstream from the interaction point. The RHIC yellow ring (which moves counter-clockwise) will have spectator (free) neutrons from a dissociated ^{197}Au nucleus hit the East ZDC if there is a collision. The RHIC blue ring (which moves clockwise) will have the spectator (free) neutrons hit the West ZDC if there is a collision. Figure 3.12 shows a schematic drawing of a ZDC.

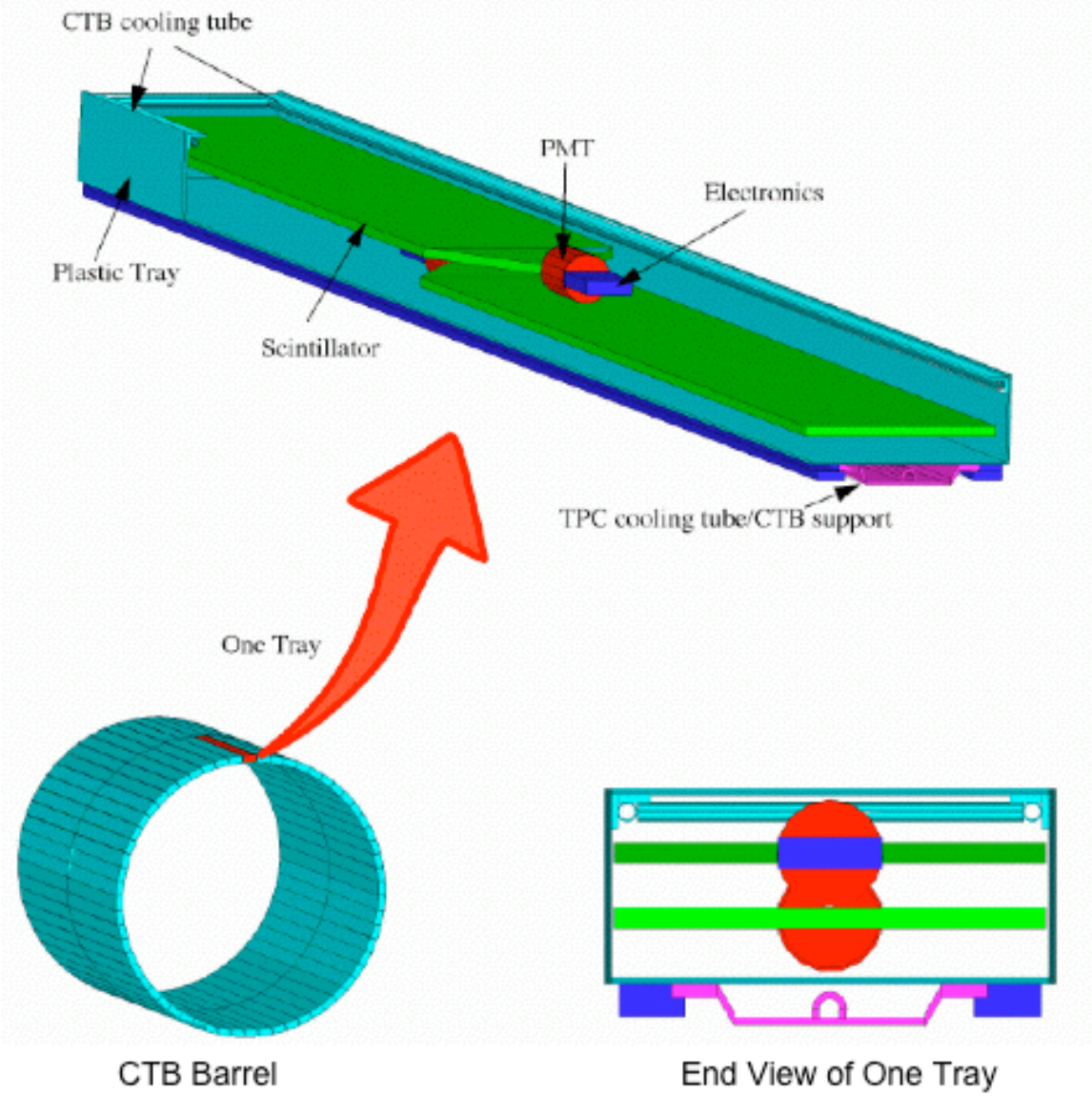

Figure 3.11: A schematic drawing of the CTB [STARTrig 2006].

A ZDC has three modules, which consist of alternating layers of Pb and scintillator fibers. The resulting signal is read out by PMTs. The ZDC detectors measure neutral energy with a 2 millirad cone about the beam direction by counting the number of spectator (free) neutrons. Charged particles are swept away by the dipole magnet (they no longer have the proper charge–to–mass ratio to continue their circular path after the

collision). A central collision at 200 GeV yields 25 neutrons in the ZDC [Bieser 2003]. ZDC timing resolution is about 0.1 nanoseconds.

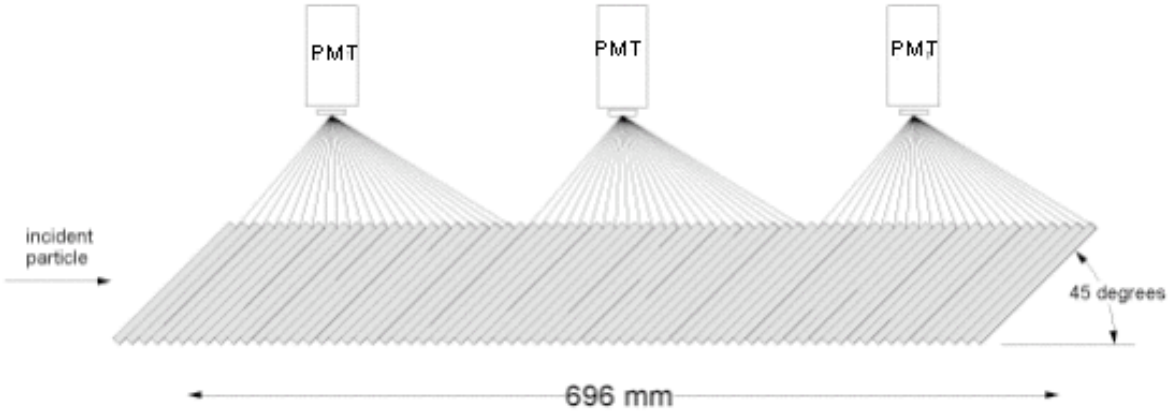

Figure 3.12: A schematic drawing of the ZDC [STARTrig 2006].

3.3.3 Nominal Triggers

A nominal minimum bias trigger for the 200 GeV $^{197}Au + ^{197}Au$ RHIC run II would have the following conditions: at least five ADC counts (about one neutron) detected by the East ZDC from the yellow ring, at least five ADC counts (about one neutron) detected by the West ZDC from the blue ring, at least 75 counts by the CTB (this roughly translates to 15 particles) and blue-yellow sync (when ion bunches in the blue and yellow rings are synchronized to cross simultaneously at the interaction regions) [Bieser 2003]. A nominal central trigger for the 200 GeV $^{197}Au + ^{197}Au$ RHIC run II would have the same conditions as the minimum bias plus a requirement of 2,000 particles detected by the CTB.

3.3.4 The 19.6 GeV Trigger

The 19.6 GeV data run was taken with a minimum bias trigger [Bieser 2003]. As mentioned earlier, the 19.6 GeV data run was taken on the final day of the RHIC run II heavy ion operation. This beam energy had not been planned prior to the end of RHIC

run II. This surprise beam energy run left little time available for trigger optimization to this specific energy. Thus, STAR was mostly left in the mode for taking 200 GeV data.

For a lower beam energy data run, the lower beam fragment longitudinal momentum yields a larger opening angle for spectator neutrons. In addition, the fragments are not completely dissociated and a fraction of the spectator neutrons are bound up in deuterons, tritons, helions, and alpha particles, which are all bent by the magnets and do not get measured by the ZDC. This resulted in ZDC trigger inefficiencies for extremely peripheral (impact parameter greater than 12 fm) events where the beam remnant breaks into complex fragments rather than into base neutrons and protons. The ZDC trigger was also increasingly inefficient for collisions with impact parameter around 7 fm. In these collisions the opening angle of the spectator neutrons was larger than the solid angle subtended by the ZDC.

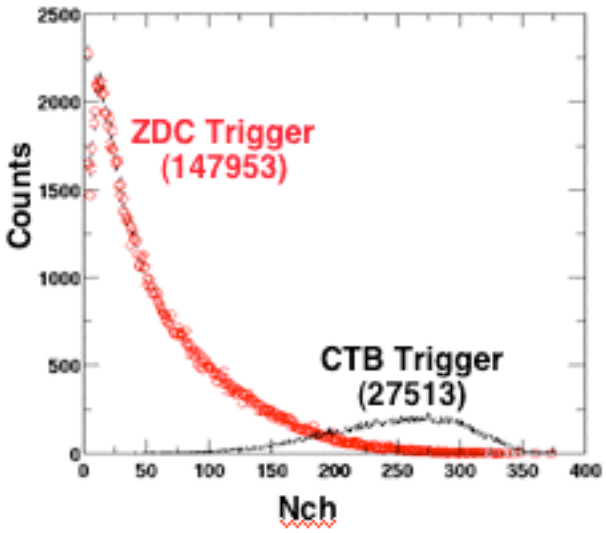

Figure 3.13: A histogram plot of the ZDC and CTB triggers for the 20 GeV run [Cebra 2002].

In order to approximate a minimum bias trigger for the 19.6 GeV run, events were selected if they satisfied either one of two trigger conditions. The first trigger condition

required a coincidence between ZDC east and west (both set a low threshold level corresponding to approximately one neutron) and the blue and yellow syncs. The second trigger condition required the Central Trigger Barrel (CTB) sum signal to pass a high threshold (corresponding to over one hundred charged particles within one unit of midrapidity) in coincidence with the blue and yellow syncs. The combination of these two hardware trigger conditions provided a data set that contained the full range of impact parameters (*i.e.* minimum bias). Figure 3.13 on the previous page shows a histogram plot of the ZDC and CTB triggers for the 20 GeV data run [Cebra 2002].

The shape of this data run was much different from the 200 GeV data run. Figure 3.14 below shows a scatter plot of counts for the ZDC and CTB.

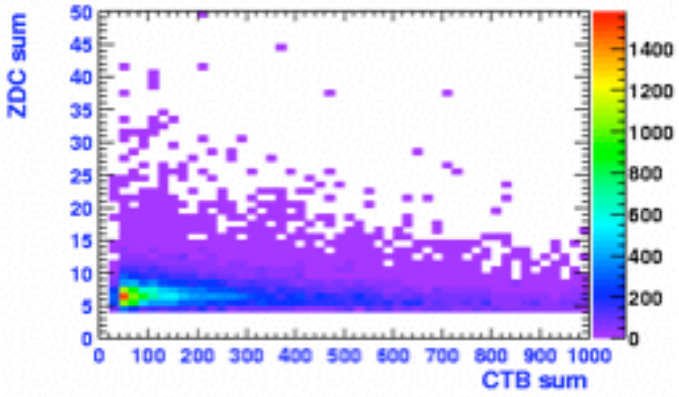

Figure 3.14: A scatter plot of counts for the ZDC and CTB.

Chapter 4

Analysis Techniques

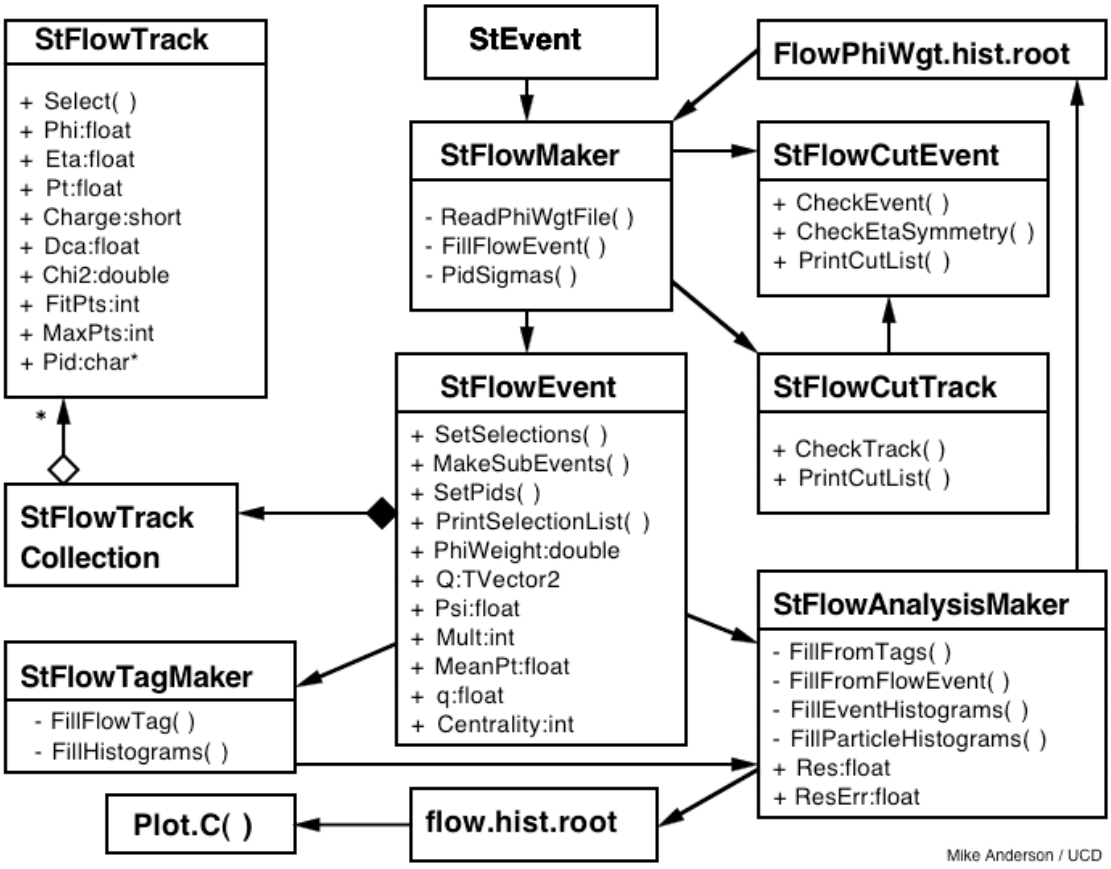

Figure 4.1: A flowchart of the complicated software routine.

4.1 Event Plane Determination

Once we have an event to analyze, we must then try to extract multiple moments flow values from this violent collision through a complicated software routine. Figure 4.1 shows a flowchart of the complicated software routine. When examining the distribution of particles from a given event, it becomes easier to turn to a Fourier series expansion to relate the azimuthal dependence [Ollitrault, 1993]

$$E\frac{d^3N}{d^3p} = \frac{1}{2p}\frac{d^2N}{p_T dp_T dy}\left(1 + \sum_{n=1}^{\infty} 2v_n \cos(n(\phi - \Psi_r))\right)$$

where ϕ is the angle of the azimuthal emission angle with respect to the reaction plane for a particular particle, Ψ_r is the true reaction plane (the x-z plane created by the impact parameter and the projectile's velocity vector for a given event), p_T is transverse momentum, and y is rapidity. Rapidity, y, is the relativistic generalization of velocity given by the following equation

$$y = \frac{1}{2}\ln\left(\frac{E + p_z}{E - p_z}\right)$$

Note that rapidity has no upper bound and that it is unitless.

The first two Fourier coefficients, v_1 (the first Fourier coefficient of anisotropy, directed flow) and v_2 (the second Fourier coefficient of anisotropy, elliptic flow), will tell us important information about the (probably early) stages of the violent event collision. There has been some recent interest in the higher Fourier coefficients [Kolb 2003], [Adams 2004] but they will not be examined in this paper.

The first task is to try to reconstruct the reaction plane from the information given to us by the detectors. The event plane angle, an estimate of the real reaction plane angle, is unique to each event. The event plane angle is estimated by constructing a special

vector known as the Q–vector [Danielewicz and Odyniec, 1985]. The Q-vector is given by

$$\vec{Q} = \sum_{i=1}^{N} \omega_i \vec{u}_i$$

where N is the number of detected particles in the event, $\vec{u}_i$ is the unit vector parallel to the transverse momentum of the i^{th} particle, and ω_i is the weight assigned to the i^{th} particle. The Q-vector was determined independently for directed and elliptic flow. In the directed flow analysis $\omega_i = -1$ for $y < 0$ and $\omega_i = +1$ for $y > 0$. In the elliptic flow analysis for $p_T < 2$ GeV/c, $\omega_i = p_T$; for $p_T > 2$ GeV/c, $\omega_i = 2$ GeV/c. With proper weighting, $\vec{Q}$ should point in the direction of the impact parameter, $\vec{b}$.

4.2 Event Plane Resolution

In the extreme case, with infinite multiplicities per event, $\vec{Q}$ lies in the direction of the true reaction plane defined by the beam direction, z, and the impact parameter, $\vec{b}$ [Ollitrault, 1993]. With our multiplicity of several thousand, the direction of $\vec{Q}$ will usually differ from that of $\vec{b}$, event by event. This reaction plane error must be taken into account when calculating flow values.

In order to understand this correction Figure 4.2 shows a schematic for determining the error due to a false reaction plane measurement.

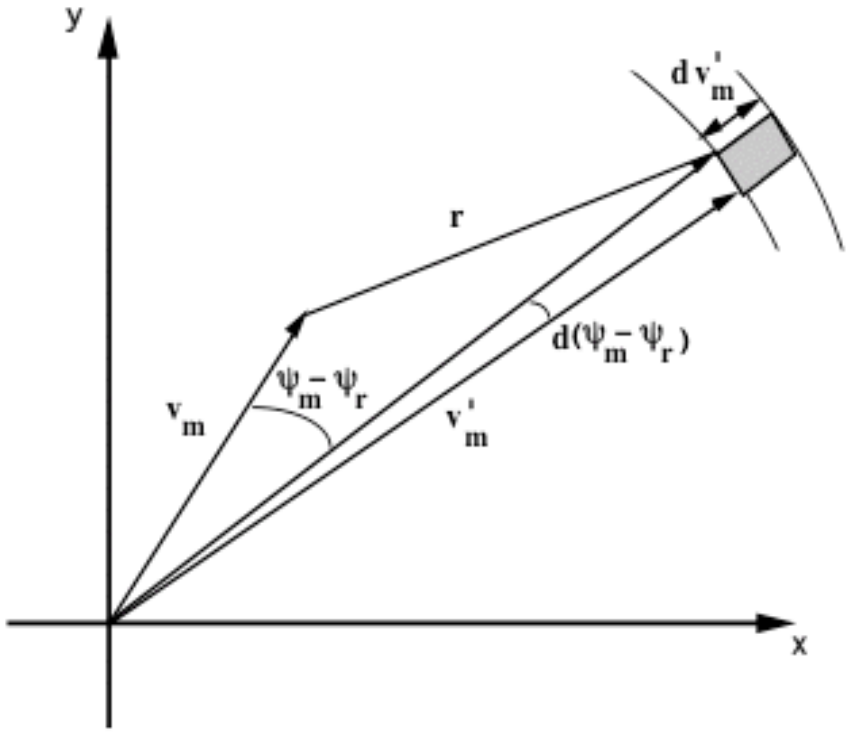

Figure 4.2: A schematic for determining the error due to a false (*i.e.* statistically limited) reaction plane measurement in an event.

In this schematic, $\vec{v}_m$ represents the flow value if you had no event plane resolution problems and averaged over billions of events. $\vec{v}'_m$ is the coefficient if you had measured the angle $(\psi_m-\psi_r)$ as the reaction plane. r is the error in $\vec{v}'_m$. σ is the uncertainty in the length r. σ is related to event multiplicity and is assumed to be independent of $\vec{v}'_m$. For example, if flow were zero, the random walk would give $\sigma = 1/\sqrt{2N}$, where N is the multiplicity of the event. Assuming a Gaussian distribution of error, r, the probability distribution of angle error, $(\psi_m-\psi_r)$ is then

$$\frac{dP}{d(m(\psi_m-\psi_r))} = \int \frac{v'_m dv'_m}{2\pi\sigma} \exp\left(-\frac{v_m^2}{2\sigma^2} - \frac{v_m'^2}{2\sigma^2} + \frac{v_m v'_m \cos(m(\psi_m-\psi_r))}{\sigma^2}\right) \qquad (4.1)$$

as given by [Poskanzer and Voloshin, 1998] where m is the order of the flow and where the exponent term is $e^{-r^2/2\sigma^2}$. The value of r is from the law of cosines. The $v'_m dv'_m$ is proportional to the probability of $\vec{V}'_m$ ending in the hatched area in Figure 4.2. The integrand of (4.1) is the product of these two independent probabilities.

The average, $\langle \cos m(\Psi_m - \Psi_r) \rangle$, is the integral of ($\cos m(\Psi_m - \Psi_r)$ times the probability of ($\Psi_m - \Psi_r$), (4.1)), divided by the integral of (4.1). For the present case of determining the reaction plane from the same order as the order of flow being determined (*i.e.* k = 1 in [Poskanzer and Voloshin, 1998]), the result is

$$\left\langle \cos m(\Psi_m - \Psi_r \right\rangle = \frac{\sqrt{\pi}}{2\sqrt{2}} \chi_m e^{\left(-\chi_m^2/4\right)} \left[I_o\left(\frac{\chi_m^2}{4}\right) + I_1\left(\frac{\chi_m^2}{4}\right) \right] \qquad (4.2)$$

where

$$\chi_m \equiv \frac{v_m}{\sigma} = v_m \sqrt{2N}\,, \qquad (4.3)$$

and where I_p is the modified Bessel function of order p. Figure 4.3, shows a plot of $\langle \cos m(\Psi_m - \Psi_r) \rangle$ versus χ_m for m = 1 and m = 2 (m being the flow harmonic). This average cosine is the factor by which flow is reduced when projecting it onto these wrongly oriented reaction planes.

In order to determine χ_m experimentally, all particles found in each event are randomly divided into two equally populated subevents. Then two subevent apparent reaction plane angles, Φ_A and Φ_B, are calculated. The difference between these two angles is $\Delta\Phi_{AB} = \Phi_A - \Phi_B$. The mean value, $\langle \cos \Delta\Phi_{AB} \rangle$, is

$$\langle \cos \Delta\Phi_{AB} \rangle = \langle \cos(\Phi_A - \Phi_B) \rangle$$
$$\Rightarrow \langle \cos \Delta\Phi_{AB} \rangle = \langle \cos[(\Phi_A - \Psi_r) - (\Phi_B - \Psi_r)] \rangle$$
$$\Rightarrow \langle \cos \Delta\Phi_{AB} \rangle = \langle \cos(\Phi_A - \Psi_r)\cos(\Phi_B - \Psi_r) - \sin(\Phi_A - \Psi_r)\sin(\Phi_B - \Psi_r) \rangle$$
$$\Rightarrow \langle \cos \Delta\Phi_{AB} \rangle = \langle \cos(\Phi_A - \Psi_r)\cos(\Phi_B - \Psi_r) \rangle - \langle \sin(\Phi_A - \Psi_r)\sin(\Phi_B - \Psi_r) \rangle$$

Since the average of sine terms vanishes due to reflection symmetry of the distribution,

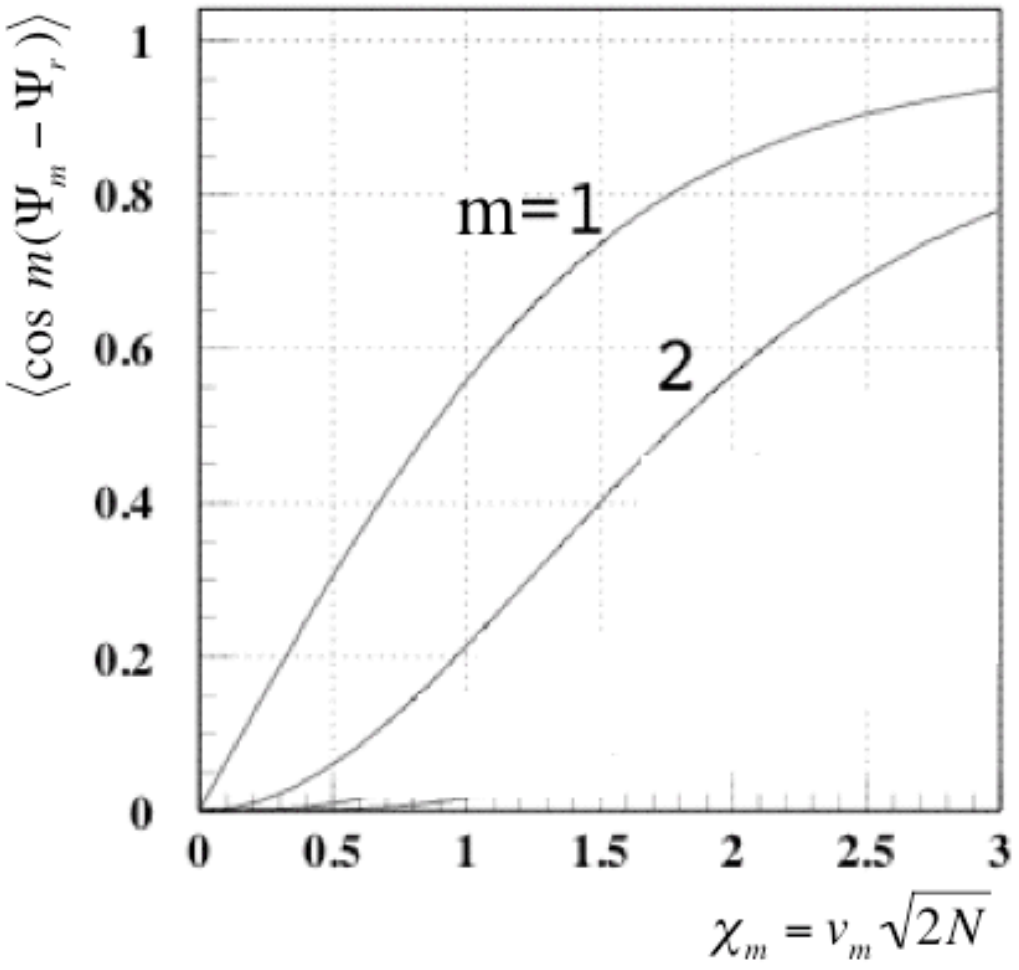

Figure 4.3: A plot of <cos m(Ψ_m-Ψ_r)> in (4.2) versus χ_m for m = 1 and m = 2 [Poskanzer and Voloshin, 1998].

and the two subevent plane angles are statistically independent of one another we can write

$$\left\langle \cos \Delta\Phi_{AB} \right\rangle = \left\langle \cos\left(\Phi_A - \Psi_r\right) \right\rangle \left\langle \cos\left(\Phi_B - \Psi_r\right) \right\rangle \tag{4.4}$$

Since every event is statistically the same as each of its subevents, apart from double the multiplicity, each factor on the right side of (4.4) should equal (4.2) but with subevent χ_m smaller by the factor $1/\sqrt{2}$. Thus

$$\chi_A = \chi_B = \chi_m \Big/ \sqrt{2} \tag{4.5}$$

where χ_m is (4.3) with the full event multiplicity, N.

The following method is used in the data analysis to correct for event plane resolution. First, $\langle \cos \Delta\Phi_{AB} \rangle$ is calculated from the subevents using all events. That value of $\langle \cos \Delta\Phi_{AB} \rangle$ is used on the y-axis of Figure 4.3 to find a tentative value of χ from the curve of appropriate flow order. That tentative value of χ is multiplied by $\sqrt{2}$ for use on the abscissa of Figure 4.3 to find the value of $\langle \cos m(\Psi_m - \Psi_r) \rangle$ from the same curve of appropriate flow order. This $\langle \cos m(\Psi_m - \Psi_r) \rangle$ is used in (4.6) to find the corrected value, v_m, from the observed flow value, v_{obs}, as

$$v_m = \frac{v_{obs}}{\left\langle \cos m(\Psi_m - \Psi_r) \right\rangle} \tag{4.6}$$

The cosine function will always be less than one giving $v_m > v_{obs}$. We could perform an overall check by using the data without employing subevents and running it through these equations, but that will not be done here.

4.3 Acceptance Corrections

Acceptance was determined by defining four different categories. The categories were called: the far west, the west, the east, and the far east. The far west region included particle tracks that had a pseudorapidity value greater than zero and an event vertex greater than zero in the z-direction. The west region included particle tracks that had a pseudorapidity value greater than zero and a vertex less than zero in the z-direction. The east region included particle tracks that had a pseudorapidity value less than zero and a vertex greater than zero in the z-direction. The far east region included particle tracks that had a pseudorapidity value less than zero and a vertex less than zero in the z-direction. Thus, tracks from any given event would fill only two of these acceptance categories, either east and far west or west and far east.

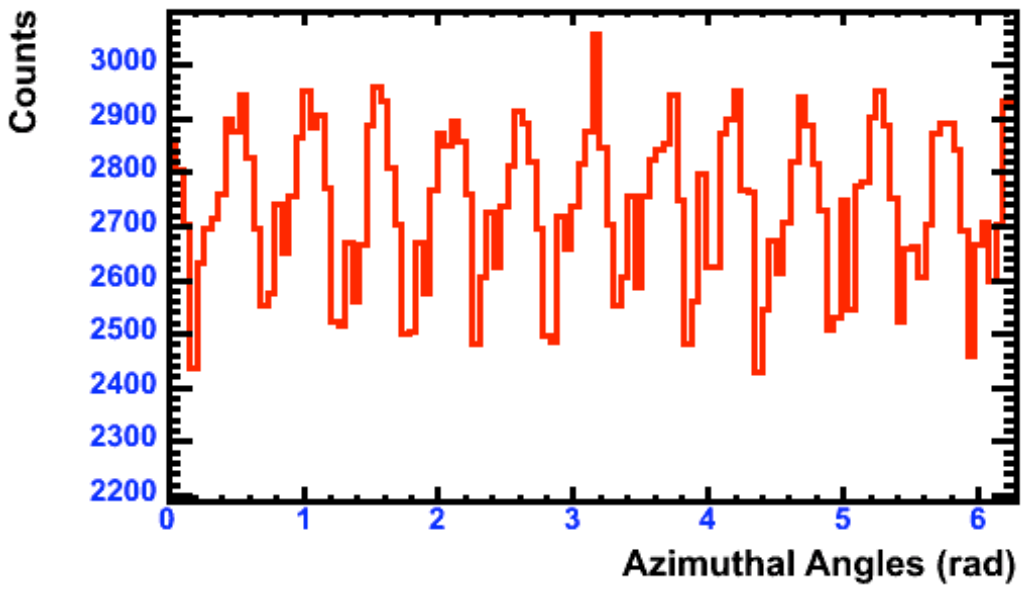

Figure 4.4: A histogram plot of counts in the far east region of the TPC before incorporation of the acceptance correction weighting file.

An acceptance correction weighting file was created over all events with the first pass of the data, and the analysis was re-run to incorporate this acceptance file. The

acceptance correction weighting file is a file that contains the sum yield of particles in all events over bins in p_T, η, and azimuthal angle. The reciprocal of this file is used on an event-by-event basis on the second run to correct for particles unobserved by the detectors. Figure 4.4 shows a histogram plot of the far east region before incorporating the acceptance correction weighting file. Note that there are twelve dips due to the sector boundaries.

After the acceptance correction weighting file was introduced this led to a much flatter overall particle yield. Figure 4.5 shows a histogram plot of the far east region after incorporating the acceptance correction weighting file. Note that the sector boundary dips are now much less pronounced due to the acceptance correction weighting file now accounting for the unobserved particles.

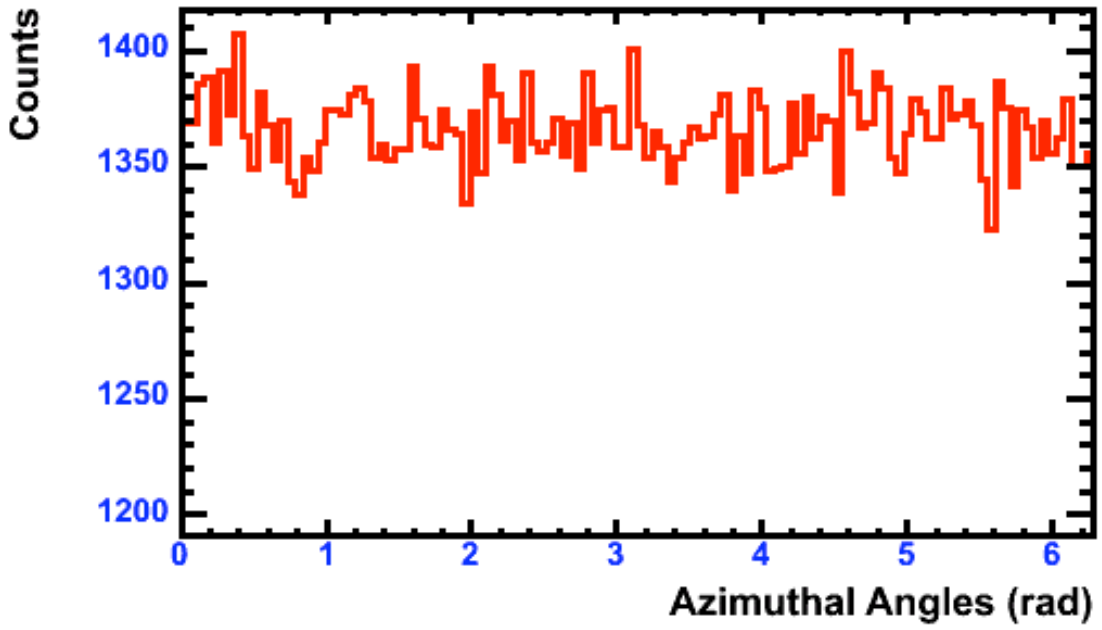

Figure 4.5: A histogram plot of counts in the far east region of the TPC after incorporation of the acceptance correction weighting file.

4.4 Centrality of Events

The collision events at RHIC run the gamut from head-on collisions to barely grazing peripheral collisions, depending on the impact parameter. Centrality is the measure of how central the collision is. This is usually measured by analyzing the multiplicity of the given collision event. Elliptic flow is highly correlated with centrality (*e.g.* elliptic flow must be zero for central collisions) [Sorge, 1999]. Thus, dividing the collision events into different centrality bins will assist us in performing a meaningful analysis.

Centrality was determined to be in one of five bins. In order to avoid a correlation between the z vertex and multiplicity, only tracks that had a pseudorapidity between –0.75 and 0.75 were considered when determining centrality. Events were lumped into centrality bins corresponding to between 12 and 48 tracks, 48 and 115 tracks, 115 and 248 tracks, and bin 4, those with over 248 tracks. Bin 4 is the bin with the most central collisions, bin 3 is the bin with semi-central collisions, bin 2 is the bin with semi-peripheral collisions, and bin 1 is the bin with peripheral collisions. Figure 4.6 shows a histogram plot with the different bin divisions. The x (N_{ch}) axis and the y (number of events) axis at 130 GeV and 200 GeV were scaled to the 19.6 GeV maximum [Picha 2003]. The most peripheral events (*i.e.* those with multiplicities less than 12) were not analyzed as it is known that there is a strong trigger bias for these events. Strong trigger bias means that some centralities were preferred in the trigger setting. This caused these results to be more biased towards the 50%–70% impact parameter results than a true minimum bias data set.

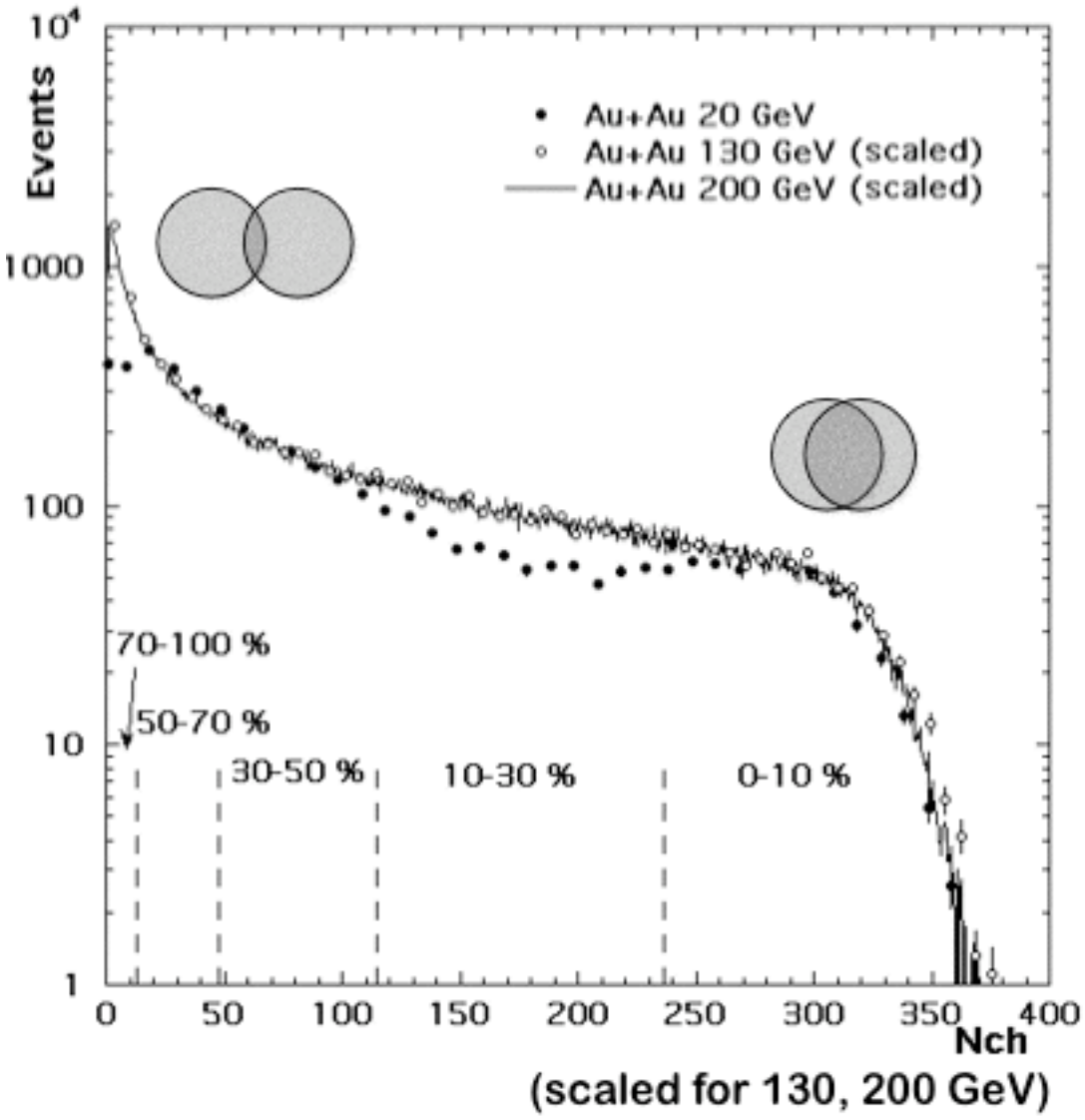

Figure 4.6: A histogram plot with the different bin divisions [Picha 2003].

Bin 1 corresponds to collisions that contain 50% to 70% centrality (70% centrality is a conventional bin which really means 70% of the yield curve as in Figure 4.6). Bin 2 corresponds to collisions that contain 30% to 50% centrality. Bin 3 corresponds to collisions that contain 10% to 30% centrality. Bin 4 corresponds to collisions that contain 0% to 10% centrality [Cebra 2002].

Chapter 5

Flow Results

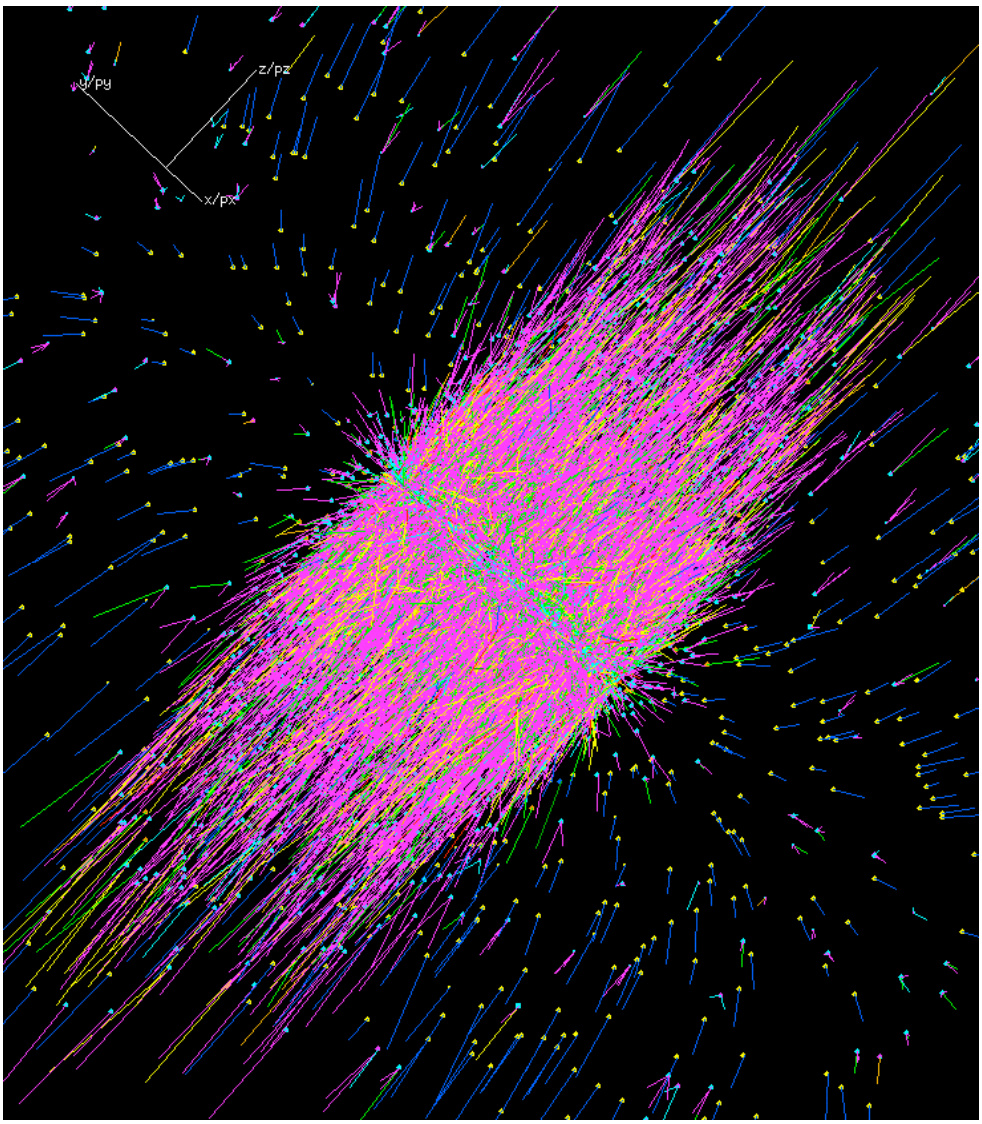

Figure 5.1: A violent collision fireball [STAR 2006].

5.1 Analysis

We now try to extract multiple moments flow values from this violent collision. Figure 5.1 shows a violent collision fireball. In order to extract the proper information from this analysis that may be compared to previous and future experiments, "classic plots" have been generated for different particle species and centrality ranges. These plots include both directed flow (v_1) and elliptic flow (v_2) which are plotted against either pseudorapidity (η) or transverse momentum (p_T). Systematic errors are included in the error bars of all the plots in this thesis.

5.2 Plots with All Particles

The plots in this section are generated by examining the cumulative effects of all particles in the analysis. PID was not used in this analysis. These particles must have had a transverse momentum between 0.1 GeV/c and 4.0 GeV/c and a pseudorapidity between –1.3 and 1.3 units.

The events were separated into four separate centrality bins: peripheral events which represent 50% to 70% centrality, semi-peripheral events which represent 30% to 50% centrality, semi-central events which represent 10% to 30% centrality, and central events which represent the top 10% central events. The most peripheral bin (70% to 100% centrality) was not used in this analysis due to the low overall event multiplicity which made extracting meaningful physics virtually impossible, and because there was a strong trigger bias for events in this centrality range.

For all of the plots in this section, a trendline curve was added to the graph that is only meant to guide the eye. The rather large error bars on all of the plots in this section are due to lack of statistics.

5.2.1 Peripheral Events

This sub-section deals with peripheral events (50% to 70% centrality). This centrality bin contained 12,337 events that passed all of the cuts.

Figure 5.2 shows a plot of directed flow (v_1) versus pseudorapidity for peripheral events in STAR for all particles. In order to reduce fluctuations, the data are averaged, inverted, and reflected about mid-rapidity. The trendline curve is forced through a flow value of zero at $\eta = 0$. The peak value for directed flow is approximately 4% in the highest pseudorapidity bins. The slope of the trendline curve is -4.5 ± 1.4.

Note that the sign of the slope for directed flow is negative. The sign of the slope for directed flow here is assumed to be the same as it was at the SPS, which measured the sign of directed flow of protons to be positive near beam rapidity for peripheral collisions

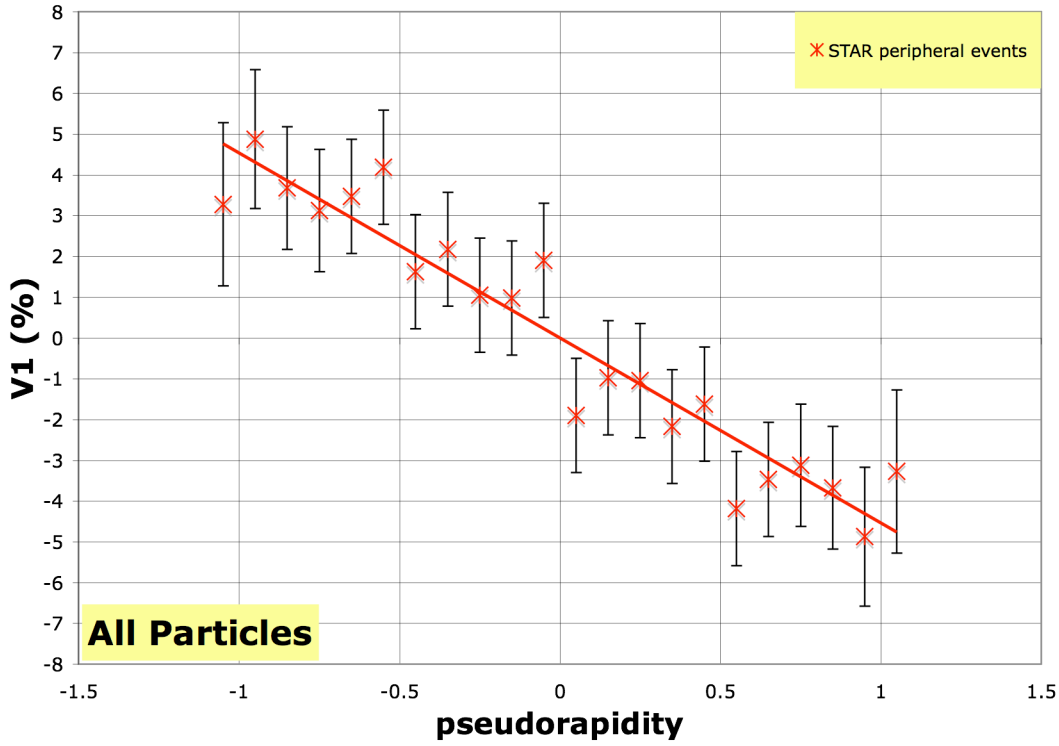

Figure 5.2: A plot of directed flow (v_1) versus pseudorapidity for peripheral events in STAR for all particles.

[Alt 2003]. Directed flow will have the opposite sign on either side of mid-rapidity due to the spectator nucleons. As particles leave the interaction region they will be preferentially redirected as they scatter off of the exiting spectator nucleons.

Figure 5.3 shows a plot of elliptic flow (v_2) versus pseudorapidity for peripheral events in STAR for all particles. In order to reduce fluctuations, the data are averaged and reflected about mid-rapidity. In this plot the trendline curve is a fourth-order polynomial. The average value for flow is around 6% for most of the bins around mid-rapidity. The magnitude of v_2 is maximum at a value of $\eta = 0$.

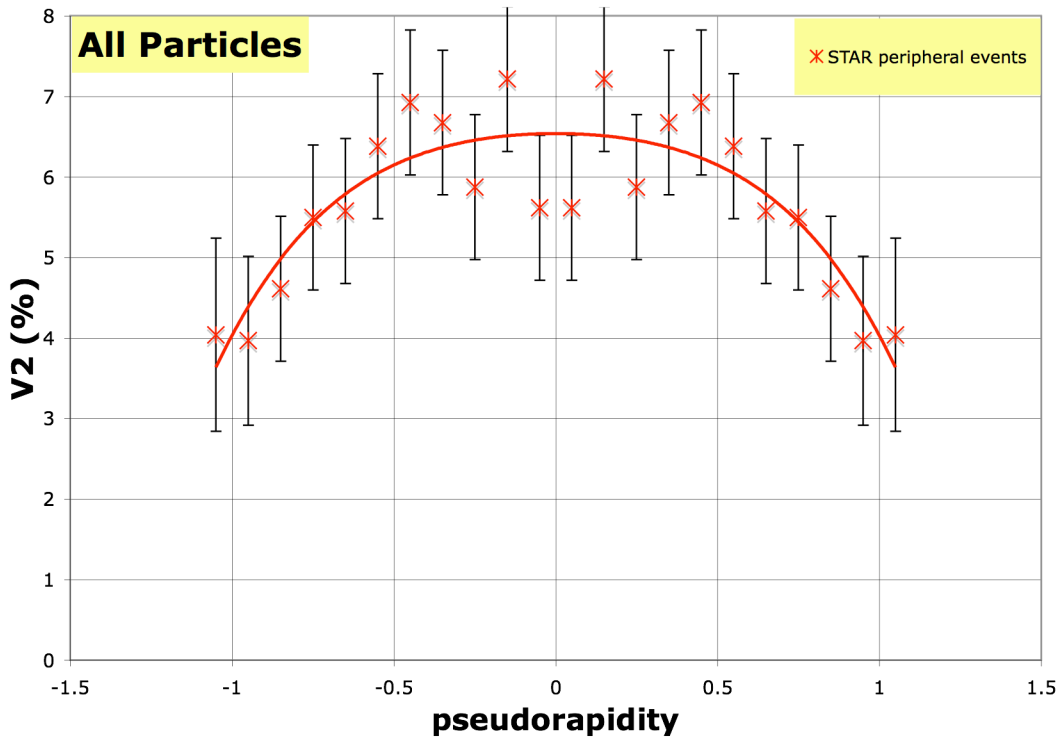

Figure 5.3: A plot of elliptic flow (v_2) versus pseudorapidity for peripheral events in STAR for all particles.

Figure 5.4 shows a plot of directed flow (v_1) versus transverse momentum (p_T) for peripheral events STAR for all particles. As the transverse momentum increases, the statistics in the transverse momentum histogram bins decrease rapidly. The sign for directed flow was determined as it was at the SPS, which measured the sign of v_1 of protons to be positive near beam rapidity for peripheral collisions [Alt 2003]. The particles exhibit a negative flow over the entire transverse momentum region.

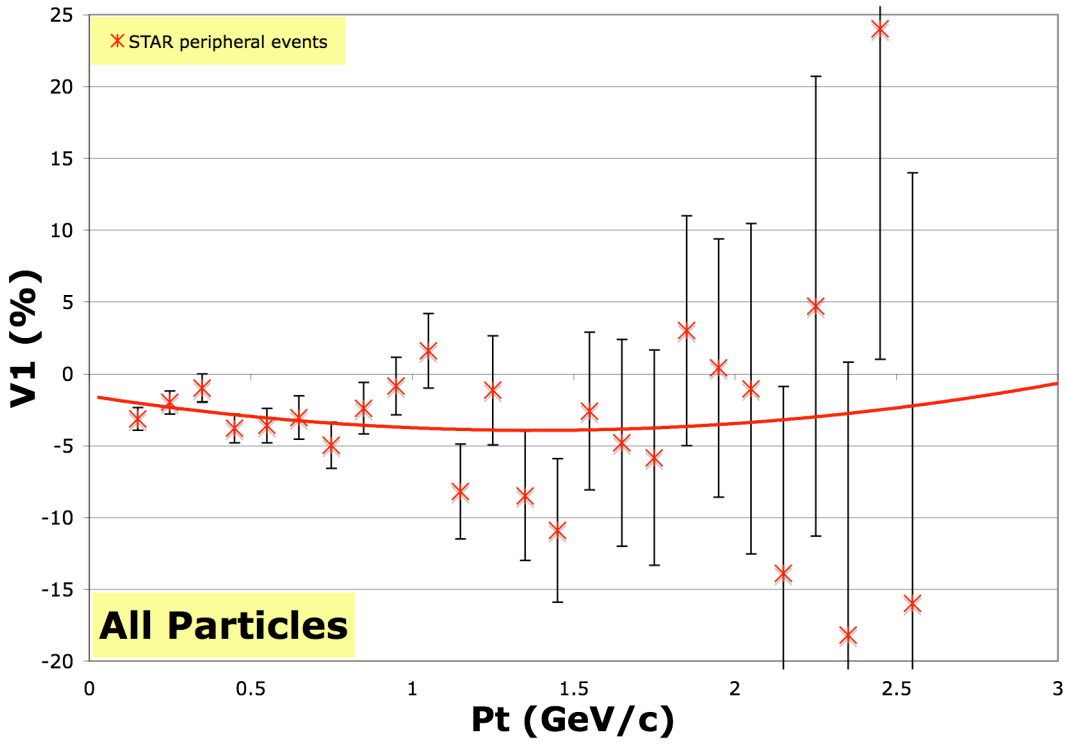

Figure 5.4: A plot of directed flow (v_1) versus transverse momentum (p_T) for peripheral events in STAR for all particles.

Figure 5.5 shows a plot of elliptic flow (v_2) versus transverse momentum (p_T) for peripheral events in STAR for all particles. As the transverse momentum increases, the statistics in the transverse momentum histogram bins decrease rapidly. The v_2 values increase with p_T up to a p_T value of 2 GeV/c. Particles associated with high p_T values are

often considered to result primarily from hard processes. These hard processes should be azimuthally isotropic and should not exhibit the same elliptic flow as seen in the soft physics dominated region below 2 GeV/c in p_T.

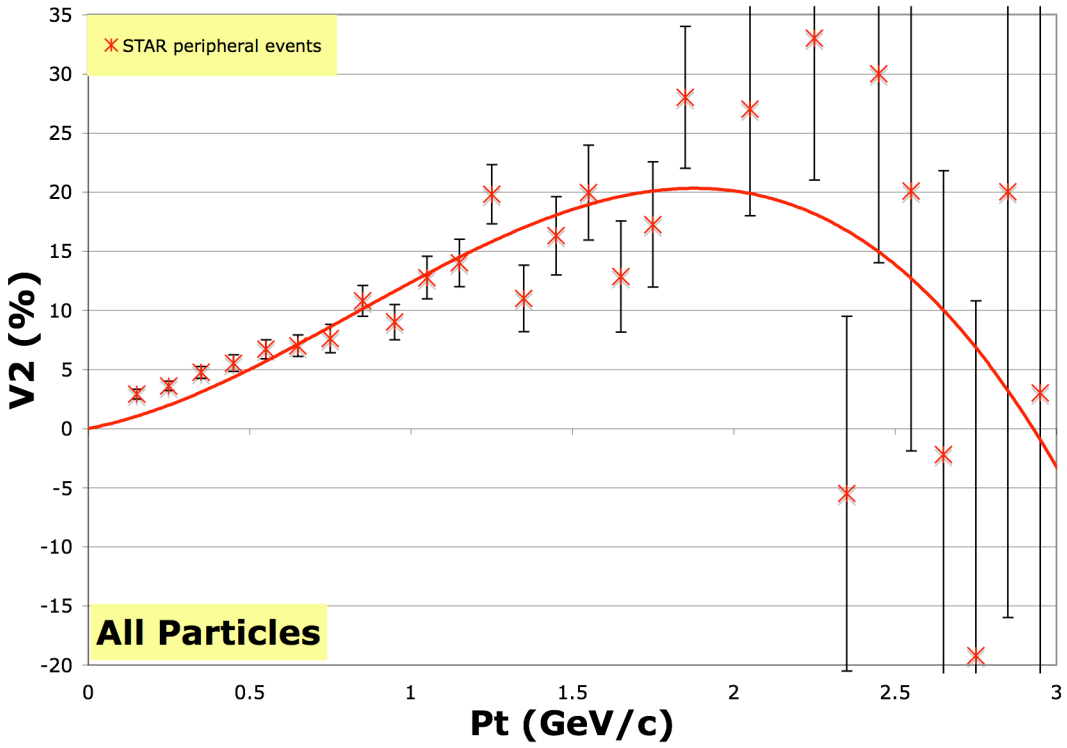

Figure 5.5: A plot of elliptic flow (v_2) versus transverse momentum (p_T) for peripheral events in STAR for all particles.

5.2.2 Semi-Peripheral Events

This sub-section deals with semi-peripheral events (30% to 50% centrality). This centrality bin contained 7,474 events that passed all of the cuts.

Figure 5.6 shows a plot of directed flow (v_1) versus pseudorapidity for semi-peripheral STAR events for all particles. In order to reduce fluctuations, the data are averaged, inverted, and reflected about mid-rapidity. The trendline curve is forced

through a flow value of zero at $\eta = 0$. The value for directed flow is approximately 3% in the higher pseudorapidity bins. The slope of the trendline curve is -3.5 ± 1.4.

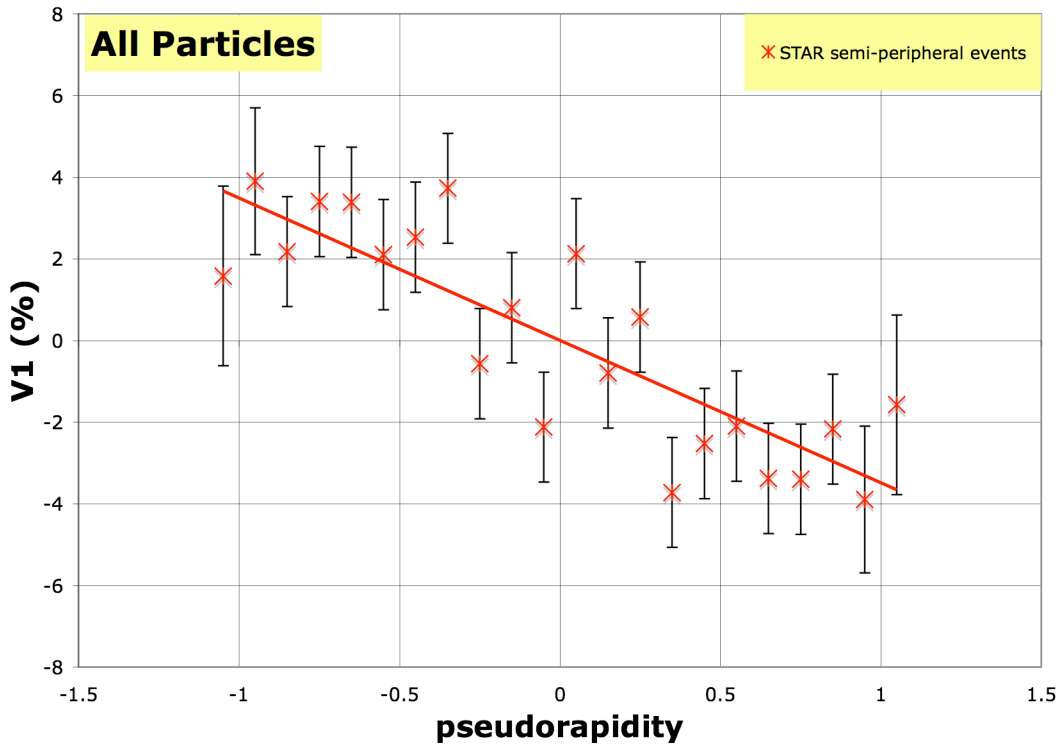

Figure 5.6: A plot of directed flow (v_1) versus pseudorapidity for semi-peripheral events in STAR for all particles.

Figure 5.7 shows a plot of elliptic flow (v_2) versus pseudorapidity for semi-peripheral events in STAR for all particles. In order to reduce fluctuations, the data are averaged and reflected about mid-rapidity. In this plot the trendline curve is a fourth-order polynomial. The average value for flow is about 5.5% for most of the bins around mid-rapidity. The magnitude of v_2 is maximum at a value of $\eta = 0$.

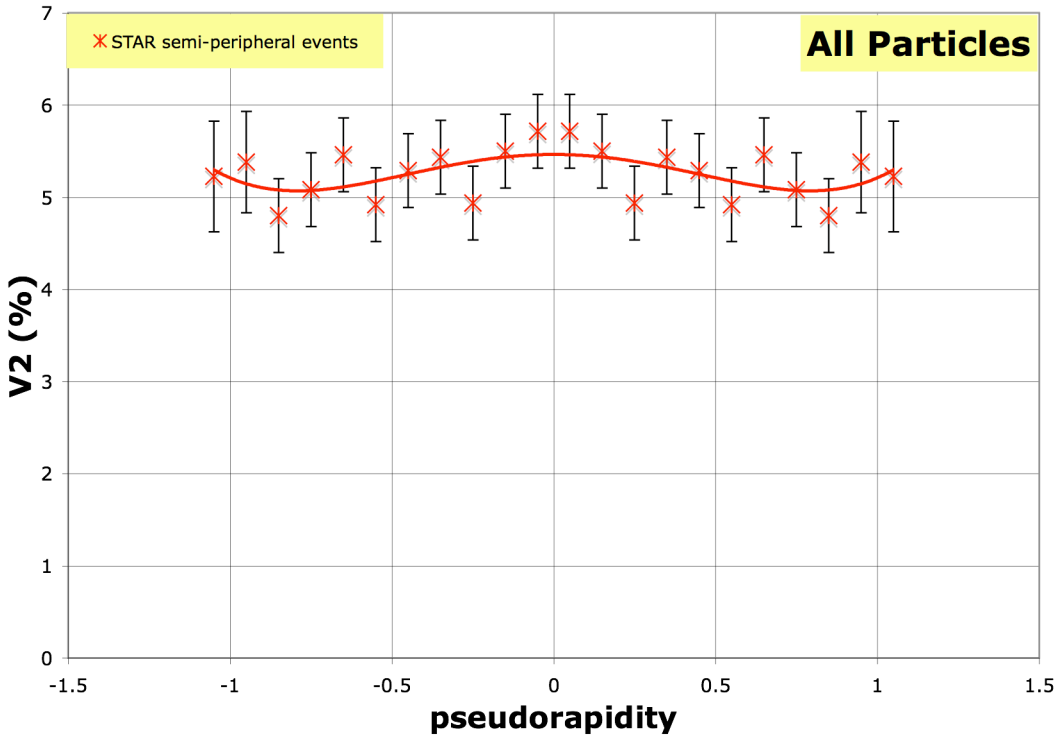

Figure 5.7: A plot of elliptic flow (v_2) versus pseudorapidity for semi-peripheral events in STAR for all particles.

Figure 5.8 shows a plot of directed flow (v_1) versus transverse momentum (p_T) for semi-peripheral events in STAR for all particles. As the transverse momentum increases, the statistics in the transverse momentum histogram bins decrease rapidly. Positive flow is defined as the direction of proton flow. The particles exhibit a negative flow in the low transverse momentum region.

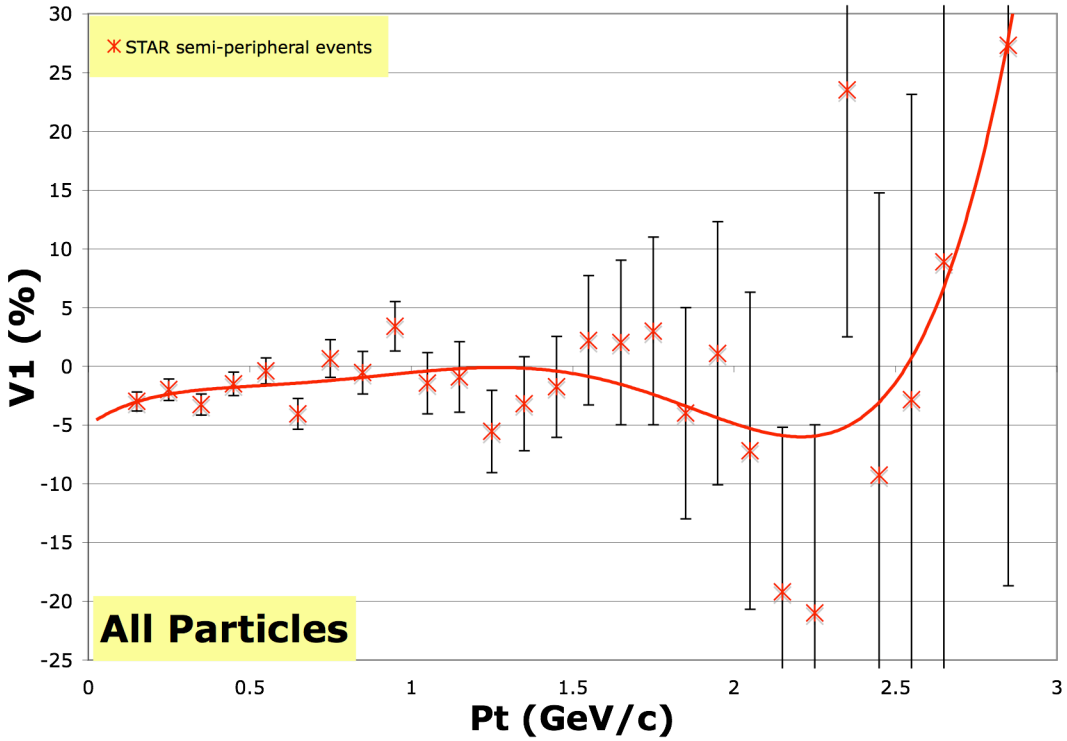

Figure 5.8: A plot of directed flow (v_1) versus transverse momentum (p_T) for semi-peripheral events in STAR for all particles.

Figure 5.9 shows a plot of elliptic flow (v_2) versus transverse momentum (p_T) for semi-peripheral events in STAR for all particles. As the transverse momentum increases, the statistics in the transverse momentum histogram bins decrease rapidly. The v_2 values increase with p_T up to a p_T value of 1.5-2 GeV/c. Particles associated with high p_T values are often considered to result primarily from hard processes. These hard processes should be azimuthally isotropic and should not exhibit the same elliptic flow as seen in the soft physics dominated region below 2 GeV/c in p_T.

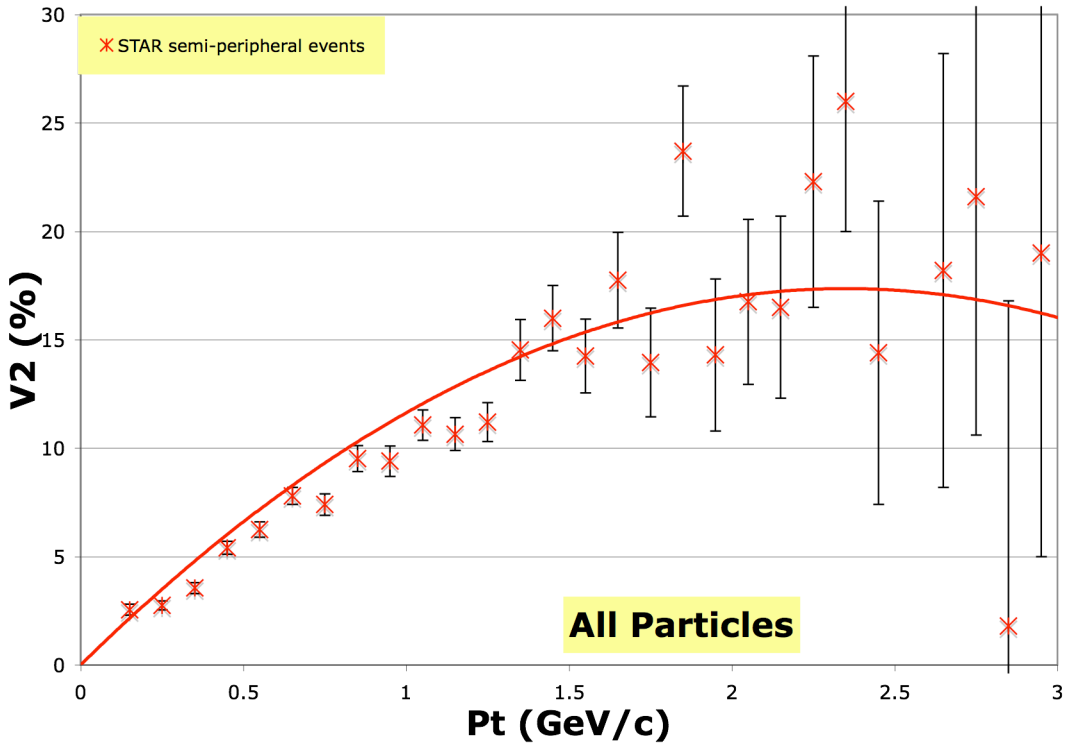

Figure 5.9: A plot of elliptic flow (v_2) versus transverse momentum (p_T) for semi-peripheral events in STAR for all particles.

5.2.3 Semi-Central Events

This sub-section deals with semi-central events (10% to 30% centrality). This centrality bin contained 5,661 events that passed all of the cuts.

Figure 5.10 shows a plot of directed flow (v_1) versus pseudorapidity for semi-central events in STAR for all particles. In order to reduce fluctuations, the data are averaged, inverted, and reflected about mid-rapidity. The trendline curve is forced through a flow value of zero at $\eta = 0$. The value for directed flow is around 4% in the higher pseudorapidity bins (with an anomalous point of 8%). The slope of the trendline curve is -5.0 ± 2.7.

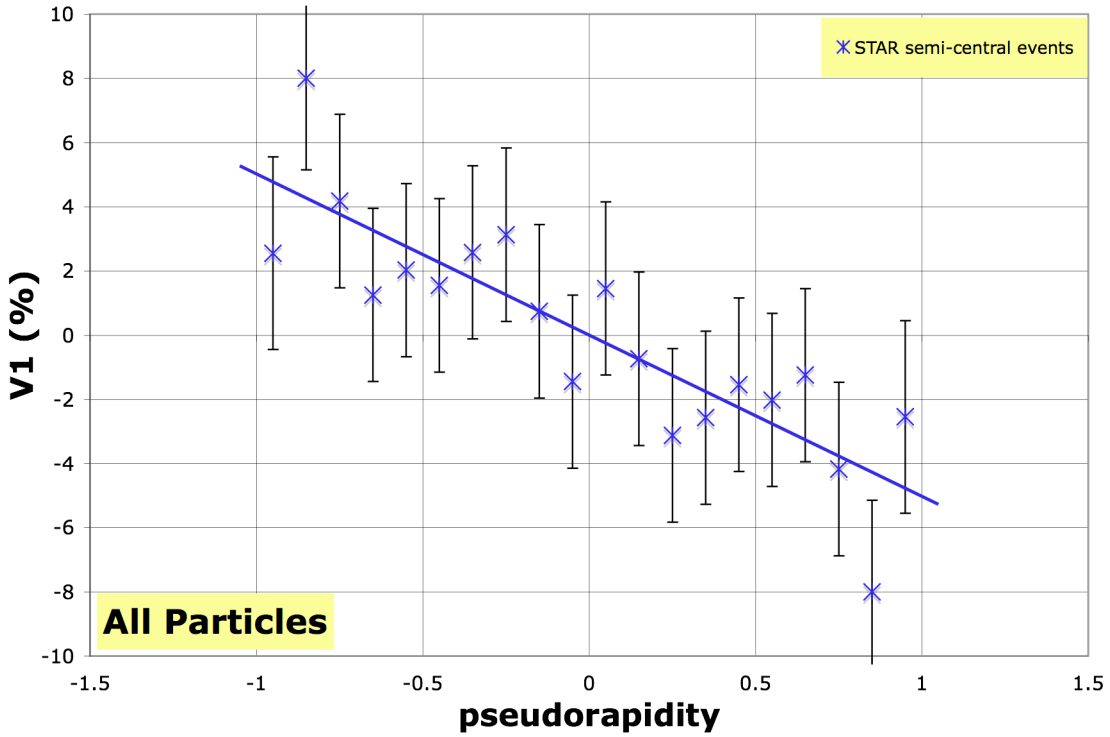

Figure 5.10: A plot of directed flow (v_1) versus pseudorapidity for semi-central events in STAR for all particles.

Figure 5.11 shows a plot of elliptic flow (v_2) versus pseudorapidity for semi-central events STAR for all particles. In order to reduce fluctuations, the data are averaged and reflected about mid-rapidity. In this plot the trendline curve is a fourth-order polynomial. The average value for flow is just below 4% for most of the bins around mid-rapidity.

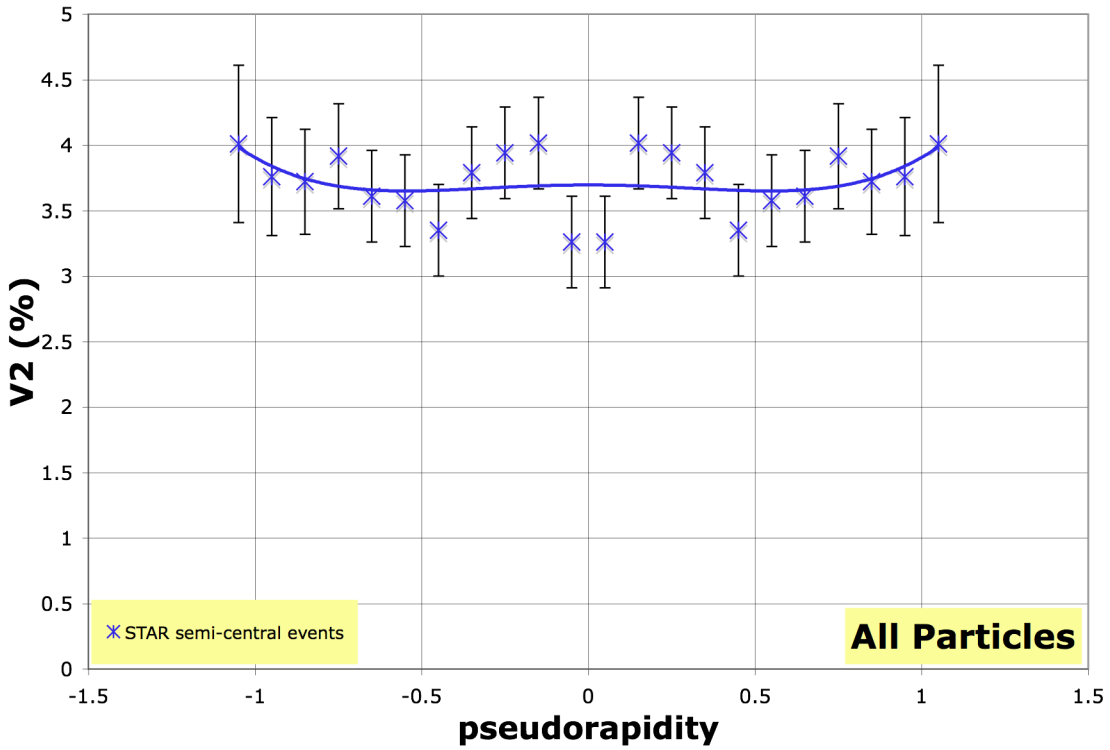

Figure 5.11: A plot of elliptic flow (v_2) versus pseudorapidity for semi-central events in STAR for all particles.

Figure 5.12 shows a plot of directed flow (v_1) versus transverse momentum (p_T) for semi-central events in STAR for all particles. As the transverse momentum increases, the statistics in the transverse momentum histogram bins decrease rapidly. Positive flow is defined as the direction of proton flow. The particles exhibit a negative flow in the low transverse momentum region.

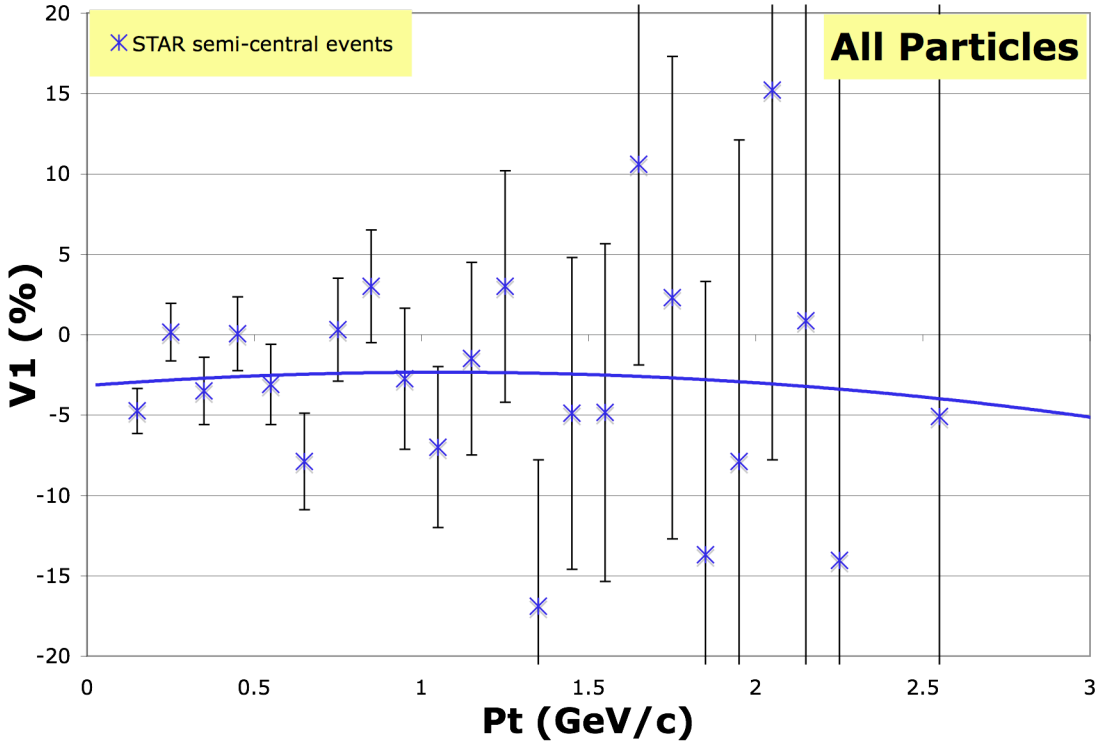

Figure 5.12: A plot of directed flow (v_1) versus transverse momentum (p_T) for semi-central events in STAR for all particles.

Figure 5.13 shows a plot of elliptic flow (v_2) versus transverse momentum (p_T) for semi-central events in STAR for all particles. As the transverse momentum increases, the statistics in the transverse momentum histogram bins decrease rapidly. The v_2 values increase with p_T up to a p_T value of 1.5-2 GeV/c. Particles associated with high p_T values are often considered to result primarily from hard processes. These hard processes should be azimuthally isotropic and should not exhibit the same elliptic flow as seen in the soft physics dominated region below 2 GeV/c in p_T.

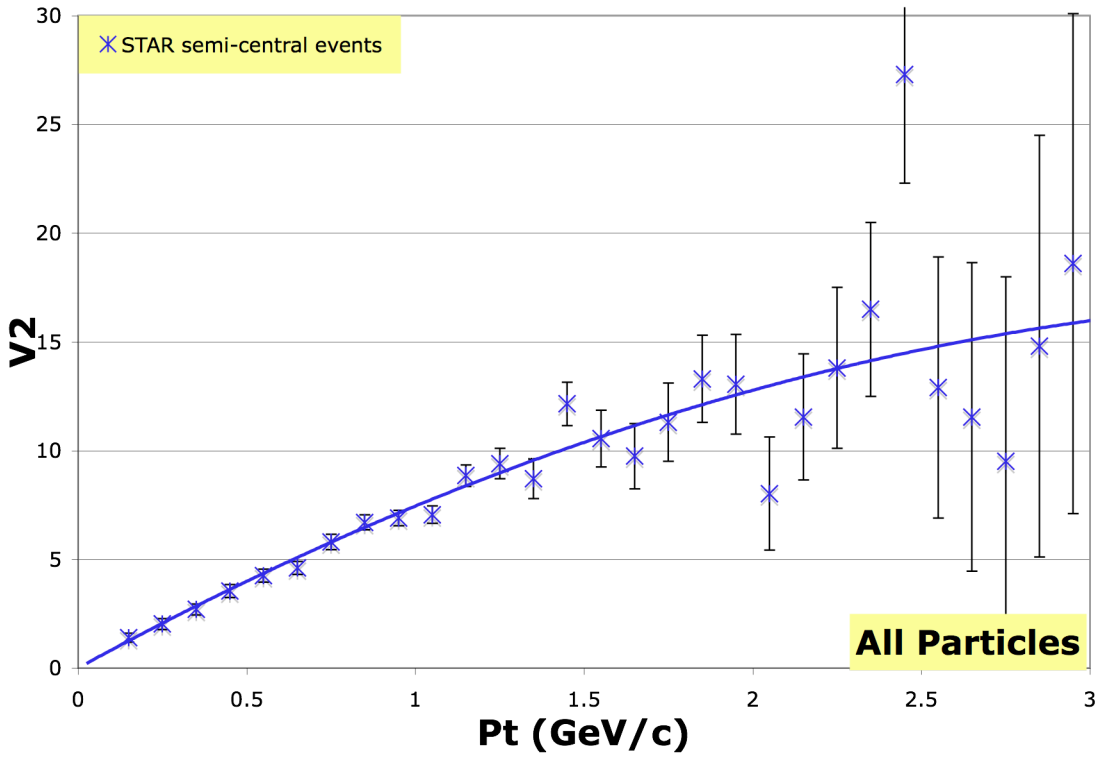

Figure 5.13: A plot of elliptic flow (v_2) versus transverse momentum (p_T) for semi-central events in STAR for all particles.

5.2.4 Central Events

This sub-section deals with central events (top 10% centrality). This centrality bin contained 3,592 events that passed all of the cuts.

Figure 5.14 shows a plot of directed flow (v_1) versus pseudorapidity for central events in STAR for all particles. In order to reduce fluctuations, the data are averaged, inverted, and reflected about mid-rapidity. There is no slope to the directed flow data, even the higher pseudorapidity bins consistently have zero directed flow. The trendline curve is forced through a flow value of zero at $\eta = 0$. The slope of the trendline curve is -0.21 ± 1.0.

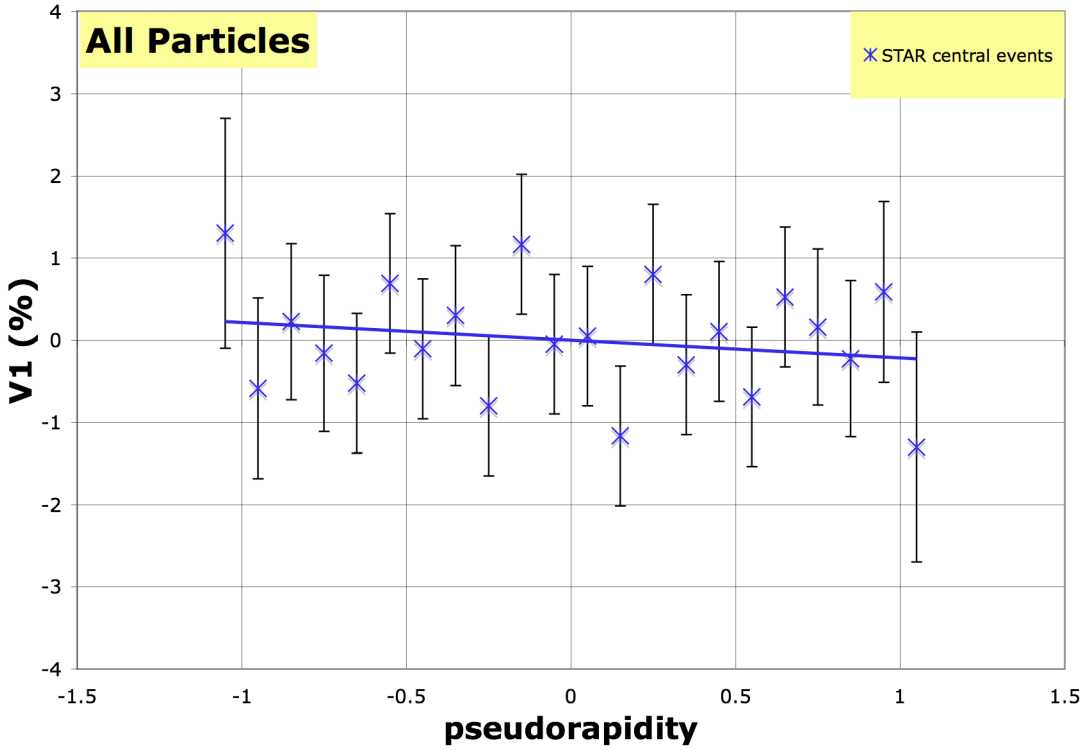

Figure 5.14: A plot of directed flow (v_1) versus pseudorapidity for central events in STAR for all particles.

Figure 5.15 shows a plot of elliptic flow (v_2) versus pseudorapidity for central events in STAR for all particles. In order to reduce fluctuations, the data are averaged and reflected about mid-rapidity. In this plot the trendline curve is a second-order polynomial. The average value for flow is nearly just below 2% for most of the bins around mid-rapidity.

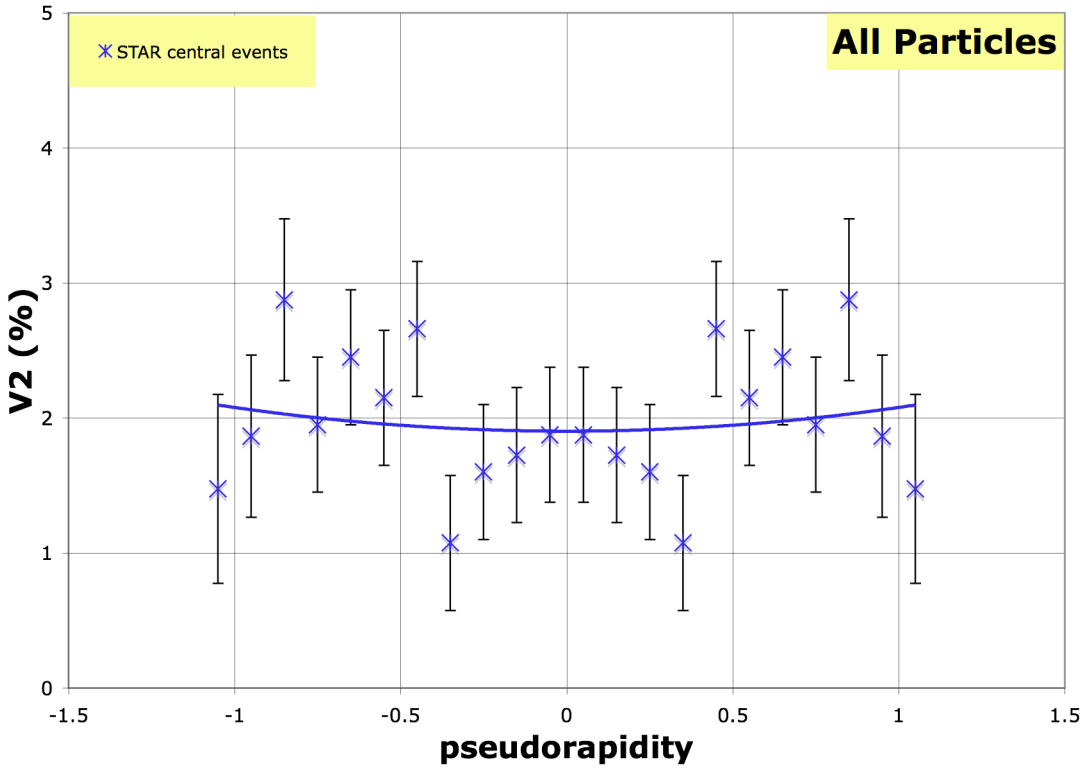

Figure 5.15: A plot of elliptic flow (v_2) versus pseudorapidity for central events in STAR for all particles.

Figure 5.16 shows a plot of directed flow (v_1) versus transverse momentum (p_T) for central events in STAR for all particles. As the transverse momentum increases, the statistics in the transverse momentum histogram bins decrease rapidly. Positive flow is defined as the direction of proton flow. The particles exhibited no flow across the entire momentum region.

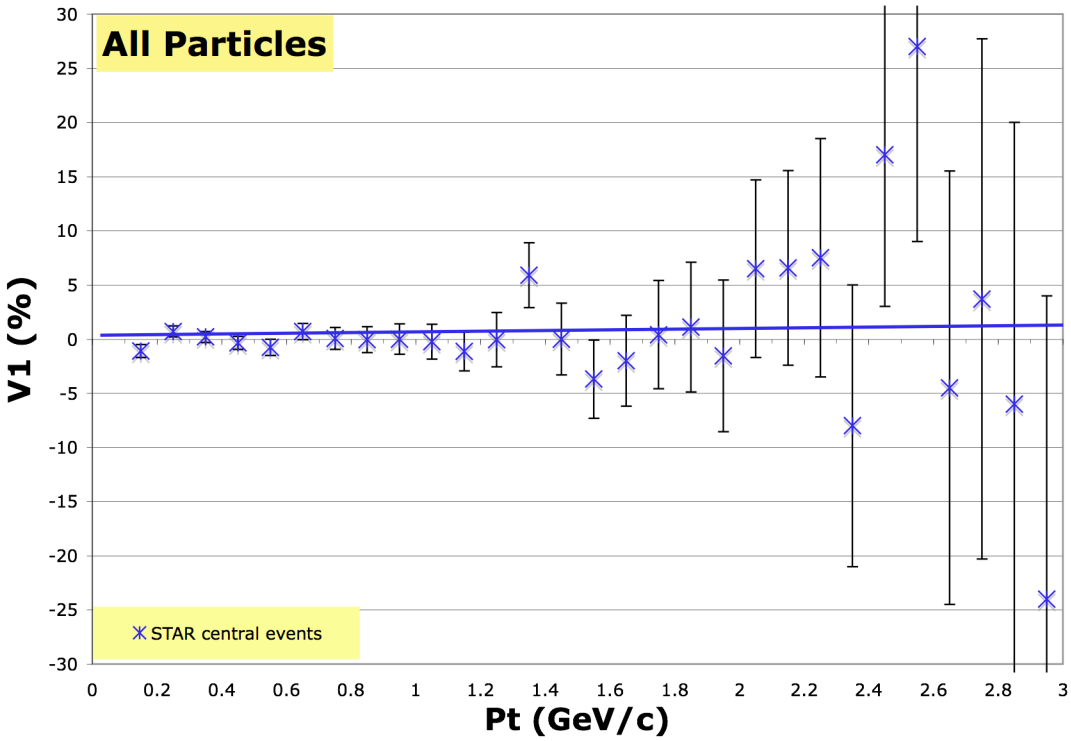

Figure 5.16: A plot of directed flow (v_1) versus transverse momentum (p_T) for central events in STAR for all particles.

Figure 5.17 shows a plot of elliptic flow (v_2) versus transverse momentum (p_T) for central events in STAR for all particles. The v_2 values increase with p_T. As the transverse momentum increases, the statistics in the transverse momentum histogram bins decrease rapidly.

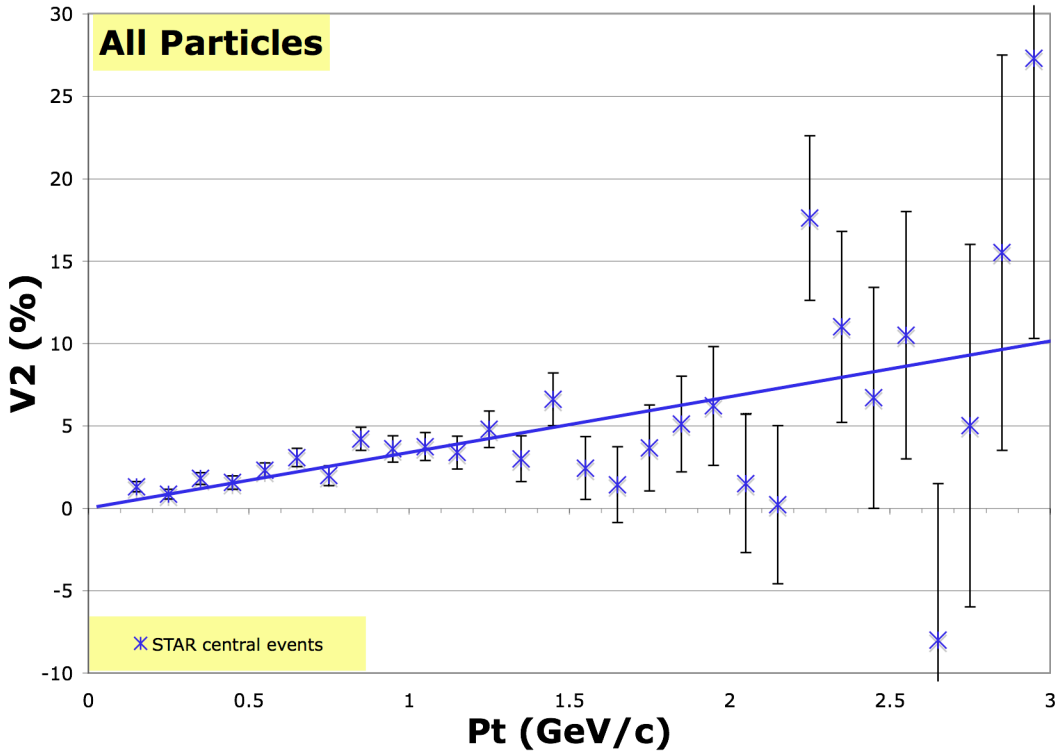

Figure 5.17: A plot of elliptic flow (v_2) versus transverse momentum (p_T) for central events in STAR for all particles.

5.2.5 Events with All Centralities

This sub-section deals with events containing all centralities (*i.e.* "minimum bias" events). Minimum bias events contained 30,983 events that passed all of the cuts. For this work, "minimum bias" means minimum software bias. The hardware trigger was not very efficient for the most peripheral and the semi-central events (10%-30%). This will cause these results to be more biased towards the 50%–70% impact parameter results than a true minimum bias data set. Caution should be used when comparing these results to other published minimum bias results.

Figure 5.18 shows a plot of directed flow (v_1) versus pseudorapidity for minimum bias events in STAR for all particles. In order to reduce fluctuations, the data are averaged, inverted, and reflected about mid-rapidity. The trendline curve is forced

through a flow value of zero at $\eta = 0$. The peak value for directed flow is just about 2% in the higher pseudorapidity bins. The data show a monotonic increase with pseudorapidity. The slope of the trendline curve is -2.4 ± 0.7.

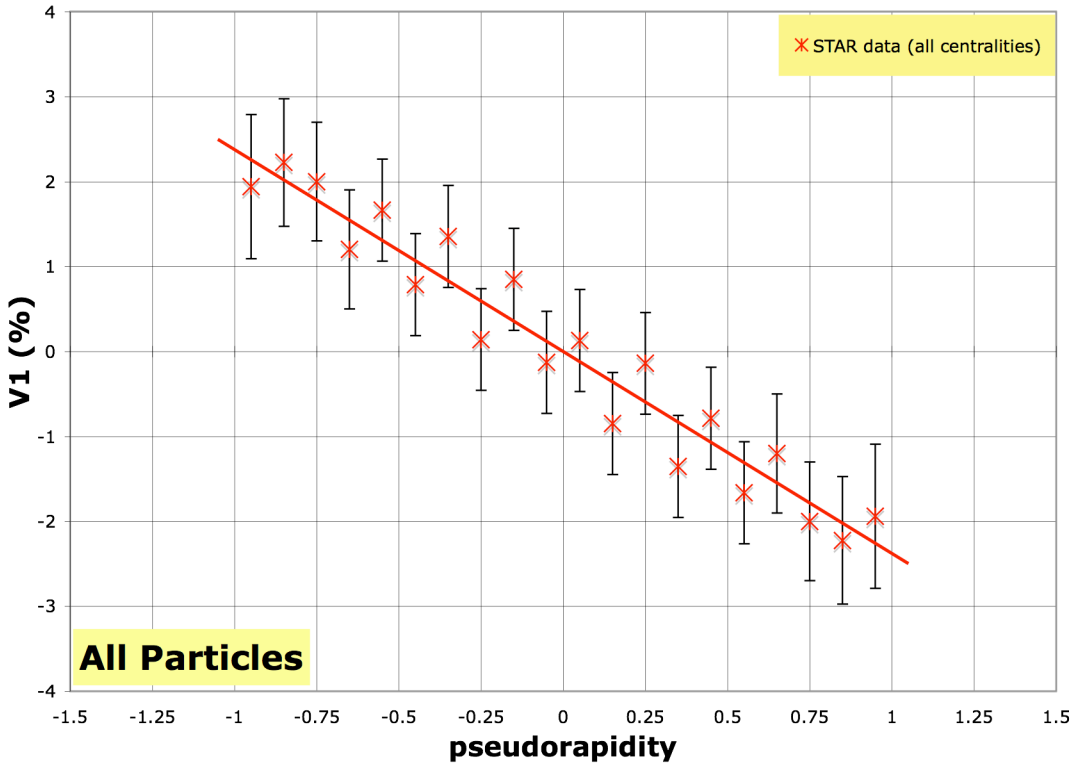

Figure 5.18: A plot of directed flow (v_1) versus pseudorapidity for minimum bias events in STAR for all particles.

Figure 5.19 shows a plot of elliptic flow (v_2) versus pseudorapidity for minimum bias events in STAR for all particles. In order to reduce fluctuations, the data are averaged and reflected about mid-rapidity. In this plot the trendline curve is a fourth-order polynomial. The average value for flow is about 4% for most of the bins around mid-rapidity. The magnitude of v_2 is maximum at a value of $\eta = 0$.

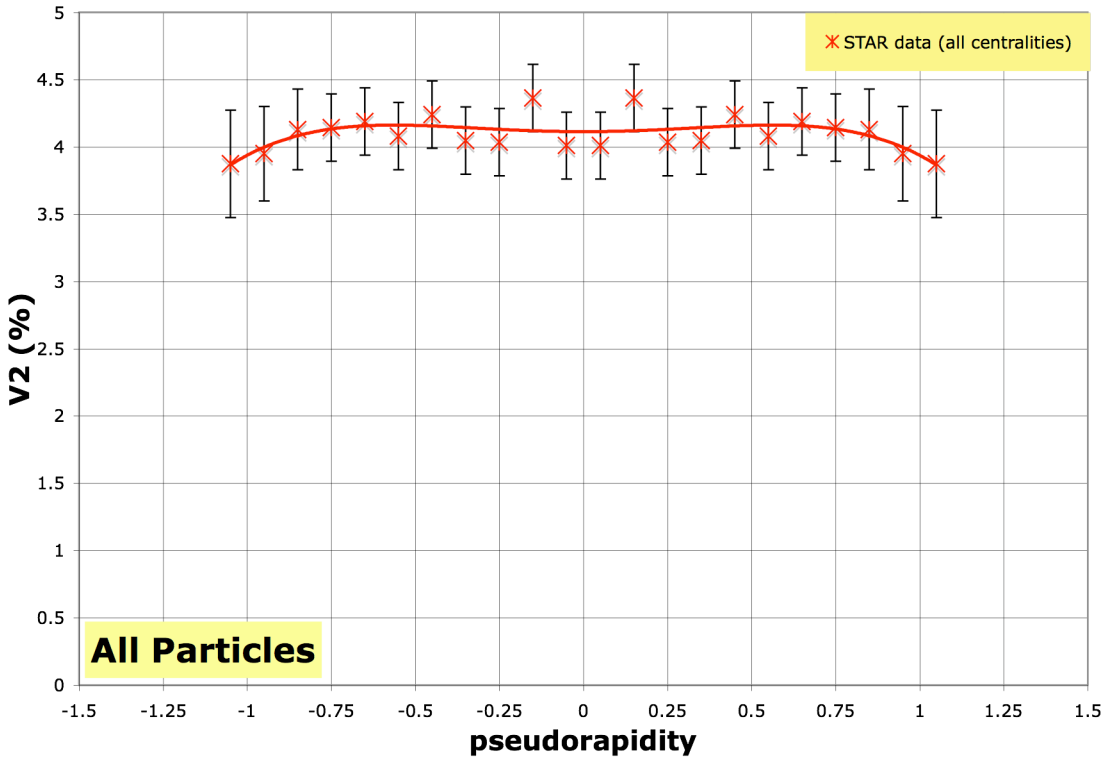

Figure 5.19: A plot of elliptic flow (v_2) versus pseudorapidity for minimum bias events in STAR for all particles.

Figure 5.20 shows a plot of directed flow (v_1) versus transverse momentum (p_T) for minimum bias events in STAR for all particles. As the transverse momentum increases, the statistics in the transverse momentum histogram bins decrease rapidly. Positive flow is defined as the direction of proton flow. The particles exhibit a negative flow in the low transverse momentum region and then moved up to positive flow (correlated with the protons) in the higher transverse momentum region.

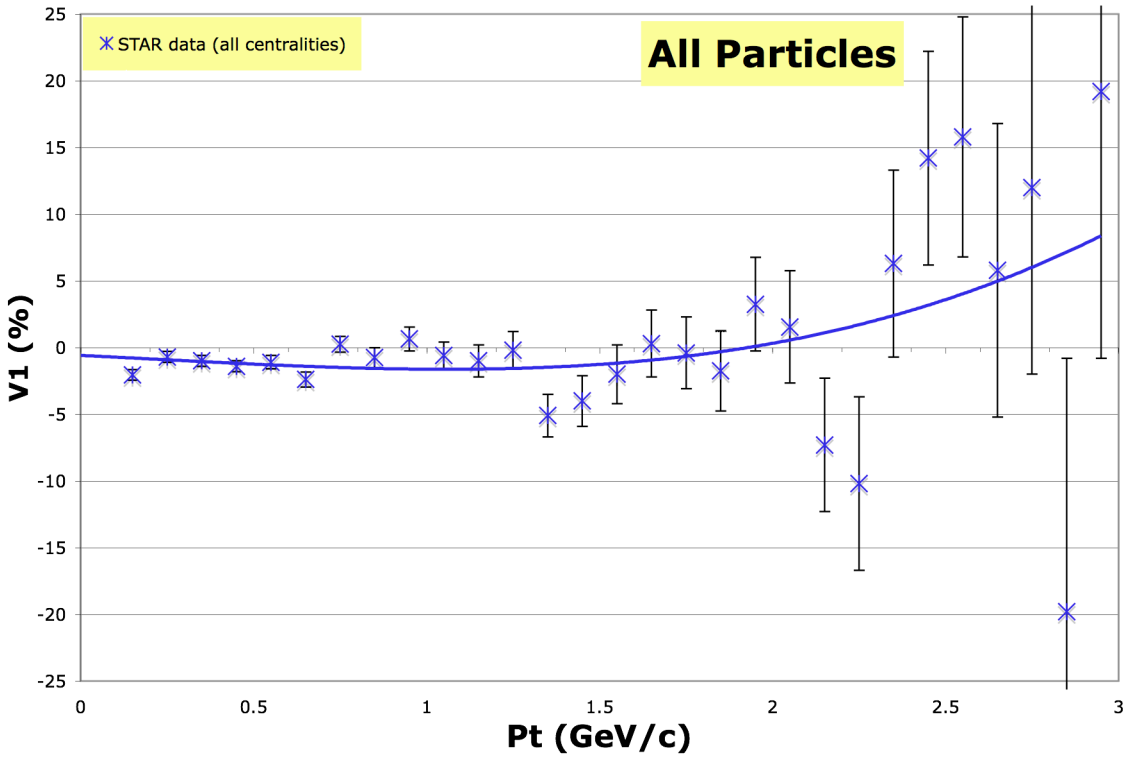

Figure 5.20: A plot of directed flow (v_1) versus transverse momentum (p_T) for minimum bias events in STAR for all particles.

Figure 5.21 shows a plot of elliptic flow (v_2) versus transverse momentum (p_T) for minimum bias events in STAR for all particles. As the transverse momentum increases, the statistics in the transverse momentum histogram bins decrease rapidly. The v_2 values increase with p_T up to a p_T value of 2 GeV/c. Particles associated with high p_T values are often considered to result primarily from hard processes. These hard processes should be azimuthally isotropic and should not exhibit the same elliptic flow as seen in the soft physics dominated region below 2 GeV/c in p_T.

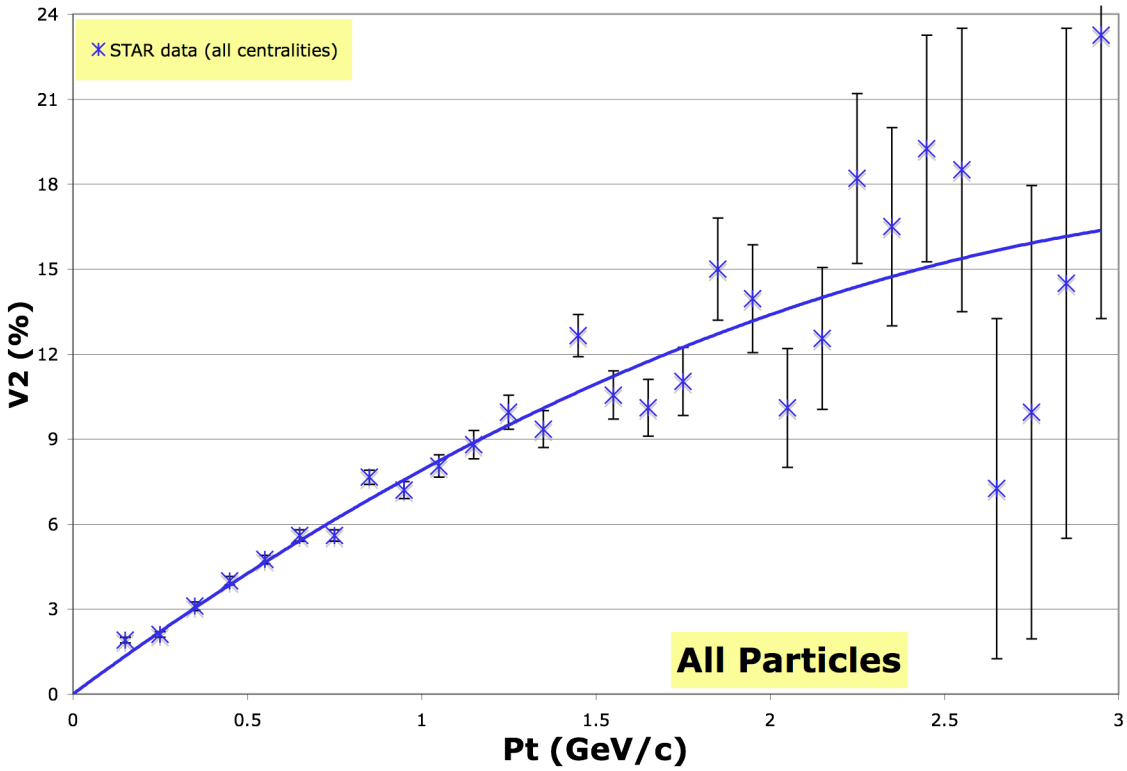

Figure 5.21: A plot of elliptic flow (v_2) versus transverse momentum (p_T) for minimum bias events in STAR for all particles.

5.3 Identified Pion Flow

The plots in this section are taken by eliminating all particles that are not identified as pions. These pions must also have had a transverse momentum between 0.1 GeV/c and 4.0 GeV/c and a pseudorapidity between –1.3 and 1.3 units.

The events were separated into four separate centrality bins: peripheral events which represent 50% to 70% centrality, semi-peripheral events which represent 30% to 50% centrality, semi-central events which represent 10% to 30% centrality, and central events which represent the top 10% central events. The most peripheral bin (70% to 100% centrality) was not used in this analysis due to the low overall event multiplicity, which made extracting meaningful physics virtually impossible.

For all of the plots in this section, a trendline curve was added to the graph that is only meant to guide the eye. The rather large error bars on all of the plots in this section are due to lack of statistics. The ratio of yields of positively charged pions to protons is about 9.0 to one. The ratio of yields of all charged pions to protons plus anti-protons is about 17 to one. The ratio of yields of positively charged kaons to protons is about 0.20 to one. Also, the ratio of yields of all charged kaons to protons plus anti-protons is about 0.35 to one.

5.3.1 Identified Pion Peripheral Events

This sub-section deals with peripheral events (50% to 70% centrality). This centrality bin contained 12,337 events that passed all of the cuts.

Figure 5.22 shows a plot of directed flow (v_1) of identified pions versus

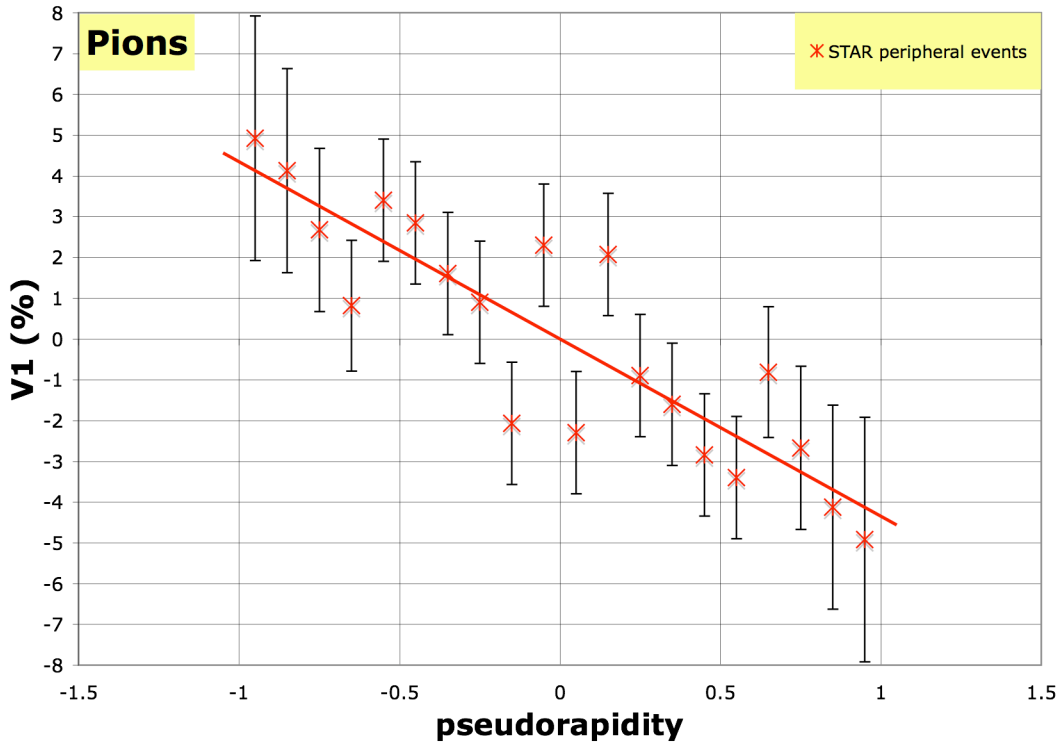

Figure 5.22: A plot of directed flow (v_1) of identified pions versus pseudorapidity for peripheral events in STAR.

pseudorapidity for peripheral events in STAR. In order to reduce fluctuations, the data are averaged, inverted, and reflected about mid-rapidity. The trendline curve is forced through a flow value of zero at $\eta = 0$. The peak value for directed flow is just below 5% in the highest pseudorapidity bin. The slope of the trendline curve is -4.4 ± 1.6.

Figure 5.23 shows a plot of elliptic flow (v_2) of identified pions versus pseudorapidity for peripheral events in STAR. In order to reduce fluctuations, the data are averaged and reflected about mid-rapidity. In this plot the trendline curve is a fourth-order polynomial. The average value for flow is just below 5% for most of the bins around mid-rapidity.

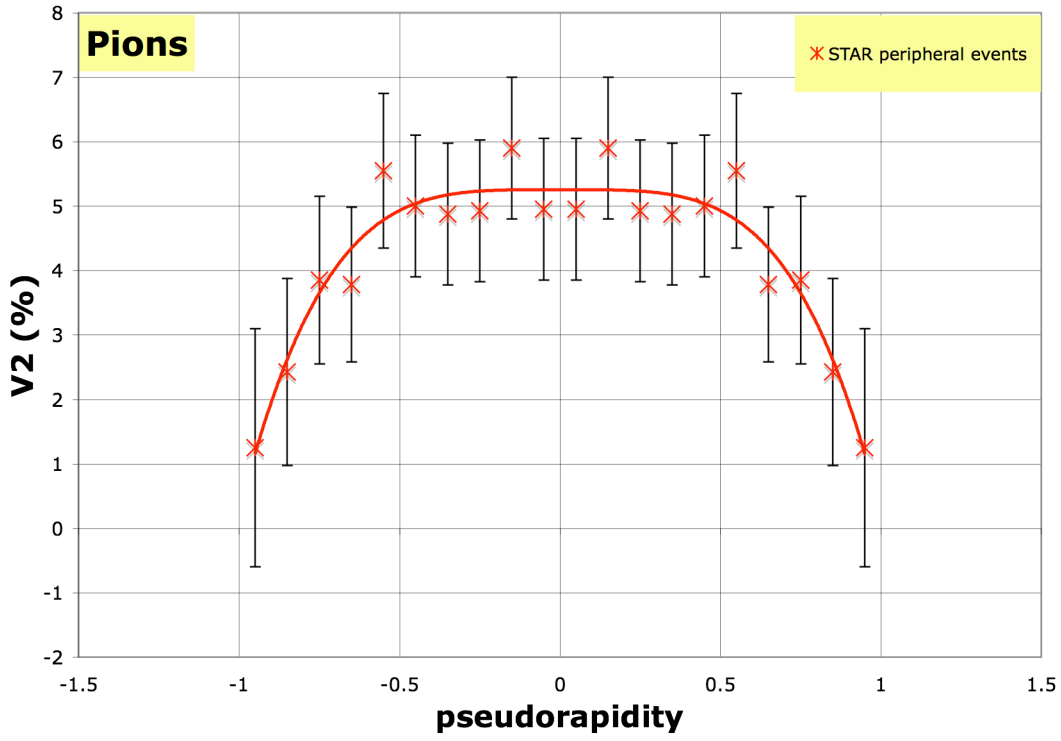

Figure 5.23: A plot of elliptic flow (v_2) of identified pions versus pseudorapidity for peripheral events in STAR.

Figure 5.24 shows a plot of directed flow (v_1) of identified pions versus transverse momentum (p_T) for peripheral events STAR. As the transverse momentum increases, the statistics in the transverse momentum histogram bins decrease rapidly. Positive flow is defined as the direction of proton flow. The pions exhibit a negative flow in the low transverse momentum.

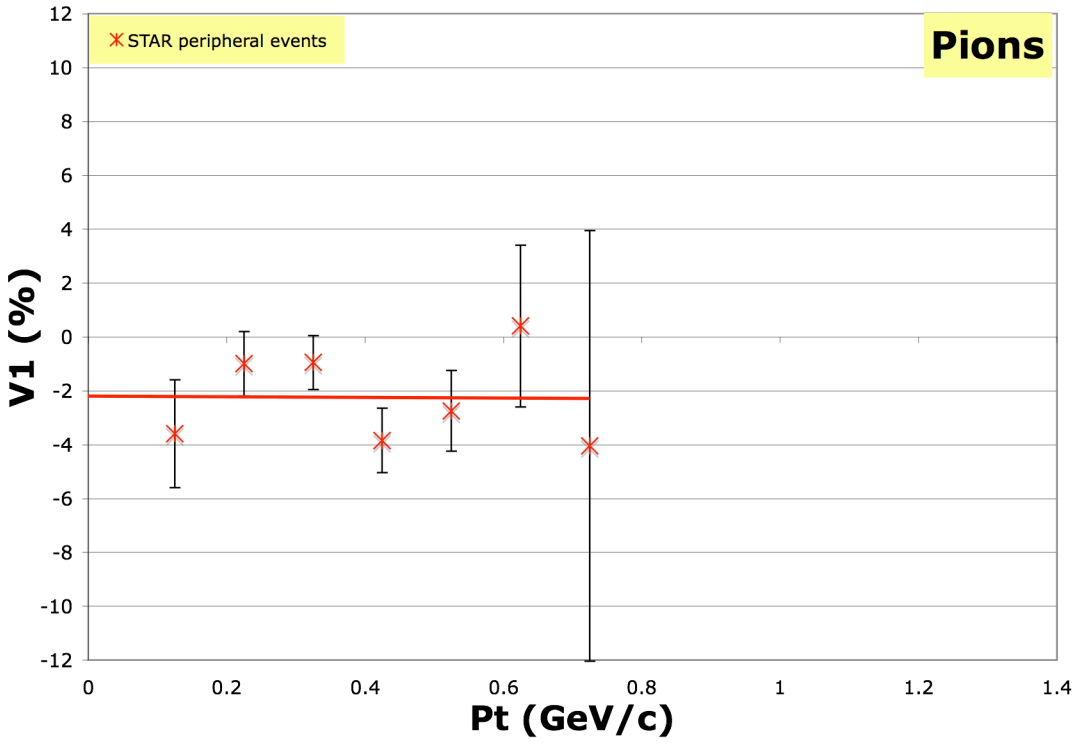

Figure 5.24: A plot of directed flow (v_1) of identified pions versus transverse momentum (p_T) for peripheral events in STAR.

Figure 5.25 shows a plot of elliptic flow (v_2) of identified pions versus transverse momentum (p_T) for peripheral events in STAR. As the transverse momentum increases, the statistics in the transverse momentum histogram bins decrease rapidly. The v_2 values increase with p_T.

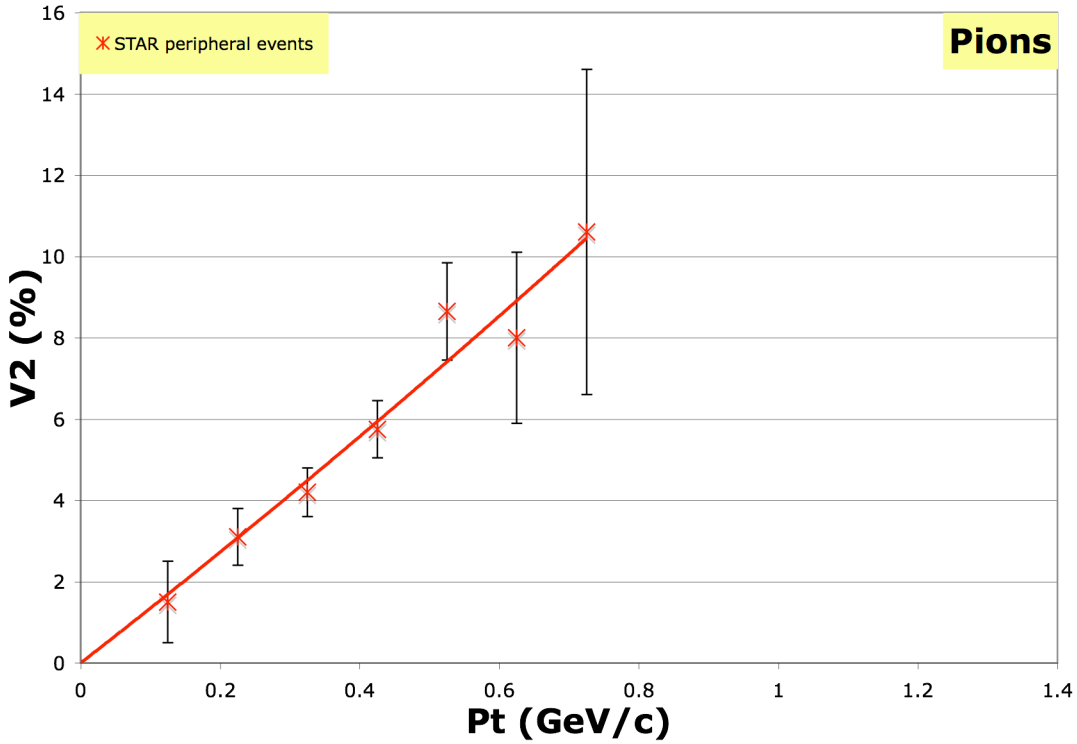

Figure 5.25: A plot of elliptic flow (v_2) of identified pions versus transverse momentum (p_T) for peripheral events in STAR.

5.3.2 Identified Pion Semi-Peripheral Events

This sub-section deals with semi-peripheral events (30% to 50% centrality). This centrality bin contained 7,474 events that passed all of the cuts.

Figure 5.26 shows a plot of directed flow (v_1) of identified pions versus pseudorapidity for semi-peripheral events STAR. In order to reduce fluctuations, the data are averaged, inverted, and reflected about mid-rapidity. The trendline curve is forced through a flow value of zero at $\eta = 0$. The value for directed flow is approximately 3% in the higher pseudorapidity bins. The slope of the trendline curve is -4.0 ± 1.5.

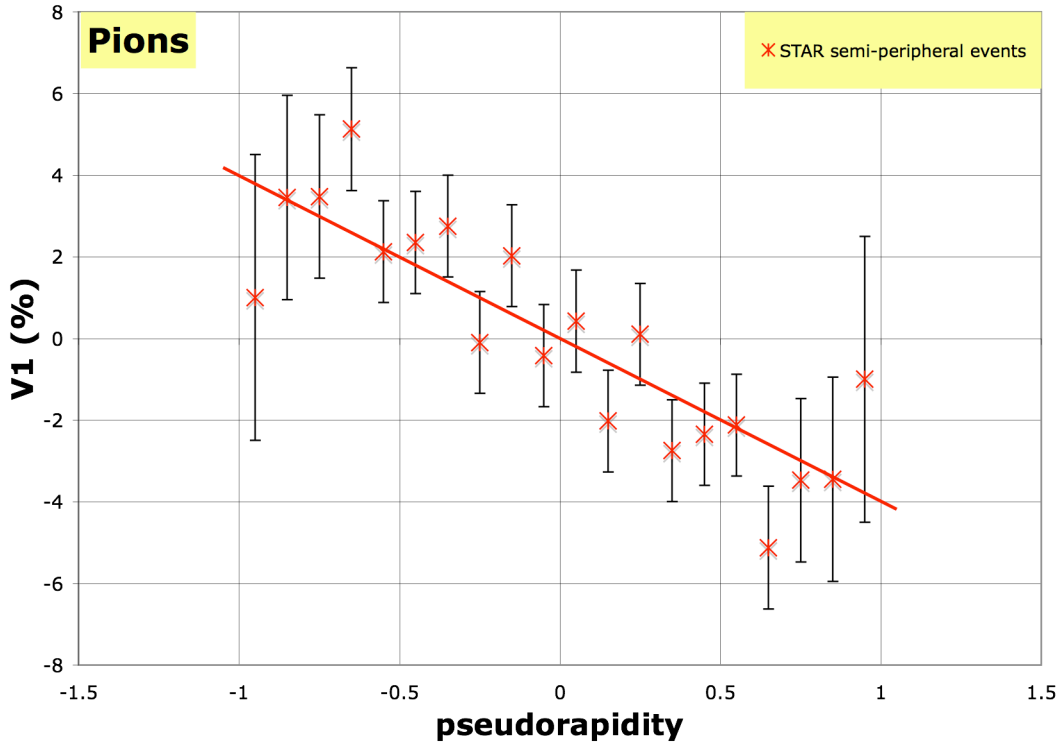

Figure 5.26: A plot of directed flow (v_1) of identified pions versus pseudorapidity for semi-peripheral events in STAR.

Figure 5.27 shows a plot of elliptic flow (v_2) of identified pions versus pseudorapidity for semi-peripheral events in STAR. In order to reduce fluctuations, the data are averaged and reflected about mid-rapidity. In this plot the trendline curve is a fourth-order polynomial. The average value for flow is just below 4% for most of the bins around mid-rapidity. The magnitude of v_2 is maximum at a value of $\eta = 0$.

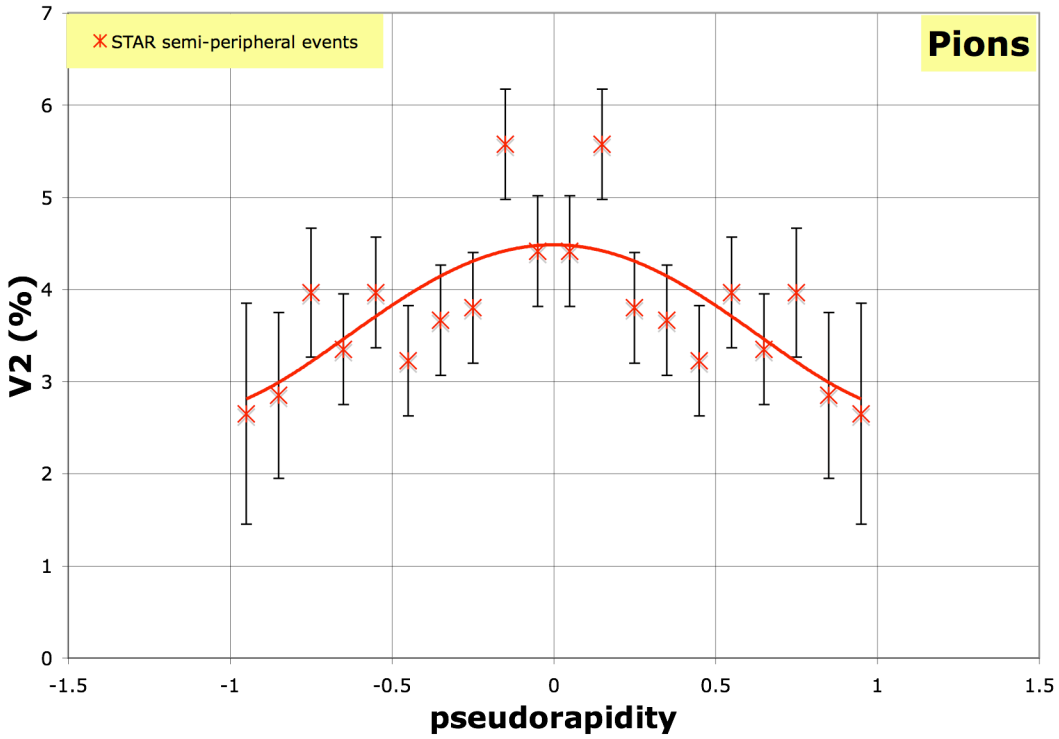

Figure 5.27: A plot of elliptic flow (v_2) of identified pions versus pseudorapidity for semi-peripheral events in STAR.

Figure 5.28 shows a plot of directed flow (v_1) of identified pions versus transverse momentum (p_T) for semi-peripheral events in STAR. As the transverse momentum increases, the statistics in the transverse momentum histogram bins decrease rapidly. Positive flow is defined as the direction of proton flow. The pions exhibit a negative flow in the low transverse momentum region.

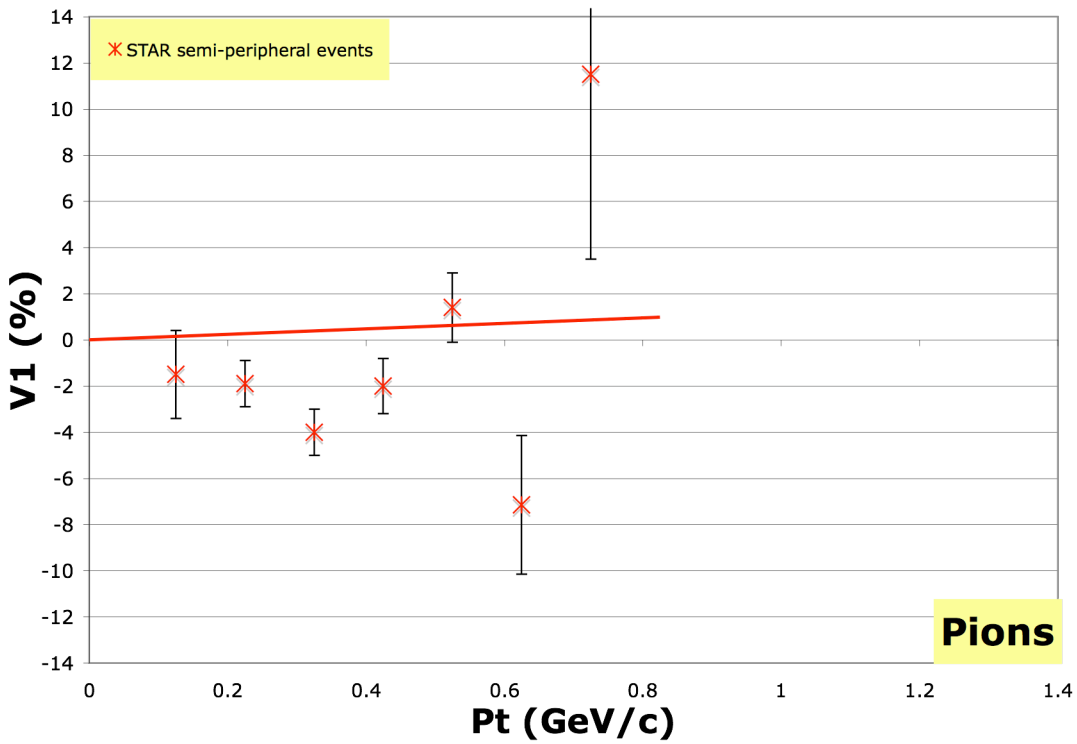

Figure 5.28: A plot of directed flow (v_1) of identified pions versus transverse momentum (p_T) for semi-peripheral events in STAR.

Figure 5.29 shows a plot of elliptic flow (v_2) of identified pions versus transverse momentum (p_T) for semi-peripheral events in STAR. As the transverse momentum increases, the statistics in the transverse momentum histogram bins decrease rapidly. The v_2 values increase with p_T.

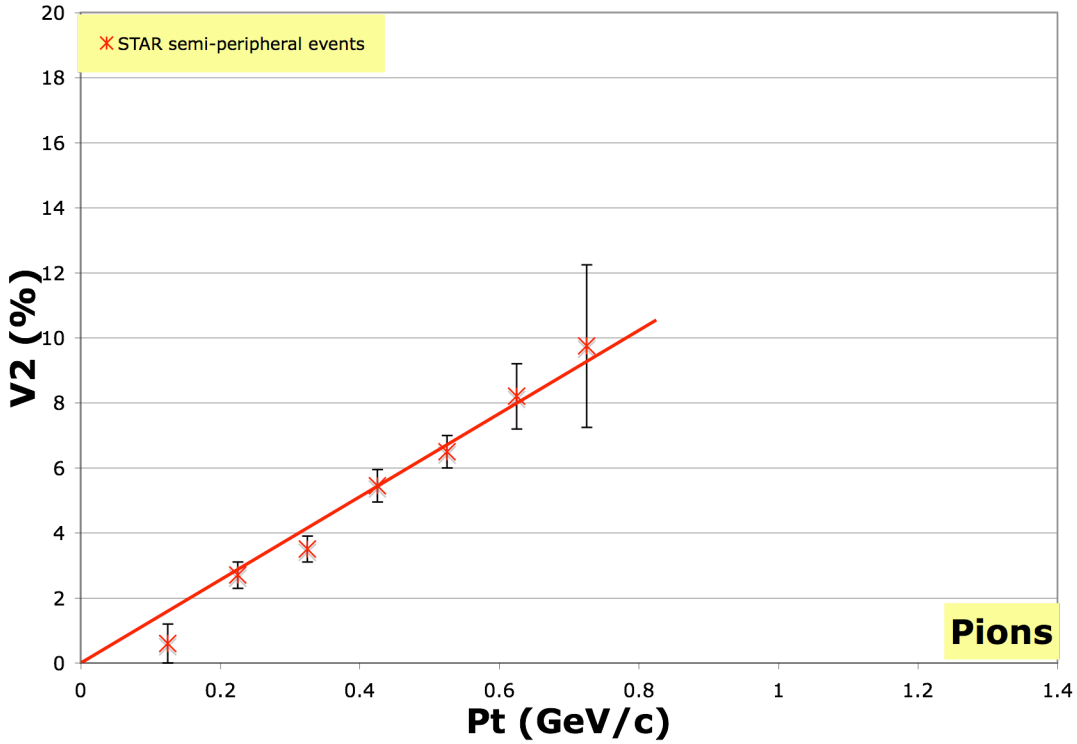

Figure 5.29: A plot of elliptic flow (v_2) of identified pions versus transverse momentum (p_T) for semi-peripheral events in STAR.

5.3.3 Identified Pion Semi-Central Events

This sub-section deals with semi-central events (10% to 30% centrality). This centrality bin contained 5,661 events that passed all of the cuts.

Figure 5.30 shows a plot of directed flow (v_1) of identified pions versus pseudorapidity for semi-central events in STAR. In order to reduce fluctuations, the data are averaged, inverted, and reflected about mid-rapidity. The trendline curve is forced through a flow value of zero at $\eta = 0$. The value for directed flow is around 2% in the higher pseudorapidity bins. The slope of the trendline curve is -3.0 ± 3.5.

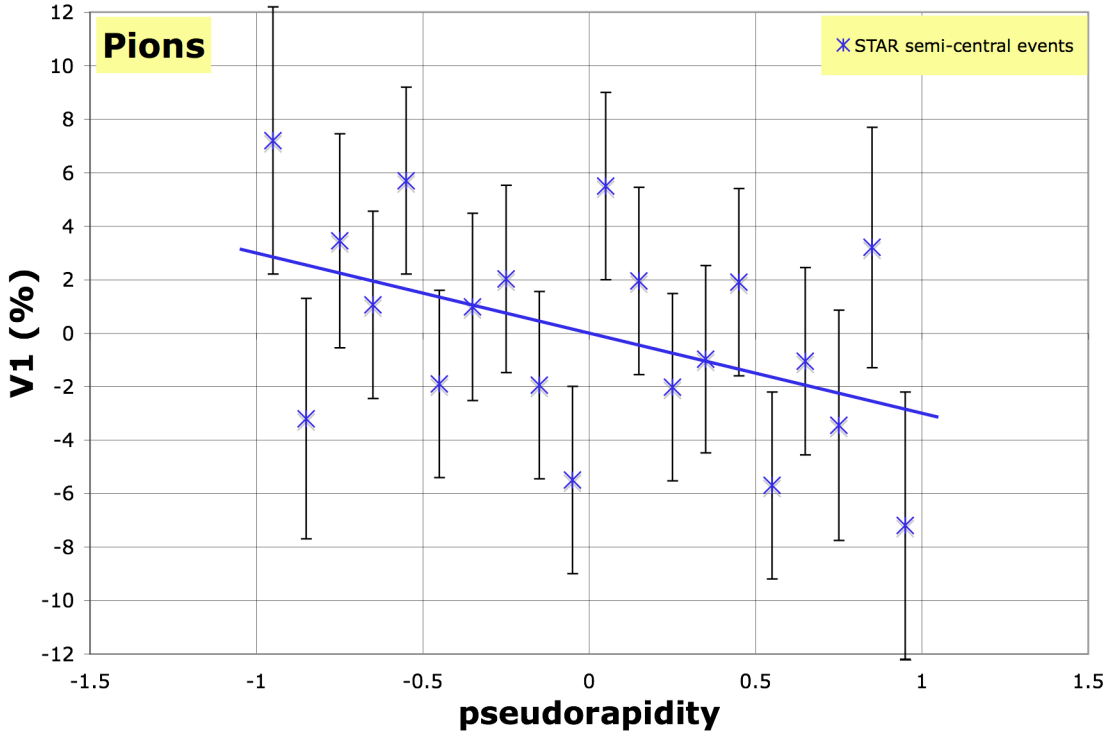

Figure 5.30: A plot of directed flow (v_1) of identified pions versus pseudorapidity for semi-central events in STAR.

Figure 5.31 shows a plot of elliptic flow (v_2) of identified pions versus pseudorapidity for semi-central events STAR. In order to reduce fluctuations, the data are averaged and reflected about mid-rapidity. In this plot the trendline curve is a second-order polynomial. The average value for flow is around 2.5% for most of the bins around mid-rapidity. The magnitude of v_2 is maximum near $\eta = 0$.

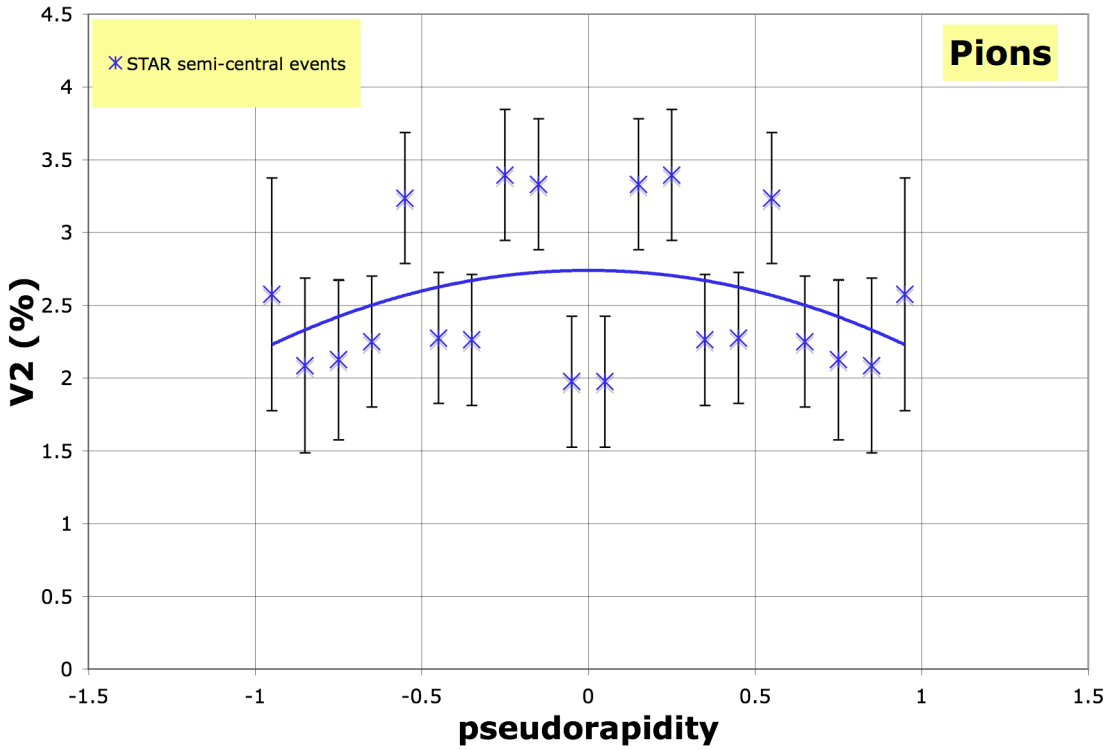

Figure 5.31: A plot of elliptic flow (v_2) of identified pions versus pseudorapidity for semi-central events in STAR.

Figure 5.32 shows a plot of directed flow (v_1) of identified pions versus transverse momentum (p_T) for semi-central events in STAR. As the transverse momentum increases, the statistics in the transverse momentum histogram bins decrease rapidly. Positive flow is defined as the direction of proton flow. The pions exhibit a negative flow in the low transverse momentum region.

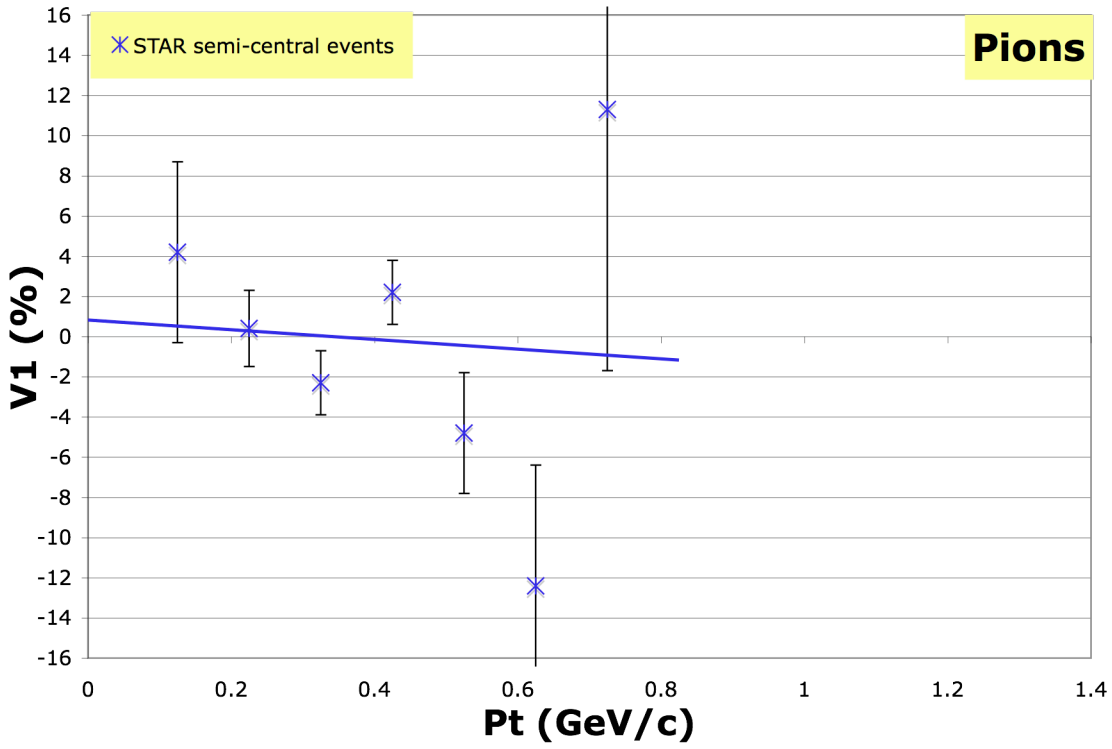

Figure 5.32: A plot of directed flow (v_1) of identified pions versus transverse momentum (p_T) for semi-central events in STAR.

Figure 5.33 shows a plot of elliptic flow (v_2) of identified pions versus transverse momentum (p_T) for semi-central events in STAR. As the transverse momentum increases, the statistics in the transverse momentum histogram bins decrease rapidly. The v_2 values increase with p_T.

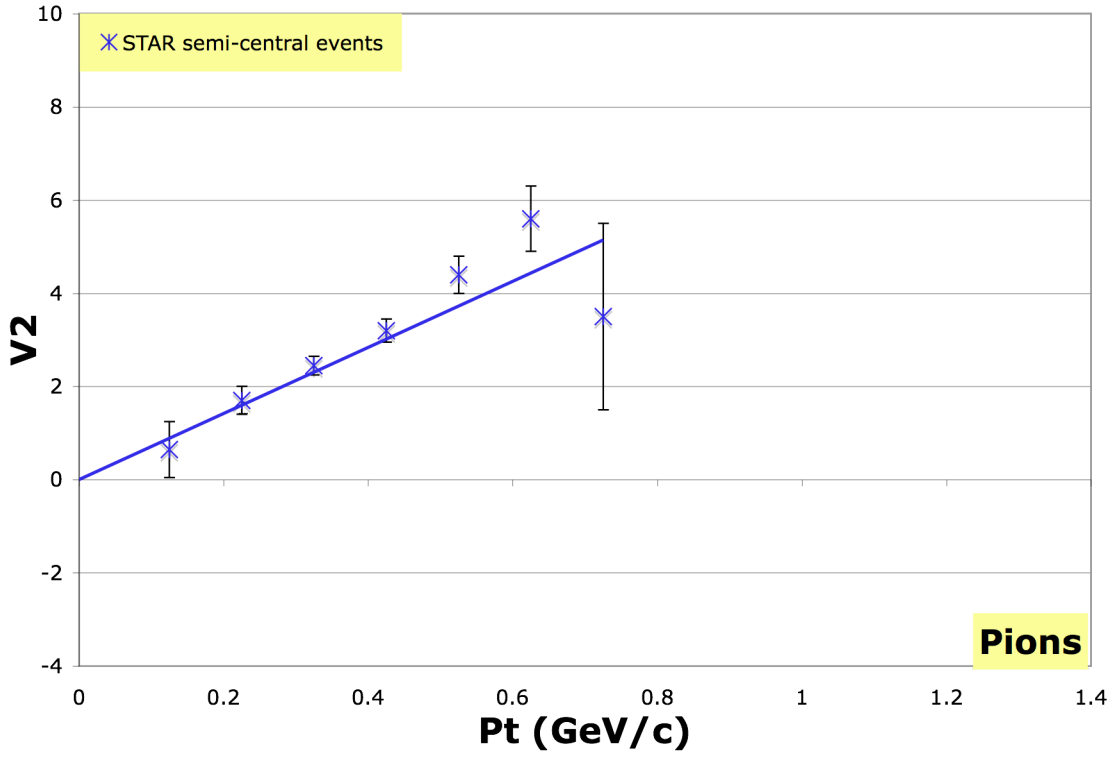

Figure 5.33: A plot of elliptic flow (v_2) of identified pions versus transverse momentum (p_T) for semi-central events in STAR.

5.3.4 Identified Pion Central Events

This sub-section deals with central events (top 10% centrality). This centrality bin contained 3,592 events that passed all of the cuts.

Figure 5.34 shows a plot of directed flow (v_1) of identified pions versus pseudorapidity for central events in STAR. In order to reduce fluctuations, the data are averaged, inverted, and reflected about mid-rapidity. The trendline curve is forced through a flow value of zero at $\eta = 0$ (note that the trendline here is fit to the data points and is not a line defined to have a zero slope). The data are consistent with no directed flow throughout the pseudorapidity region. The slope of the trendline curve is 0.030 ± 1.5.

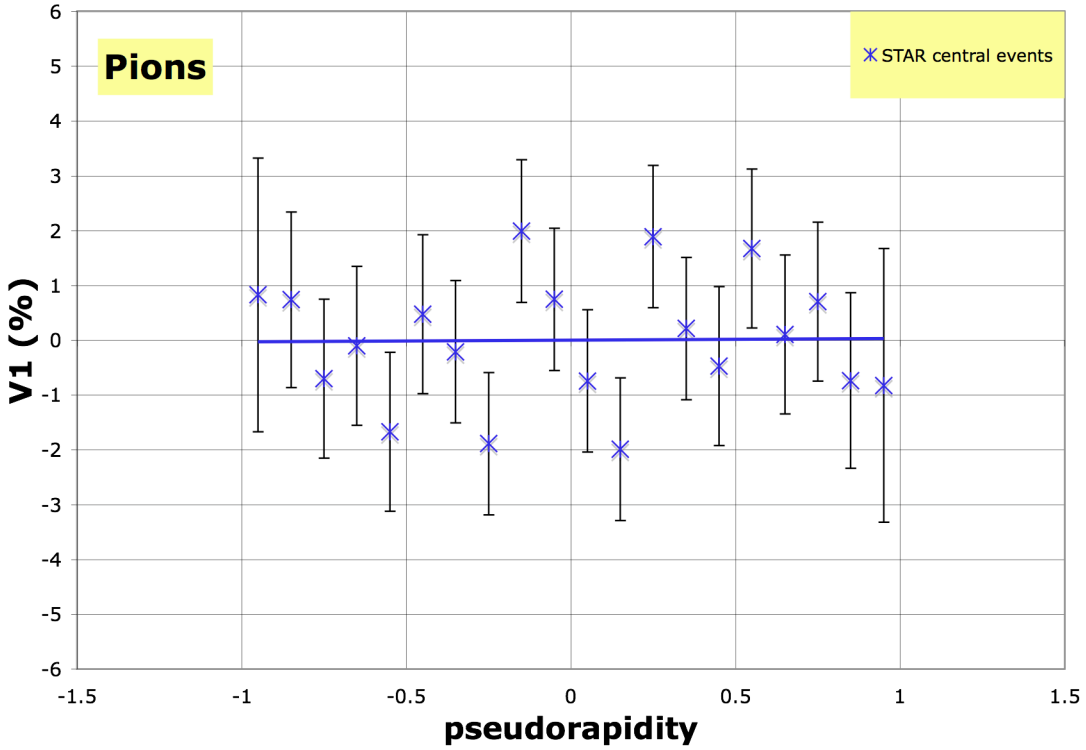

Figure 5.34: A plot of directed flow (v_1) of identified pions versus pseudorapidity for central events in STAR.

Figure 5.35 shows a plot of elliptic flow (v_2) of identified pions versus pseudorapidity for central events in STAR. In order to reduce fluctuations, the data are averaged and reflected about mid-rapidity. In this plot the trendline curve is a fourth-order polynomial. The average value for flow is just below 2% for most of the bins around mid-rapidity.

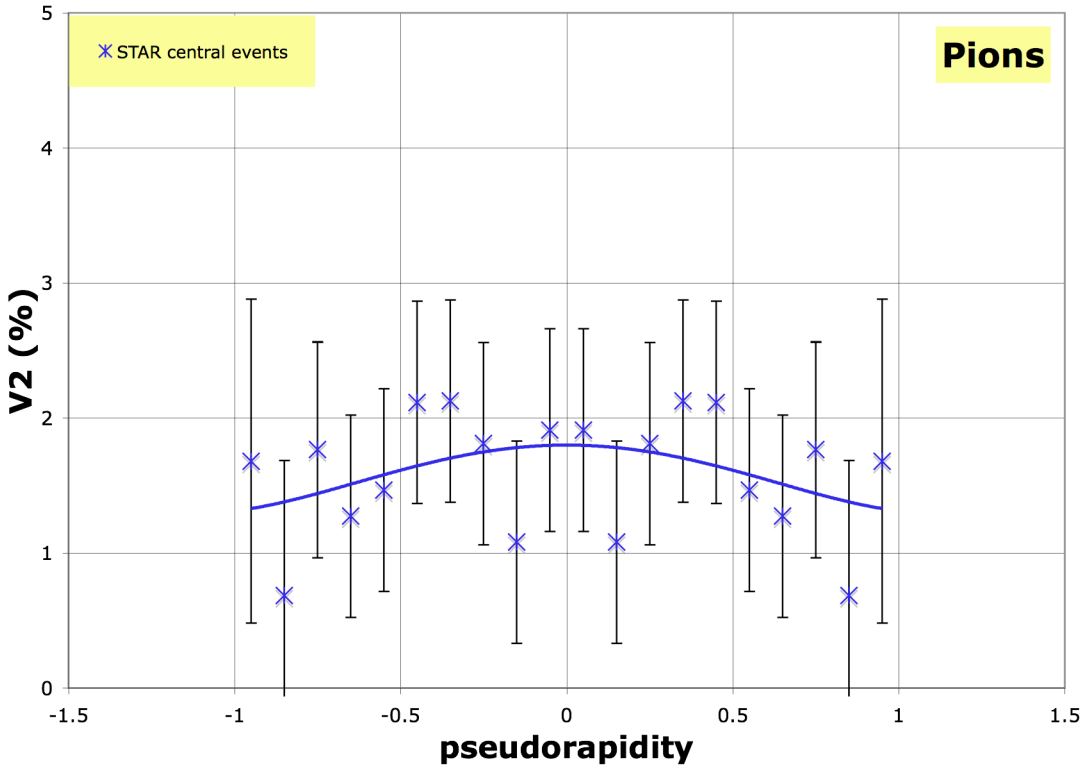

Figure 5.35: A plot of elliptic flow (v_2) of identified pions versus pseudorapidity for central events in STAR.

Figure 5.36 shows a plot of directed flow (v_1) of identified pions versus transverse momentum (p_T) for central events in STAR. As the transverse momentum increases, the statistics in the transverse momentum histogram bins decrease rapidly. Positive flow is defined as the direction of proton flow. The pions exhibit no flow in the low transverse momentum region. In the highest two transverse momentum bins, the flow value then unexpectedly turned negative; this may be due to those bins having very low statistics.

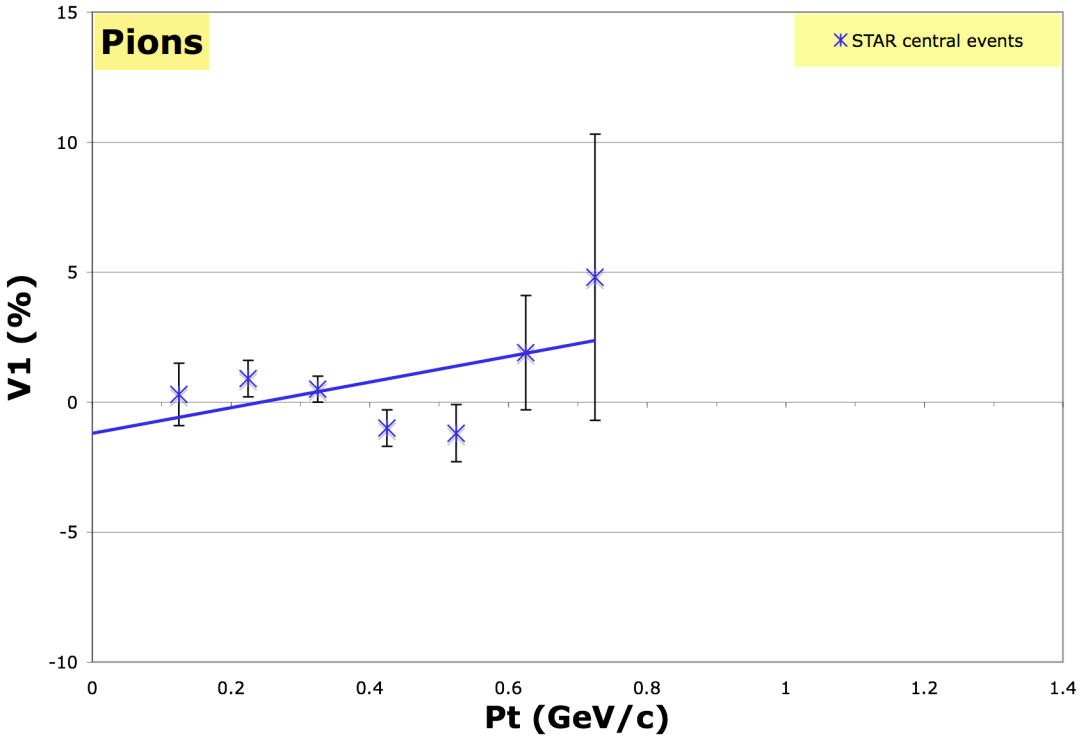

Figure 5.36: A plot of directed flow (v_1) of identified pions versus transverse momentum (p_T) for central events in STAR.

Figure 5.37 shows a plot of elliptic flow (v_2) of identified pions versus transverse momentum (p_T) for central events in STAR. As the transverse momentum increases, the statistics in the transverse momentum histogram bins decrease rapidly. The v_2 values increase with p_T.

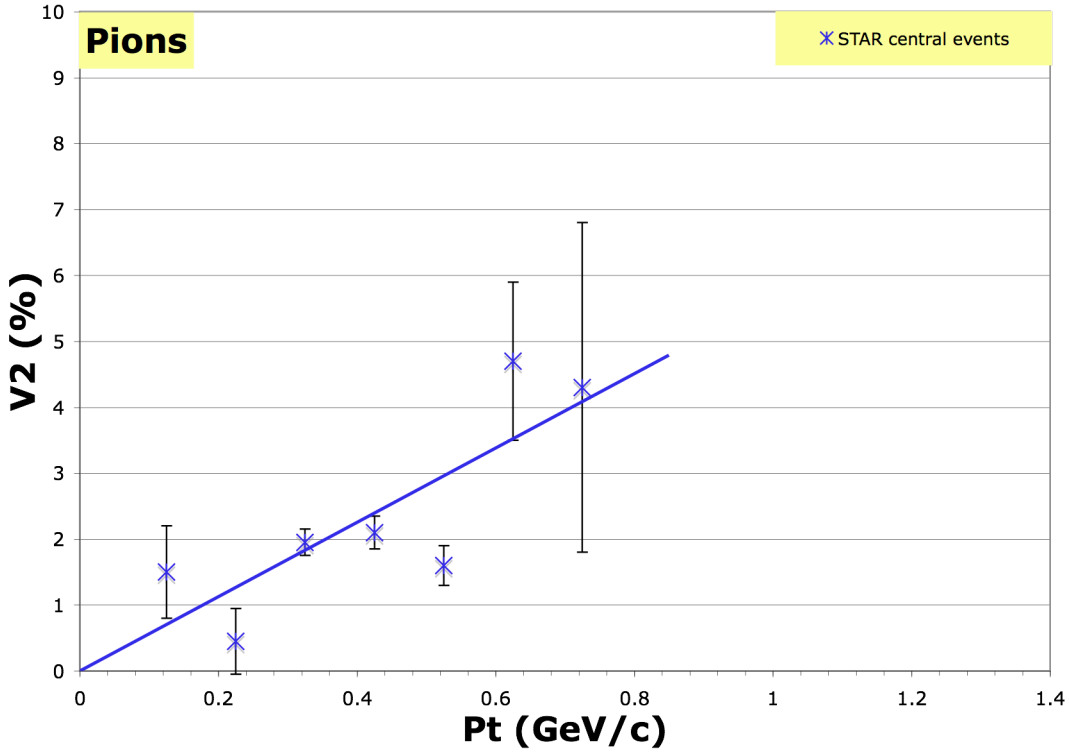

Figure 5.37: A plot of elliptic flow (v_2) of identified pions versus transverse momentum (p_T) for central events in STAR.

5.3.5 Identified Pion Events with All Centralities

This sub-section deals with events containing all centralities (*i.e.* minimum bias events). Minimum bias events contained 30,983 events that passed all of the cuts. When scrutinizing this sub-section, please refer back to the cautionary note in section 5.2.5 regarding "minimum bias" events.

Figure 5.38 shows a plot of directed flow (v_1) of identified pions versus pseudorapidity for minimum bias events in STAR. Note that the systematic errors dominate the error bars here. In order to reduce fluctuations, the data are averaged, inverted, and reflected about mid-rapidity. The trendline curve is forced through a flow value of zero at $\eta = 0$. The value for directed flow is about 1.5% in the higher pseudorapidity bins. The slope of the trendline curve is -1.6 ± 1.0.

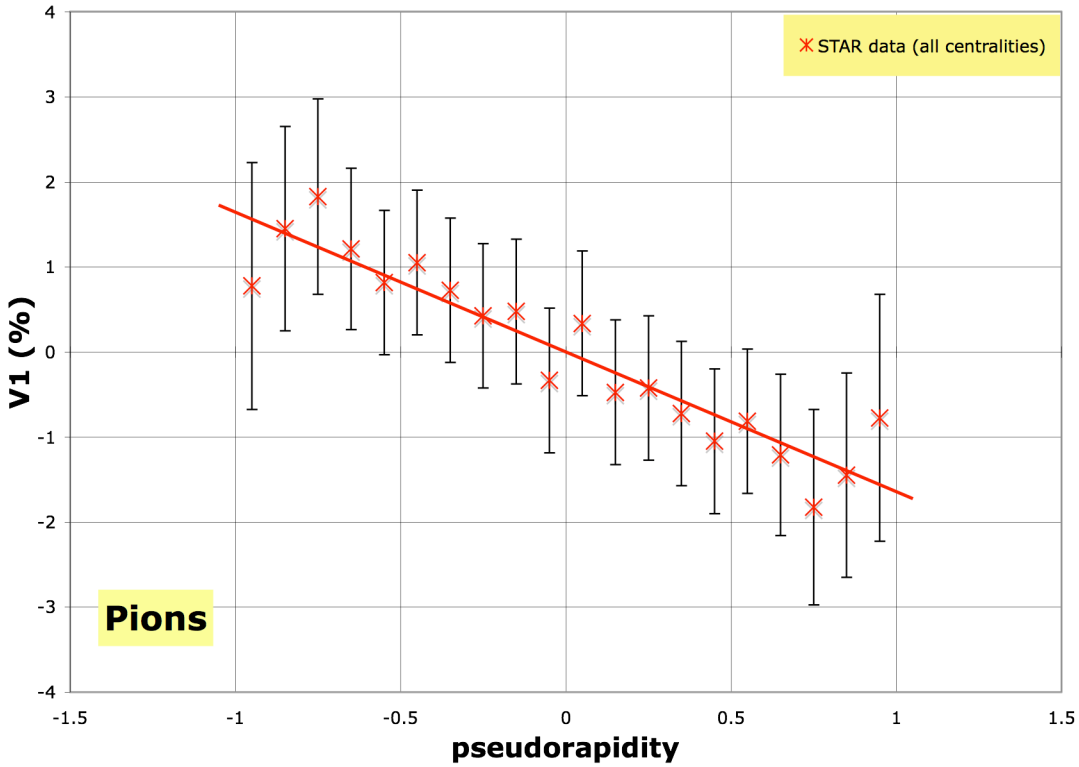

Figure 5.38: A plot of directed flow (v_1) of identified pions versus pseudorapidity for minimum bias events in STAR. Note that the systematic errors dominate here.

Figure 5.39 shows a plot of elliptic flow (v_2) of identified pions versus pseudorapidity for minimum bias events in STAR. In order to reduce fluctuations, the data are averaged and reflected about mid-rapidity. In this plot the trendline curve is a fourth-order polynomial. The average value for flow is about 3.5% for most of the bins around mid-rapidity. The magnitude of v_2 is maximum near $\eta = 0$.

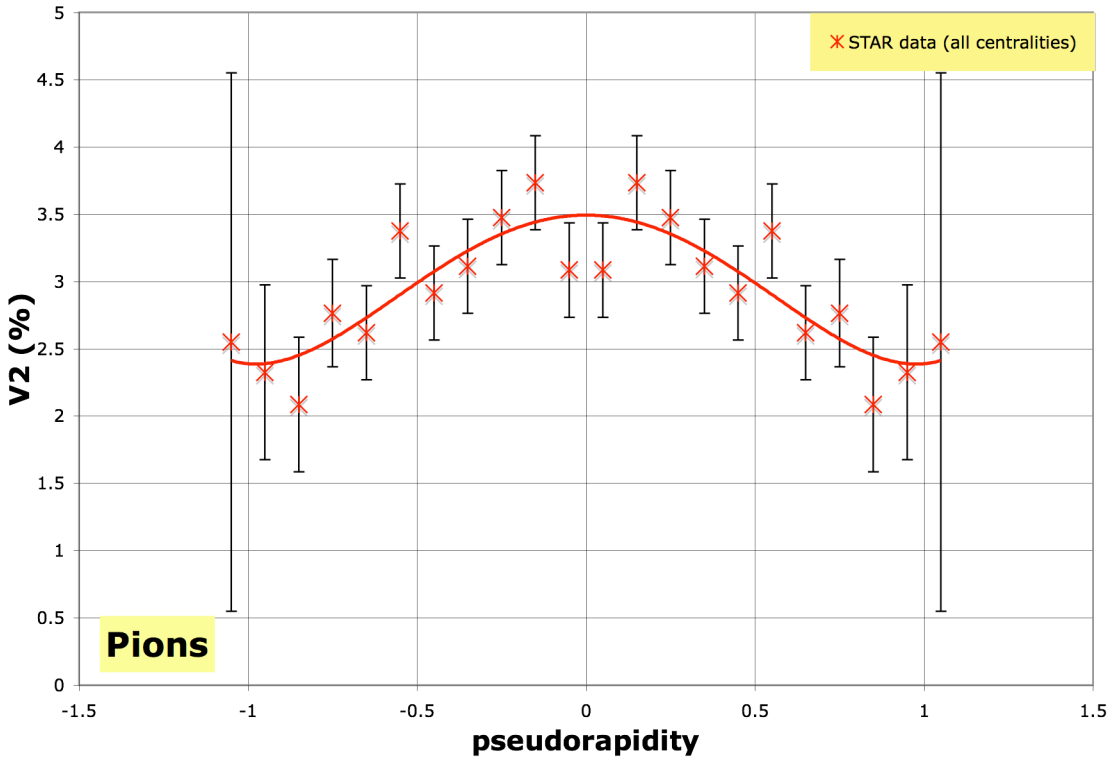

Figure 5.39: A plot of elliptic flow (v_2) of identified pions versus pseudorapidity for minimum bias events in STAR.

Figure 5.40 shows a plot of directed flow (v_1) of identified pions versus transverse momentum (p_T) for minimum bias events in STAR. As the transverse momentum increases, the statistics in the transverse momentum histogram bins decrease rapidly. Positive flow is defined as the direction of proton flow. The pions exhibit a negative flow in the low transverse momentum region. In the highest transverse momentum bin, the flow value then unexpectedly turned negative; this may be due to those bins having very low statistics.

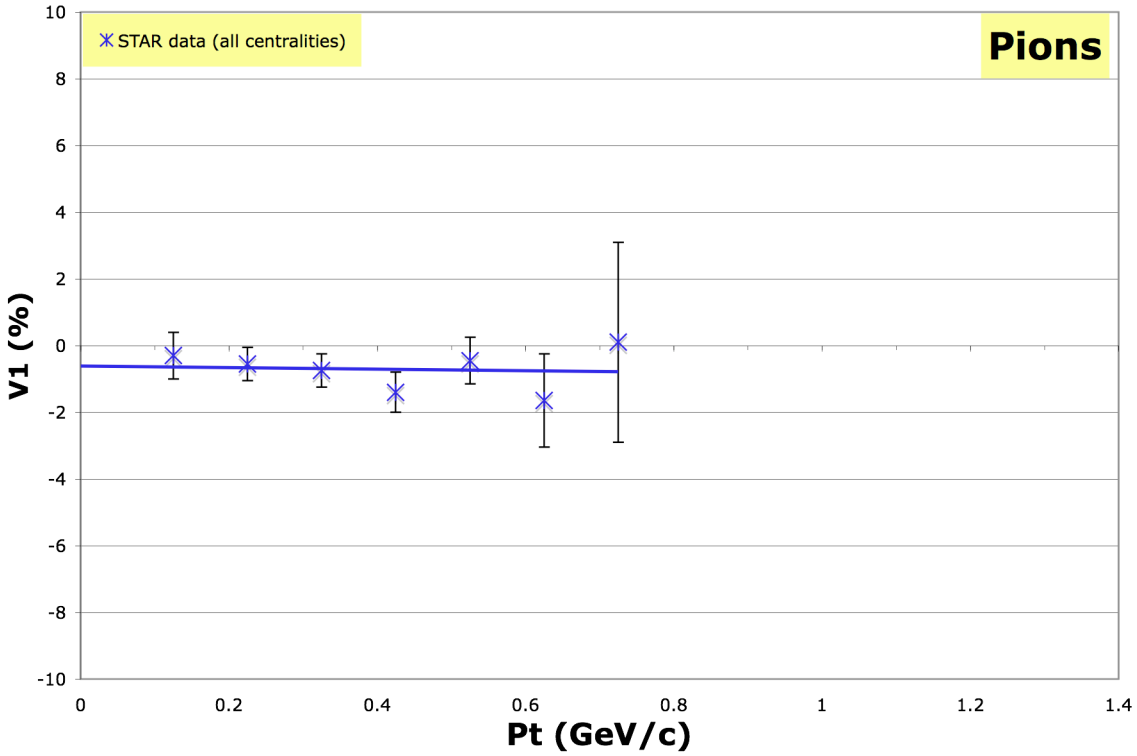

Figure 5.40: A plot of directed flow (v_1) of identified pions versus transverse momentum (p_T) for minimum bias events in STAR.

Figure 5.41 shows a plot of elliptic flow (v_2) of identified pions versus transverse momentum (p_T) for minimum bias events in STAR. As the transverse momentum increases, the statistics in the transverse momentum histogram bins decrease rapidly. The v_2 values increase with p_T.

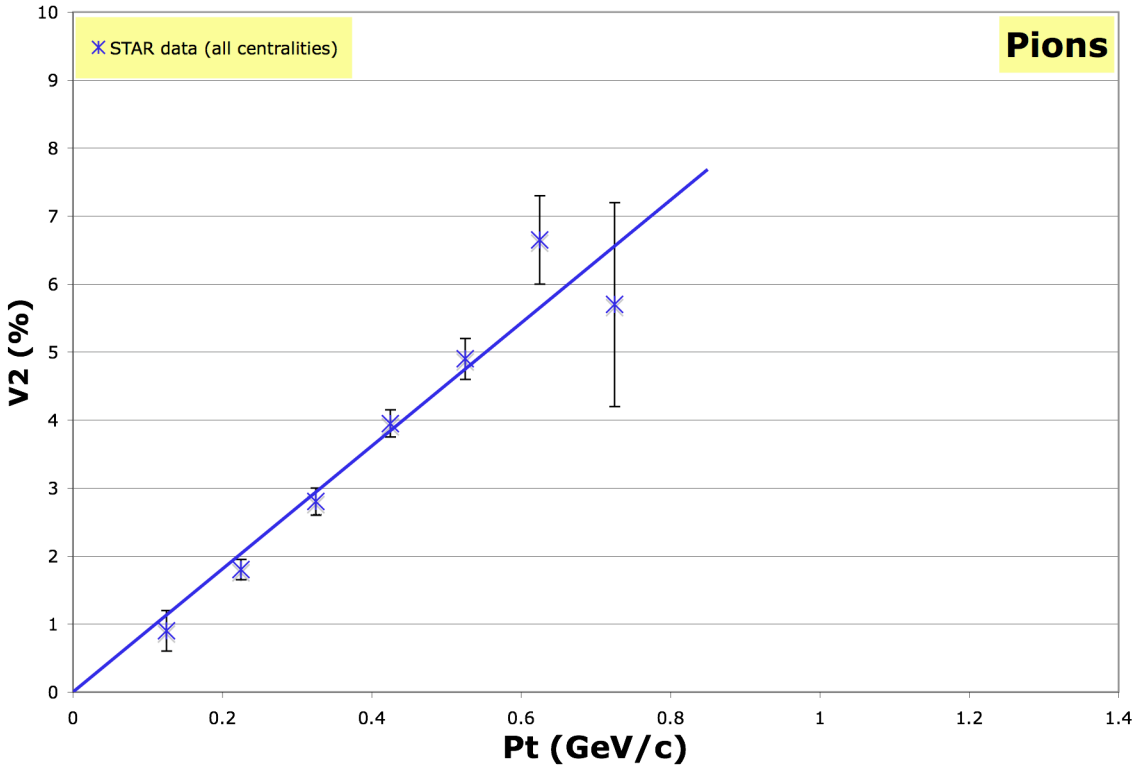

Figure 5.41: A plot of elliptic flow (v_2) of identified pions versus transverse momentum (p_T) for minimum bias events in STAR.

5.4 Conclusions of Results

This section summarizes the conclusions of this chapter. Table 5.1 on the following page reviews the numerical results of the all particle section of this chapter (section 5.2).

In this table a directed flow value (v_1) is given at a pseudorapidity (η) of 1 for various centralities. The table also includes the slope of the directed flow value versus pseudorapidity for various centralities. Also in this table, a directed flow value is given at a transverse momentum (p_T) of 0.5 GeV/c for various centralities. Also in this table, an elliptic flow value (v_2) is given at a pseudorapidity of 1 for various centralities. The table also includes the average elliptic flow value ($\langle v_2 \rangle$) between the values of $|\eta| \leq 1$ for various centralities. Finally, this table also includes an elliptic flow value at a transverse

momentum of 0.5 GeV/c for various centralities. The values in the tables were determined from the plots in this chapter by examining the trendline values.

All Particles	v_1 @ $\|\eta\| = 1$	v_1 vs η slope	v_2 @ $\eta = 0$	$\langle v_2 \rangle$ $\|\eta\| \leq 1$	v_1 @ $p_T = 0.5$ GeV/c	v_2 @ $p_T = 0.5$ GeV/c
Central Events	0.23%	–0.21 $\pm$1.0	1.9%	2.0% $\pm$0.5%	0.70%	1.9%
Semi-Central Events	5.0%	–5.0 $\pm$2.7	3.7%	3.7% $\pm$0.4%	–2.8%	3.9%
Semi-Peripheral Events	3.4%	–3.5 $\pm$1.4	5.5%	5.3% $\pm$0.4%	–1.5%	5.8%
Peripheral Events	4.6%	–4.5 $\pm$1.4	6.6%	5.8% $\pm$0.9%	–3.4%	6.1%
Minimum Bias Events	2.4%	–2.4 $\pm$0.7	4.2%	4.1% $\pm$0.3%	–1.2%	4.5%

Table 5.1: Numerical results of the all particle section of this chapter (section 5.2)

From the table and the plots in section 5.2, we observe the following for directed flow, v_1. The magnitude of directed flow increases with pseudorapidity. Also, when measured versus transverse momentum, p_T, directed flow is relatively flat. Directed flow decreases as the collisions become more central due to simple symmetry. There is an asymmetry of directed flow about zero pseudorapidity driven by the symmetry of Au+Au collisions.

We also observe the following for elliptic flow, v_2. The magnitude of elliptic flow is maximum when pseudorapidity is zero. Also, when measured against transverse momentum, elliptic flow increases with transverse momentum up to about 2 GeV/c. Elliptic flow decreases as the collisions become more central due to a less spherical deformed source with a more uniform pressure gradient. There is a symmetry of elliptic flow about zero pseudorapidity driven by the symmetry of Au+Au collisions.

A table was created for the pions with the same criteria as the all particle table. Table 5.2 is a table that reviews the numerical results of the pion section of this chapter (section 5.3).

Pions	v_1 @ $\eta = 1$	v_1 vs η slope	v_2 @ $\eta = 0$	$\langle v_2 \rangle$ $\lvert\eta\rvert \leq 1$	v_1 @ $p_T = 0.5$ GeV/c	v_2 @ $p_T = 0.5$ GeV/c
Central Events	0%	0.030 $\pm$1.5	1.8%	1.6% $\pm$0.8%	1.3%	2.7%
Semi-Central Events	3.0%	–3.0 $\pm$3.5	2.7%	2.6% $\pm$0.5%	–0.2%	3.5%
Semi-Peripheral Events	4.0%	–4.0 $\pm$1.5	4.5%	3.7% $\pm$0.7%	0.6%	6.2%
Peripheral Events	4.4%	–4.4 $\pm$1.6	5.3%	4.3% $\pm$1.3%	–2.1%	7.1%
Minimum Bias Events	1.7%	–1.6 $\pm$1.0	3.5%	2.9% $\pm$0.4%	–0.70%	4.7%

Table 5.2: Numerical results of the pion section of this chapter (section 5.3)

From the table and the plots in section 5.3, we observe that the results do not change significantly when selecting only on pions. The basic shapes and results are comparable. This is largely because pions dominate the yields. The ratio of yields of positively charged pions to protons is about 9.0 to one. The ratio of yields of all charged pions to protons plus anti-protons is about 17 to one. The ratio of yields of positively charged kaons to protons is about 0.20 to one. Also, the ratio of yields of all charged kaons to protons plus anti-protons is about 0.35 to one.

Chapter 6

Comparisons

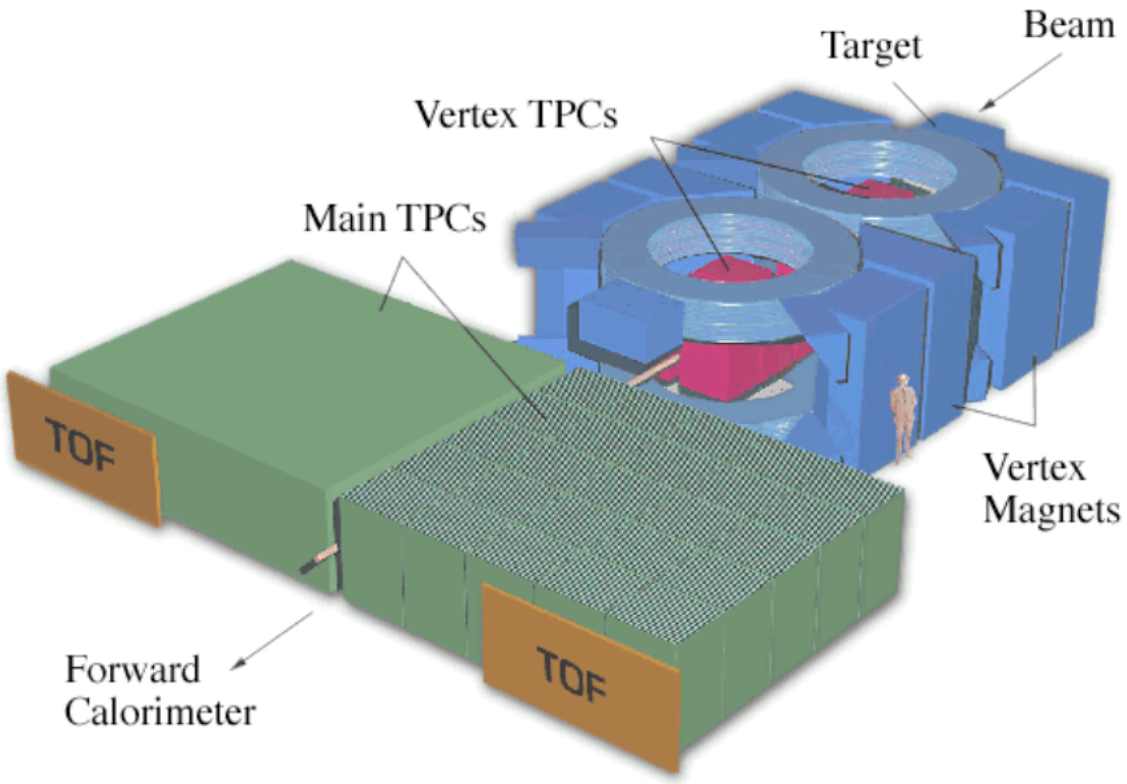

Figure 6.1: The NA49 experiment [NA49 2006].

6.1 Comparisons to NA49

To test the validity of this analysis it is necessary to compare the results to published results. The STAR data presented in this section were analyzed in a manner to compare most directly with the NA49 results. NA49 was an experiment at the SPS, which ran at a center of mass energy of 17.2 GeV per nucleon for Pb on Pb collisions. This is similar to the 19.6 GeV STAR data set which is presented in this thesis. Figure 6.1 shows the NA49 experiment. The NA49 experiment was briefly described in section 1.5.1. All of the NA49 data in this section were extracted from the following reference, [Alt 2003]. The NA49 trendlines on the plots were chosen to match the trendlines in the reference as well as possible.

In order to compare to the NA49 pion flow results, the particles selected were pions. These pions must also have had a transverse momentum between 0.1 GeV/c and 2.0 GeV/c. The events were separated into three separate centrality bins: peripheral events which represent 33.5% to 100% centrality, semi-central events which represent 12.5% to 33.5% centrality, and central events which represent the top 12.5% central events.

6.1.1 Peripheral Events

This sub-section deals with peripheral events (33.5% to 100% centrality). The STAR peripheral bin contained 19,899 events that passed all of the cuts. NA49 used over 100,000 events in their peripheral bin.

Figure 6.2 on the following page shows a plot of directed flow (v_1) of identified pions versus pseudorapidity for both NA49 and STAR. Note that the systematic errors dominate the STAR error bars here. Because the NA49 experiment had acceptance only forward of mid-rapidity, the NA49 data were reflected about mid-rapidity. In order to reduce fluctuations, the STAR data were averaged and reflected about mid-rapidity. For the most part, the results agree with each other within error bars.

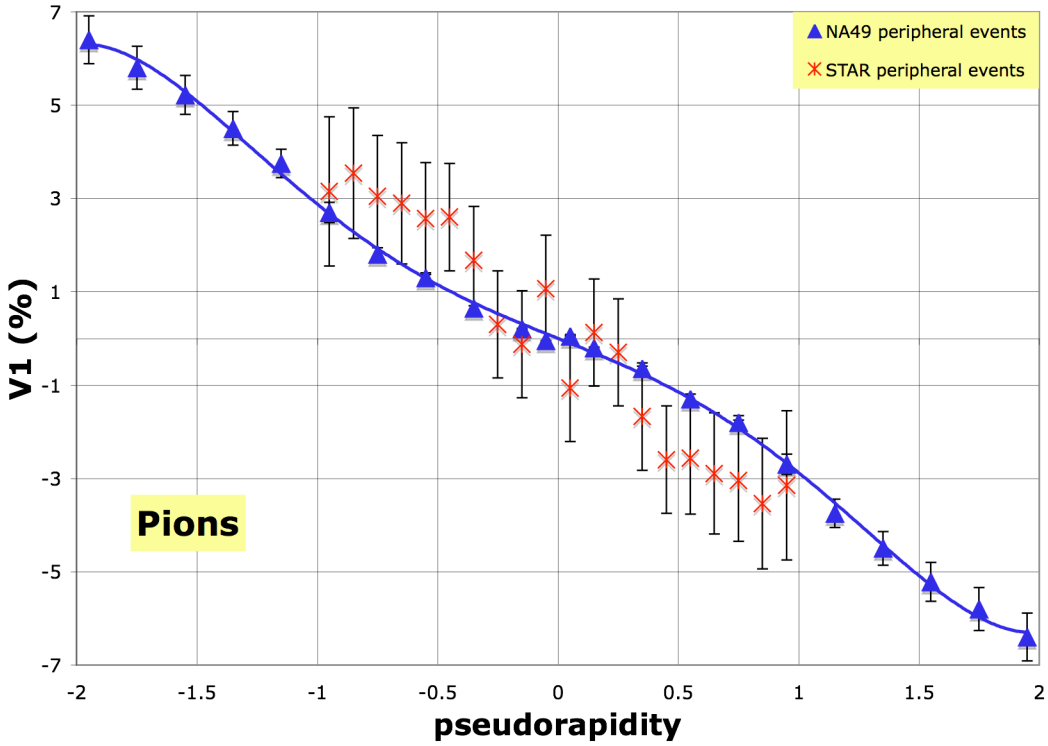

Figure 6.2: A plot of directed flow (v_1) of identified pions versus pseudorapidity for peripheral events in NA49 and STAR. Note that the systematic errors dominate here.

Figure 6.3 shows a plot of elliptic flow (v_2) of identified pions versus pseudorapidity for both NA49 and STAR. Because the NA49 experiment had acceptance only forward of mid-rapidity, the NA49 data were reflected about mid-rapidity. In order to reduce fluctuations, the STAR data were averaged and reflected about mid-rapidity.

The rather large error bars in the STAR data were due to lack of statistics. The STAR result agrees with the NA49 result in average magnitude but not well in shape.

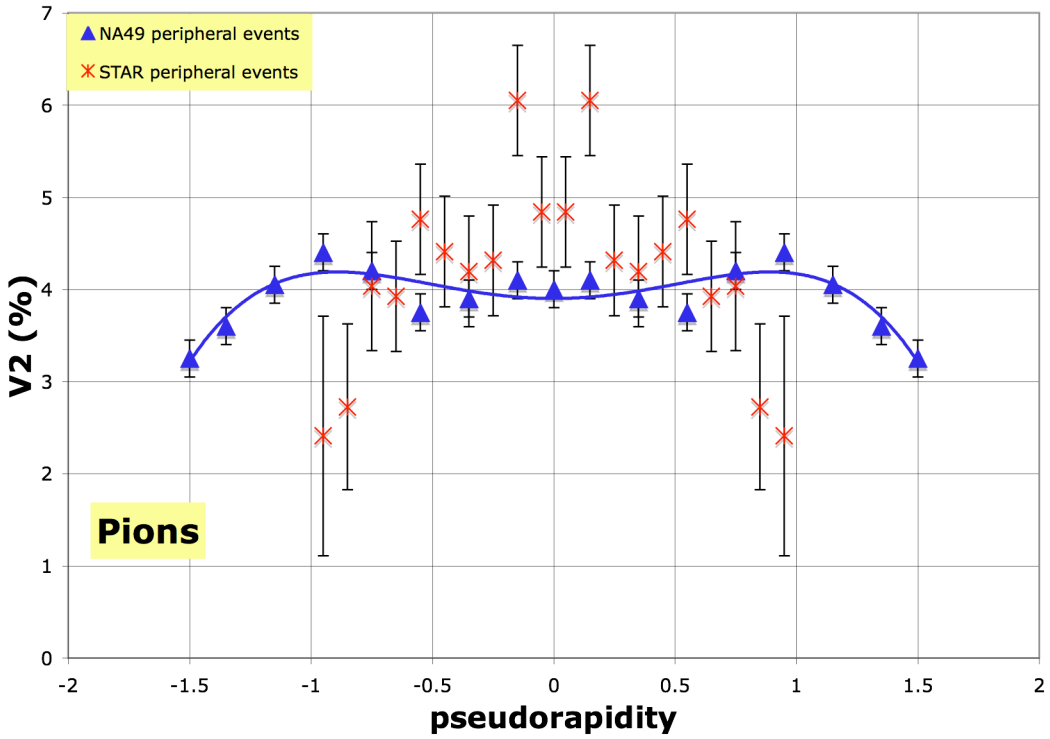

Figure 6.3: A plot of elliptic flow (v_2) of identified pions versus pseudorapidity for peripheral events in NA49 and STAR.

Figure 6.4 shows a plot of directed flow (v_1) of identified pions versus transverse momentum (p_T) for both NA49 and STAR. The rather large error bars in the STAR dataset were due to lack of statistics. As the transverse momentum increased, the statistics in the transverse momentum histogram bins decreased rapidly. The STAR results agreed with the NA49 results within statistics.

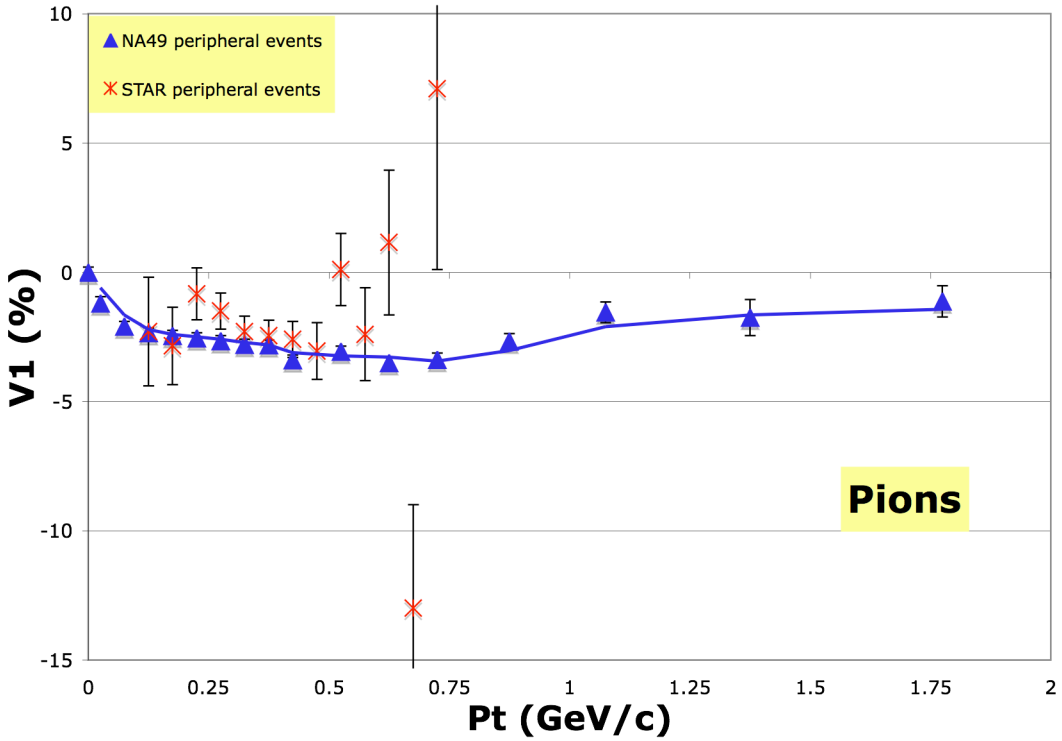

Figure 6.4: A plot of directed flow (v_1) of identified pions versus transverse momentum (p_T) for peripheral events in NA49 and STAR.

Figure 6.5 shows a plot of elliptic flow (v_2) of identified pions versus transverse momentum (p_T) for both NA49 and STAR. The rather large error bars in the STAR dataset were due to lack of statistics. As the transverse momentum increased, the statistics in the transverse momentum histogram bins decreased rapidly. The STAR results agreed with the NA49 results within statistics.

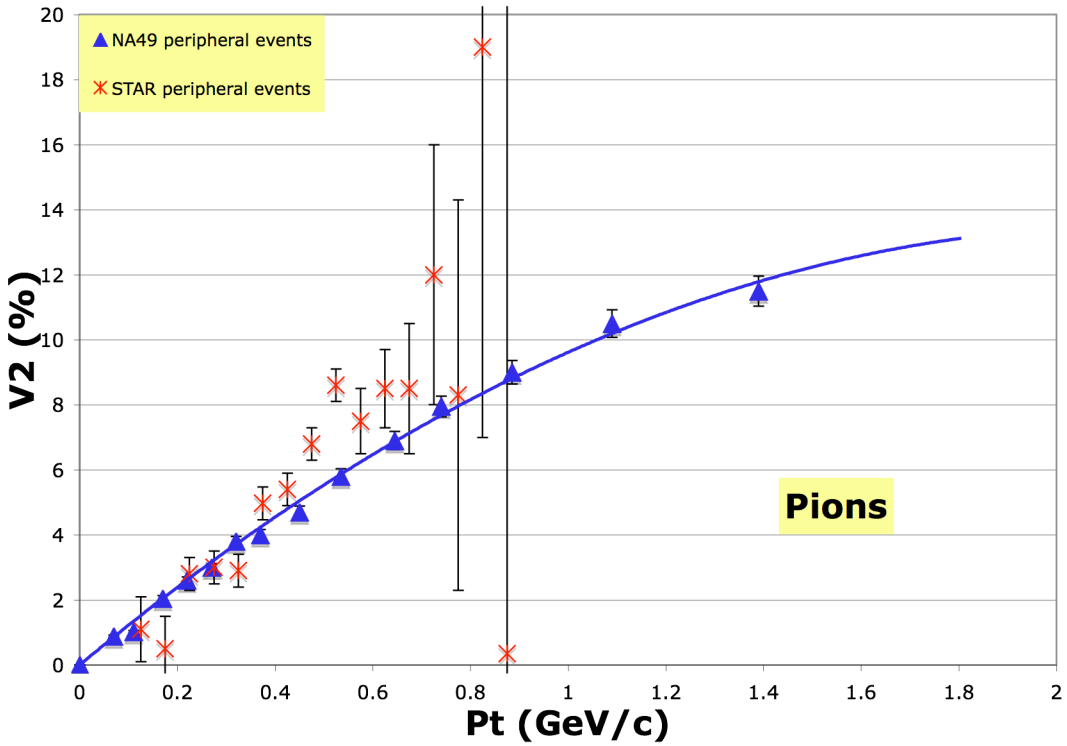

Figure 6.5: A plot of elliptic flow (v_2) of identified pions versus transverse momentum (p_T) for peripheral events in NA49 and STAR.

6.1.2 Semi-Central Events

This sub-section deals with semi-central events (12.5% to 33.5% centrality). The STAR semi-central bin contained 6,165 events that passed all of the cuts. NA49 used over 100,000 events in their semi-central bin.

Figure 6.6 shows a plot of directed flow (v_1) of identified pions versus pseudorapidity for both NA49 and STAR. Because the NA49 experiment had acceptance only forward of mid-rapidity, the NA49 data were reflected about mid-rapidity. In order to reduce fluctuations, the STAR data were averaged and reflected about mid-rapidity. The results agree with each other within statistics.

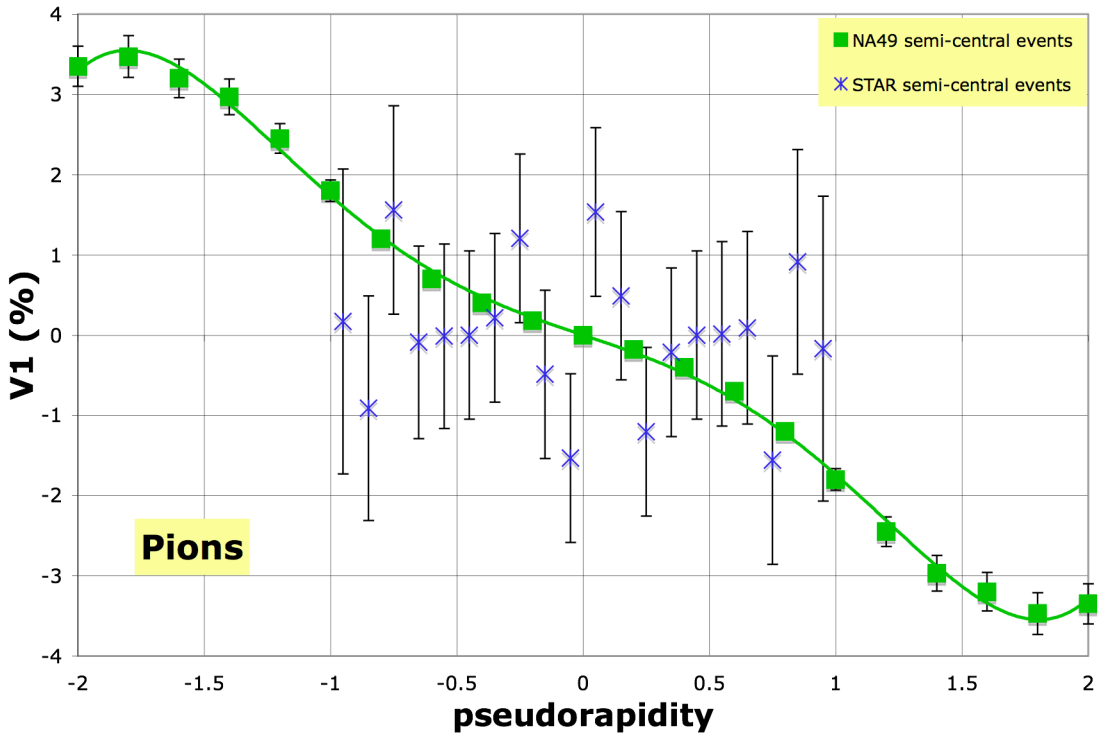

Figure 6.6: A plot of directed flow (v_1) of identified pions versus pseudorapidity for semi-central events in NA49 and STAR.

Figure 6.7 shows a plot of elliptic flow (v_2) of identified pions versus pseudorapidity for both NA49 and STAR. Because the NA49 experiment had acceptance only forward of mid-rapidity, the NA49 data were reflected about mid-rapidity. In order to reduce fluctuations, the STAR data were averaged and reflected about mid-rapidity. The rather large error bars in the STAR data were due to lack of statistics. Within statistics, the STAR result agrees with the NA49 result.

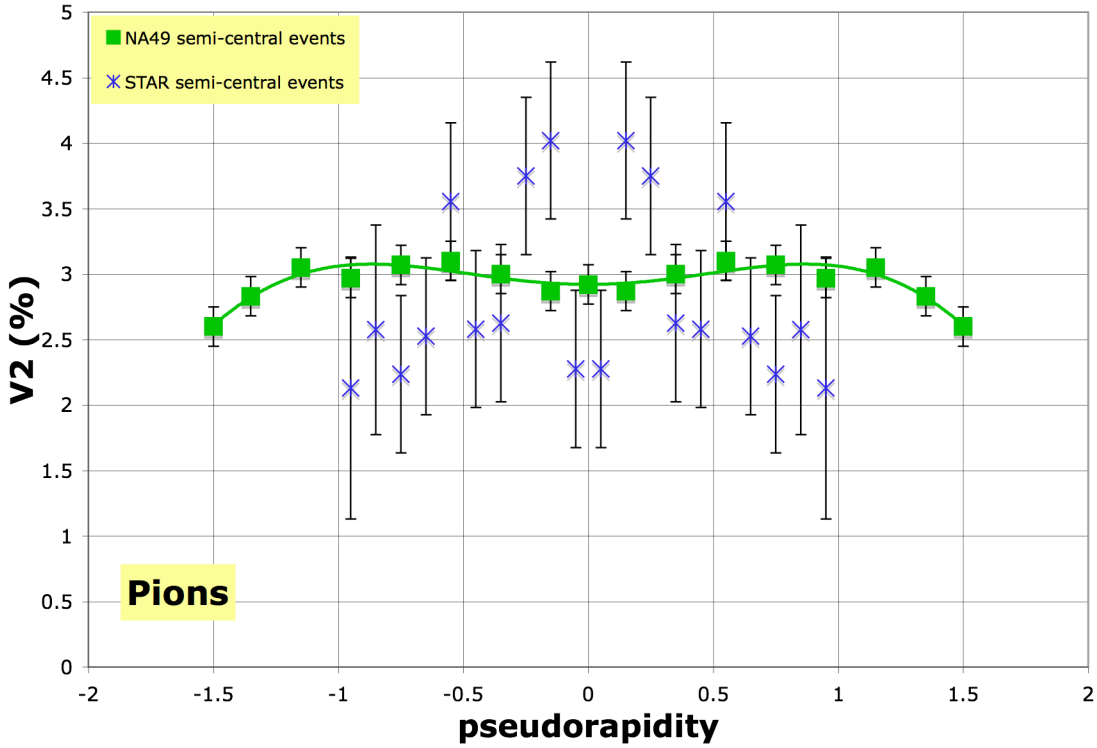

Figure 6.7: A plot of elliptic flow (v_2) of identified pions versus pseudorapidity for semi-central events in NA49 and STAR.

Figure 6.8 shows a plot of directed flow (v_1) of identified pions versus transverse momentum (p_T) for both NA49 and STAR. The rather large error bars in the STAR dataset were due to lack of statistics. As the transverse momentum increased, the statistics in the transverse momentum histogram bins decreased rapidly. Below 0.5 GeV/c, the STAR data are systematically above NA49.

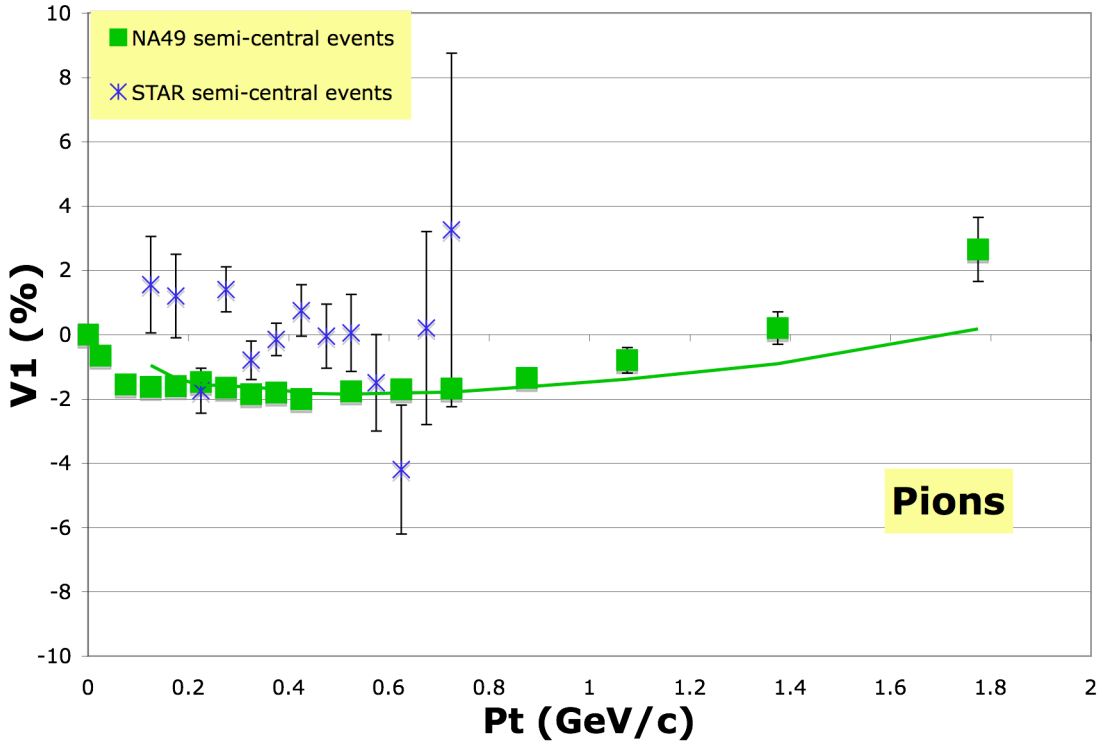

Figure 6.8: A plot of directed flow (v_1) of identified pions versus transverse momentum (p_T) for semi-central events in NA49 and STAR.

Figure 6.9 shows a plot of elliptic flow (v_2) of identified pions versus transverse momentum (p_T) for both NA49 and STAR. The rather large error bars in the STAR dataset were due to lack of statistics. As the transverse momentum increased, the statistics in the transverse momentum histogram bins decreased rapidly. The STAR results do not disagree with the NA49 results.

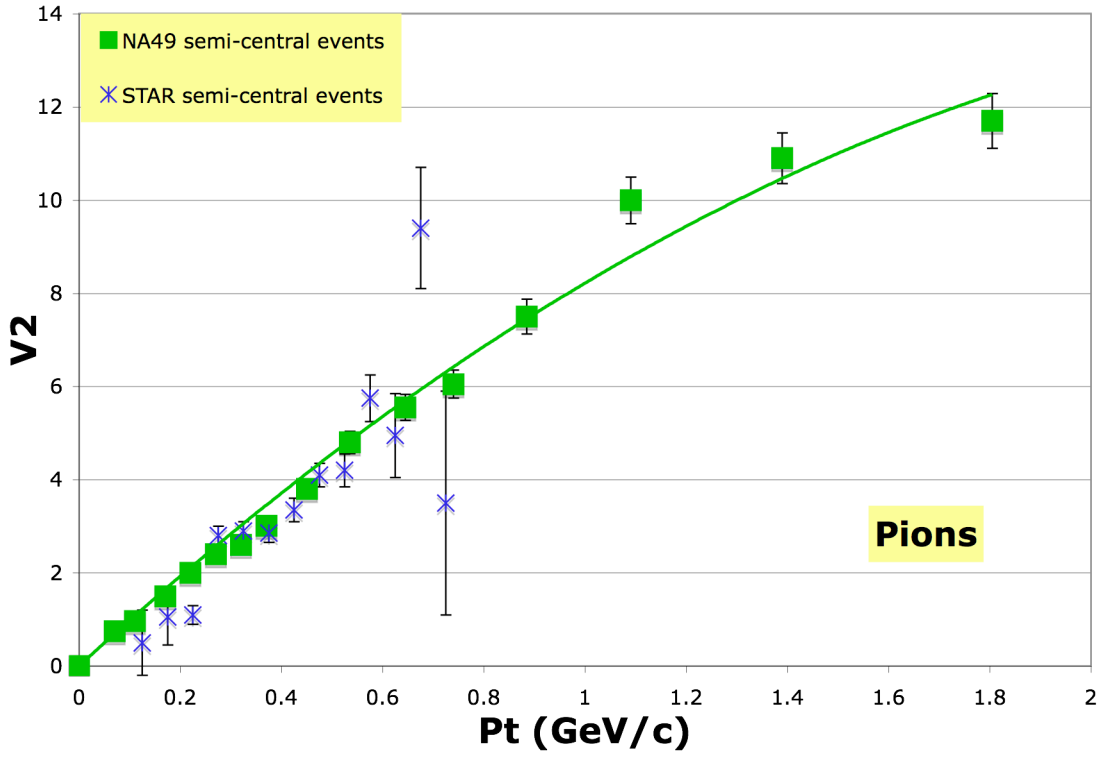

Figure 6.9: A plot of elliptic flow (v_2) of identified pions versus transverse momentum (p_T) for semi-central events in NA49 and STAR.

6.1.3 Central Events

This sub-section deals with central events (0% to 12.5% centrality). The STAR central bin contained 4,028 events that passed all of the cuts. NA49 used over 100,000 events in their central bin.

Figure 6.10 shows a plot of directed flow (v_1) of identified pions versus pseudorapidity for central events in NA49 and STAR. Because the NA49 experiment had acceptance only forward of mid-rapidity, the NA49 data were reflected about mid-rapidity. In order to reduce fluctuations, the STAR data were averaged and reflected about mid-rapidity. Within the large uncertainty in the STAR data, the results agree with each other.

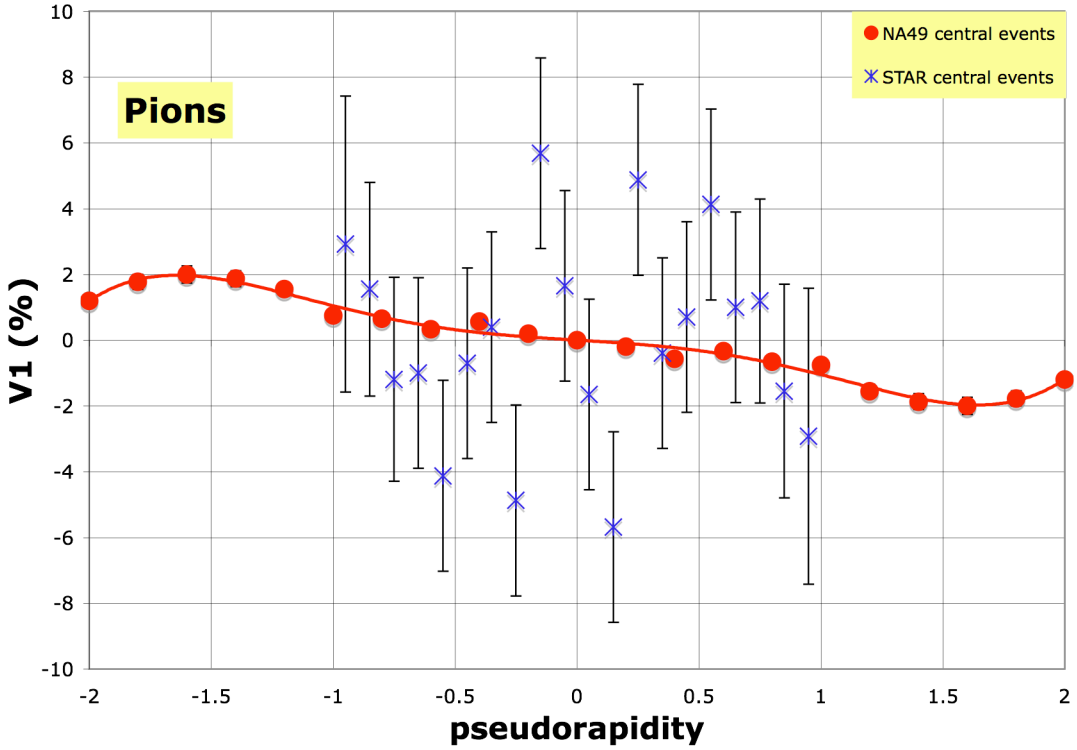

Figure 6.10: A plot of directed flow (v_1) of identified pions versus pseudorapidity for central events in NA49 and STAR.

Figure 6.11 shows a plot of elliptic flow (v_2) of identified pions versus pseudorapidity for both NA49 and STAR. Because the NA49 experiment had acceptance only forward of mid-rapidity, the NA49 data were reflected about mid-rapidity. In order to reduce fluctuations, the STAR data were averaged and reflected about mid-rapidity. The rather large error bars in the STAR data are due to lack of statistics. The STAR result agrees with the NA49 result.

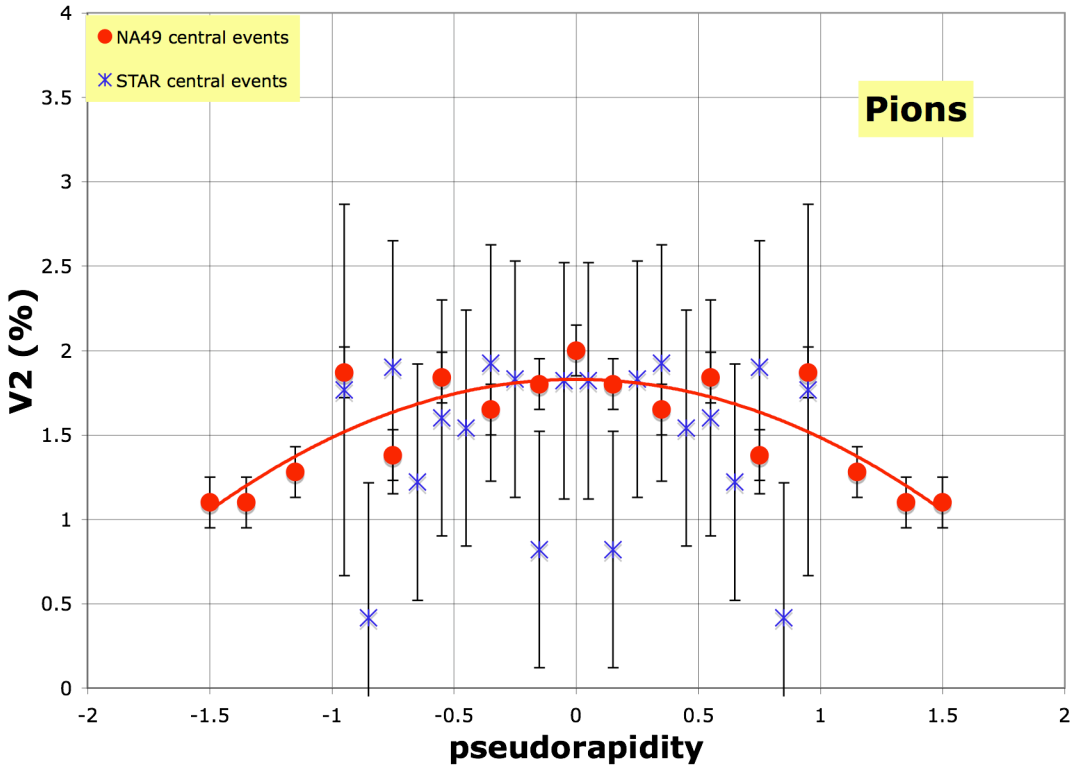

Figure 6.11: A plot of elliptic flow (v_2) of identified pions versus pseudorapidity for central events in NA49 and STAR.

Figure 6.12 shows a plot of directed flow (v_1) of identified pions versus transverse momentum (p_T) for both NA49 and STAR. The rather large error bars in the STAR dataset were due to lack of statistics. As the transverse momentum increased, the statistics in the transverse momentum histogram bins decreased rapidly. The STAR data agreed in trend with the NA49 data in the low transverse momentum region. The results do not disagree within statistics, except perhaps near 0.2 GeV/c.

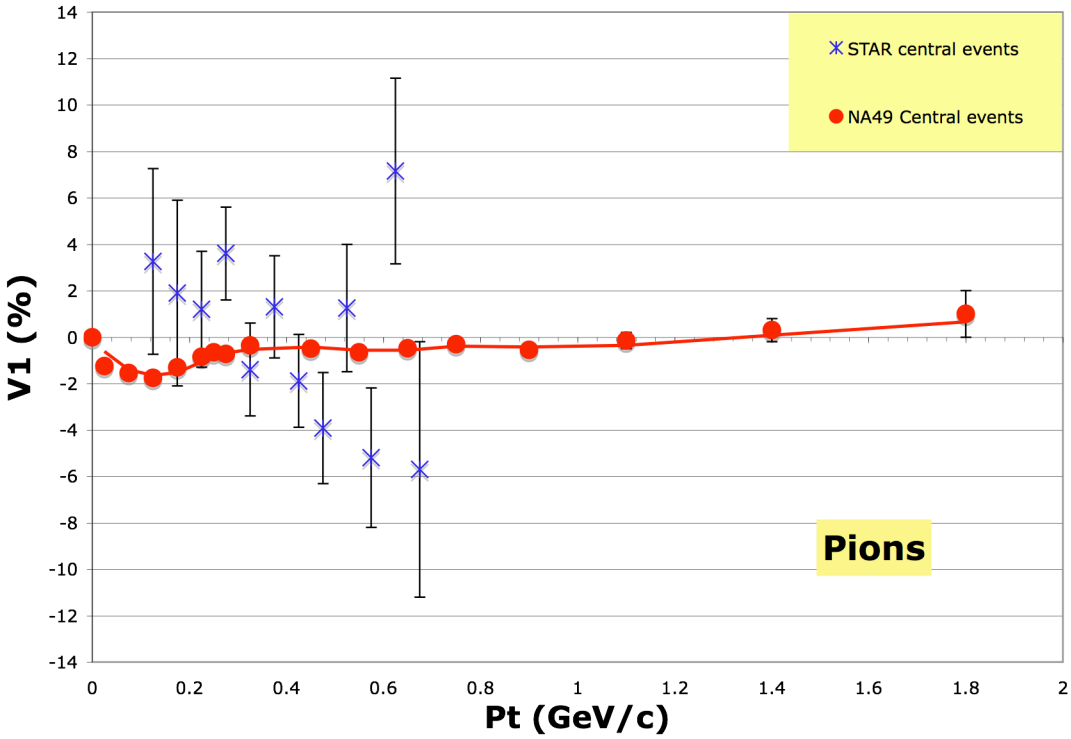

Figure 6.12: A plot of directed flow (v_1) of identified pions versus transverse momentum (p_T) for central events in NA49 and STAR.

Figure 6.13 shows a plot of elliptic flow (v_2) of identified pions versus transverse momentum (p_T) for both NA49 and STAR. A trendline curve was added to the graph that is only meant to guide the eye. The rather large error bars in the STAR dataset were due to lack of statistics. As the transverse momentum increased, the statistics in the transverse momentum histogram bins decreased rapidly. The STAR result does not disagree with the NA49 result within statistics.

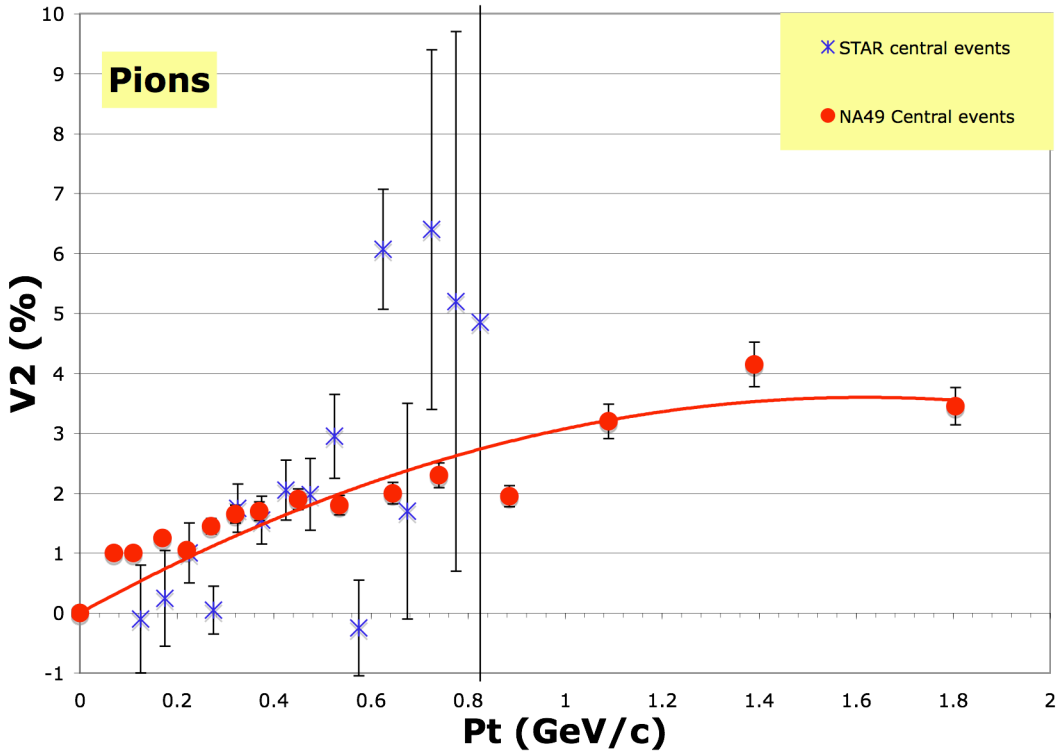

Figure 6.13: A plot of elliptic flow (v_2) of identified pions versus transverse momentum (p_T) for central events in NA49 and STAR.

6.1.4 Events with All Centralities

This sub-section deals with events containing all centralities (*i.e.* minimum bias events). STAR minimum bias contained 31,022 events that passed all of the cuts. NA49 used over 500,000 events in their minimum bias analysis.

Figure 6.14 shows a plot of directed flow (v_1) of identified pions versus pseudorapidity for minimum bias events in NA49 and STAR. Note that the systematic errors dominate the STAR error bars here. Because the NA49 experiment had acceptance only forward of mid-rapidity, the NA49 data were reflected about mid-rapidity. In order to reduce fluctuations, the STAR data were averaged and reflected about mid-rapidity. The results agree with each other within error bars.

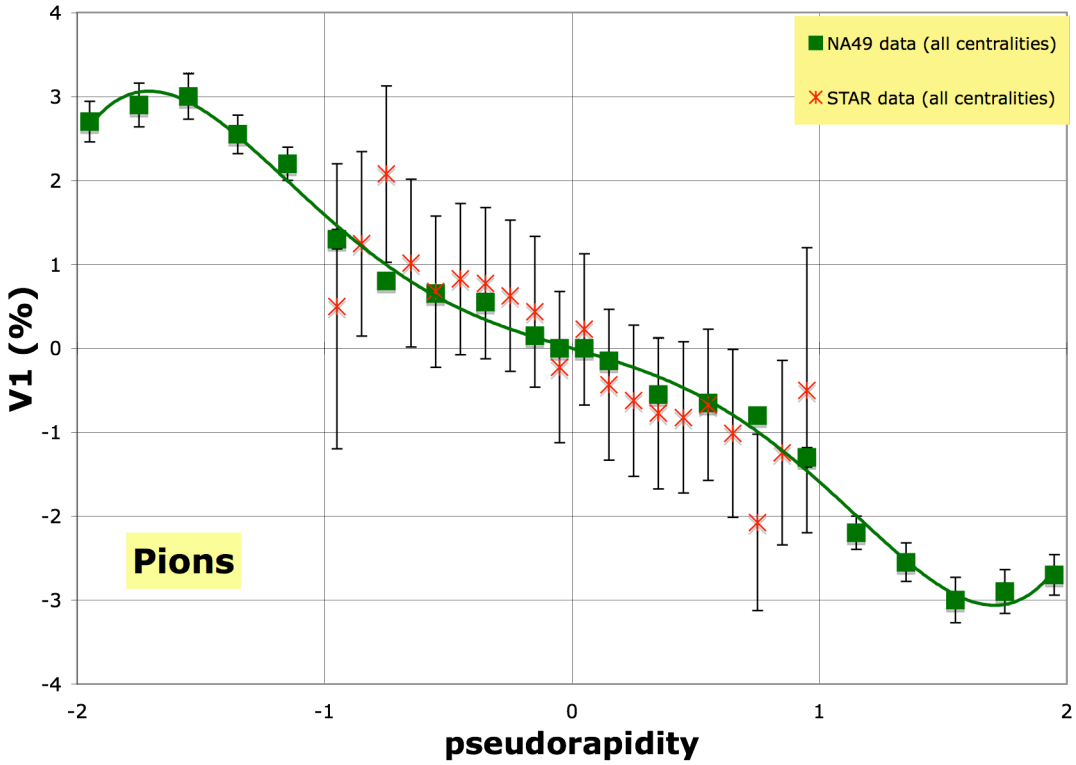

Figure 6.14: A plot of directed flow (v_1) of identified pions versus pseudorapidity for minimum bias events in NA49 and STAR. Note that the systematic errors dominate here.

Figure 6.15 shows a plot of elliptic flow (v_2) of identified pions versus pseudorapidity for minimum bias events in NA49 and STAR. Because the NA49 experiment had acceptance only forward of mid-rapidity, the NA49 data were reflected about mid-rapidity. In order to reduce fluctuations, the STAR data were averaged and reflected about mid-rapidity. The rather large error bars in the STAR data were due to lack of statistics. The STAR elliptic flow result does not disagree with the NA49 elliptic flow result except possibly near midrapidity.

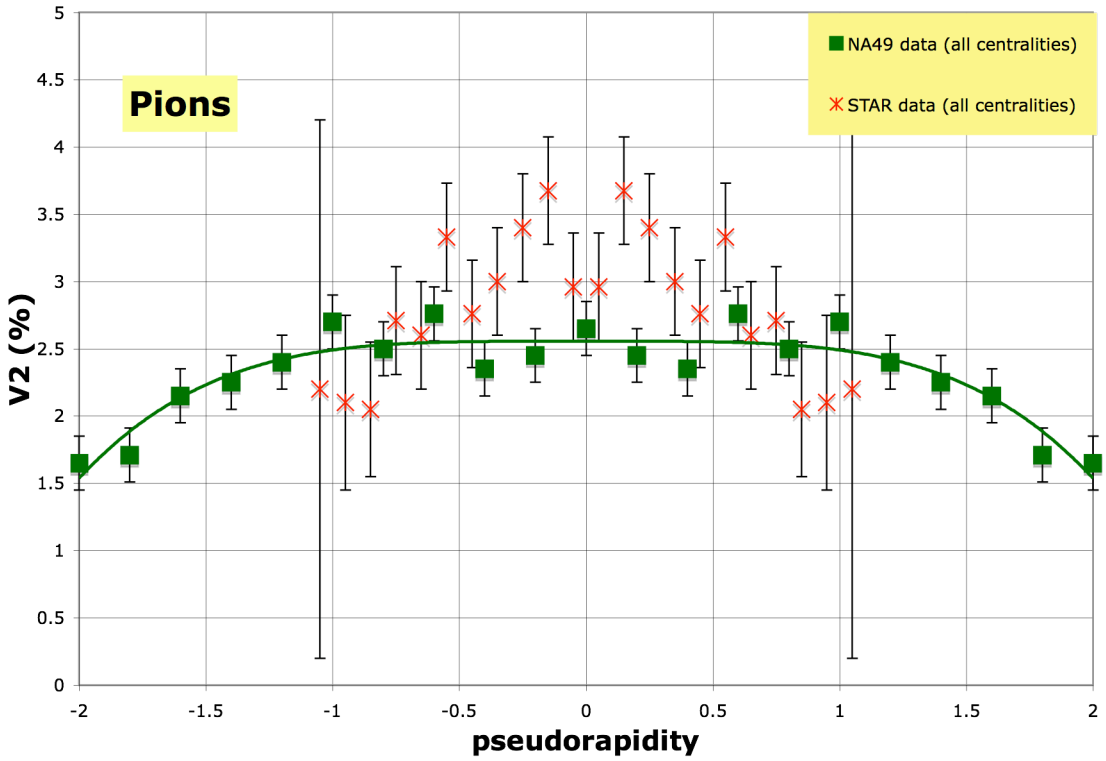

Figure 6.15: A plot of elliptic flow (v_2) of identified pions versus pseudorapidity for minimum bias events in NA49 and STAR.

Figure 6.16 shows a plot of directed flow (v_1) of identified pions versus transverse momentum (p_T) for minimum bias events in NA49 and STAR. As the transverse momentum increased, the statistics in the transverse momentum histogram bins decreased rapidly. The STAR result does not disagree with the NA49 result.

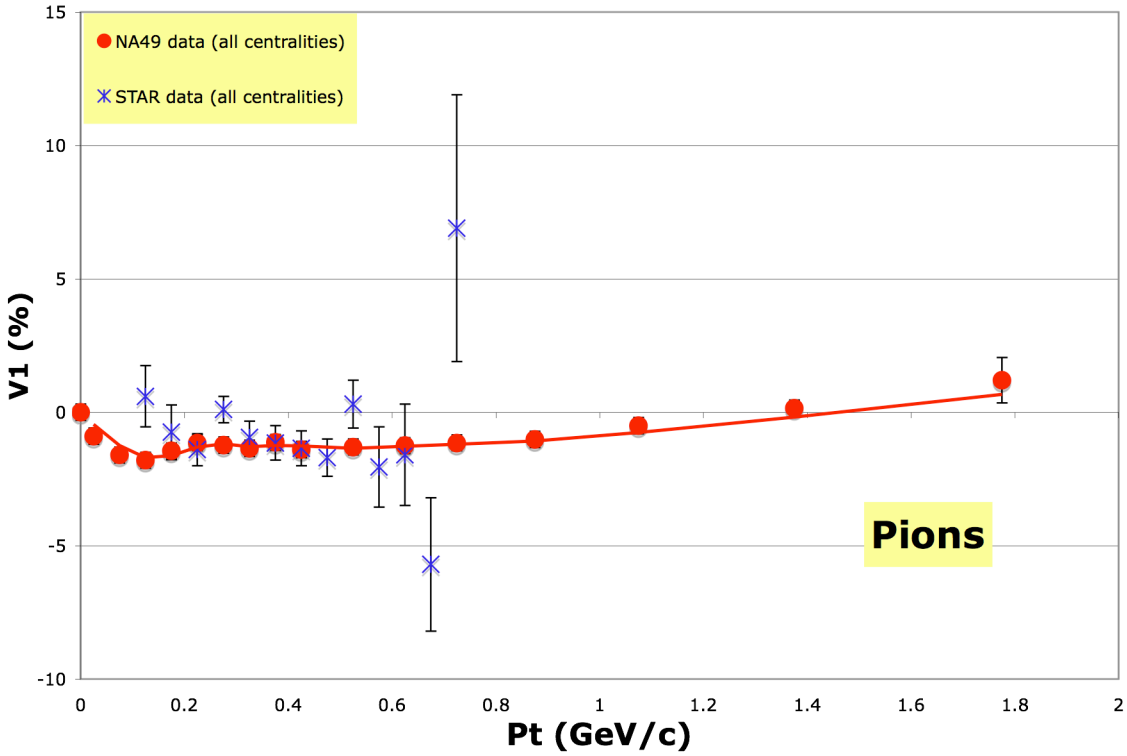

Figure 6.16: A plot of directed flow (v_1) of identified pions versus transverse momentum (p_T) for minimum bias events in NA49 and STAR.

Figure 6.17 shows a plot of elliptic flow (v_2) of identified pions versus transverse momentum (p_T) for minimum bias events in NA49 and STAR. As the transverse momentum increased, the statistics in the transverse momentum histogram bins decreased rapidly. The STAR directed flow result is significantly above the NA49 values near a transverse momentum of 0.6 GeV/c.

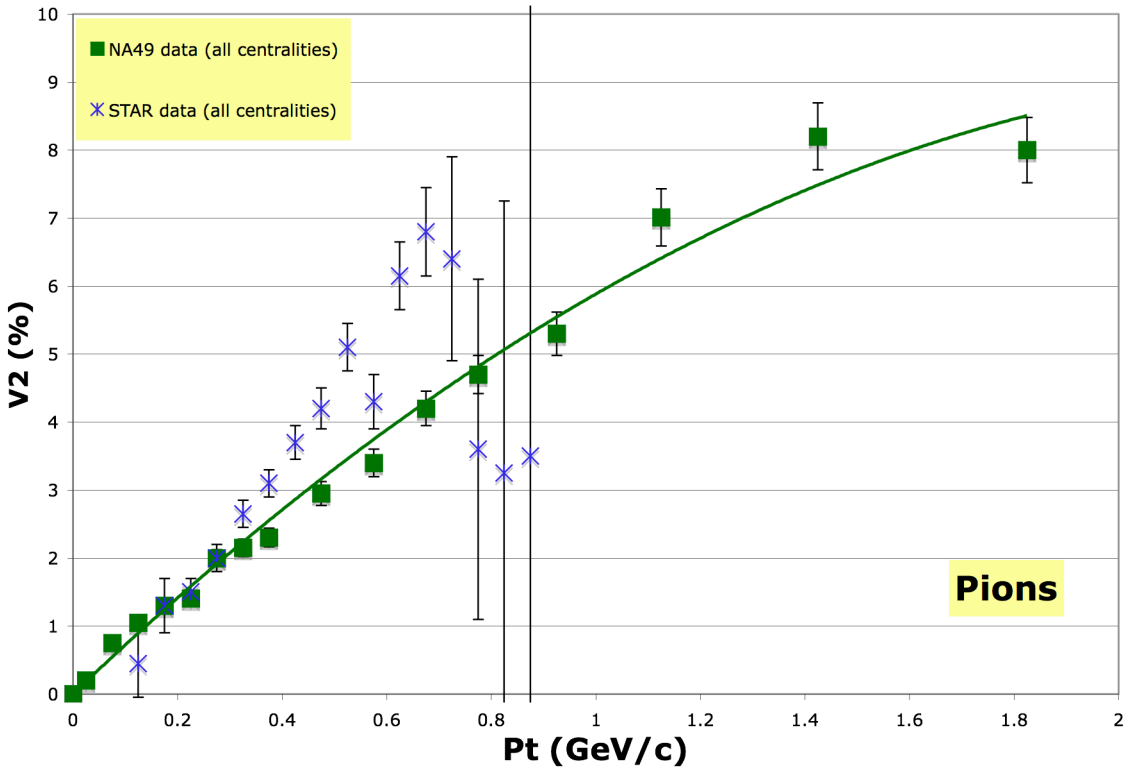

Figure 6.17: A plot of elliptic flow (v_2) of identified pions versus transverse momentum (p_T) for minimum bias events in NA49 and STAR.

6.2 Comparisons to PHOBOS

The STAR data presented in this section were analyzed in a manner to compare most directly with the PHOBOS results. PHOBOS used the same beam as STAR did. There is a brief description of PHOBOS in subsection 1.5.3. All of the PHOBOS data in this section was extracted from the following reference, [Mignerey 2005].

In order to compare to the PHOBOS flow results, all charged particles were selected since PHOBOS does not have any PID capability. The events were in a centrality bin which represent the top 40% central events.

Figure 6.18 shows a plot of directed flow (v_1) versus pseudorapidity for the top 40% central events in PHOBOS and STAR. In order to reduce fluctuations, the STAR

data were averaged and reflected about mid-rapidity. The results agree with each other within error bars.

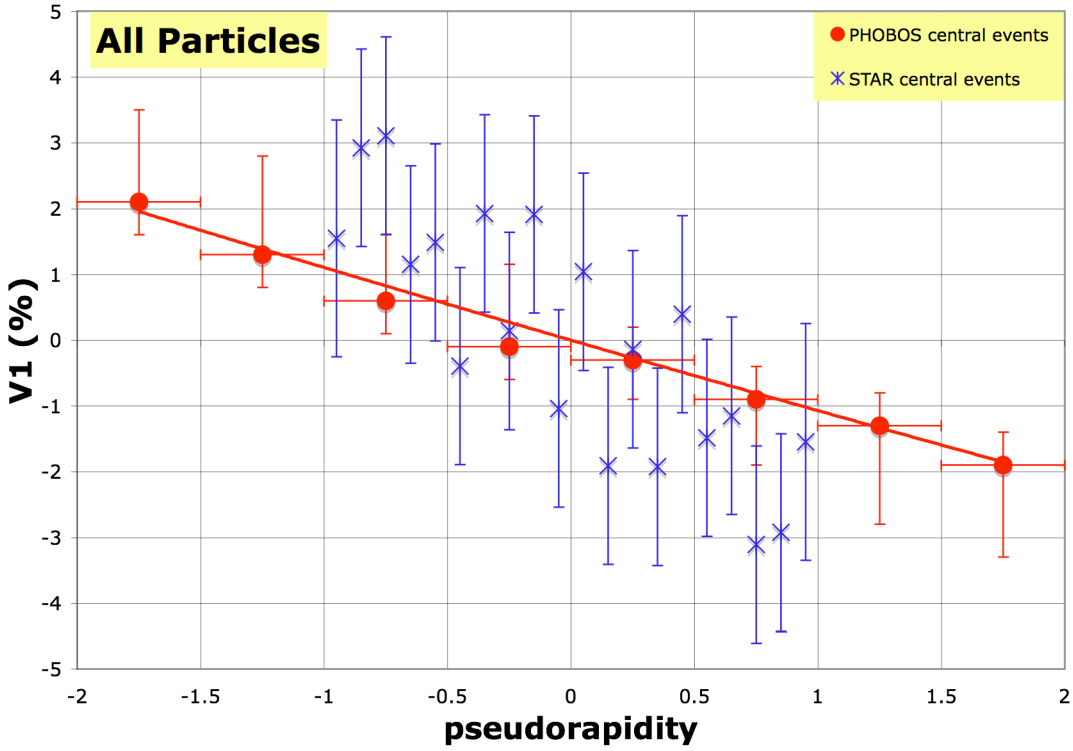

Figure 6.18: A plot of directed flow (v_1) versus pseudorapidity for the top 40% central events in PHOBOS and STAR.

Figure 6.19 shows a plot of elliptic flow (v_2) versus pseudorapidity for the top 40% central events in PHOBOS and STAR. In order to reduce fluctuations, the STAR data were averaged and reflected about mid-rapidity.

The STAR result agrees with the PHOBOS result. PHOBOS had an elliptic flow value of about $3.36 \pm 1.09\%$ for pseudorapidity bins that were between –1 and 1. STAR had an elliptic flow value of about $3.12 \pm 0.27\%$ for pseudorapidity bins that were between –1 and 1.

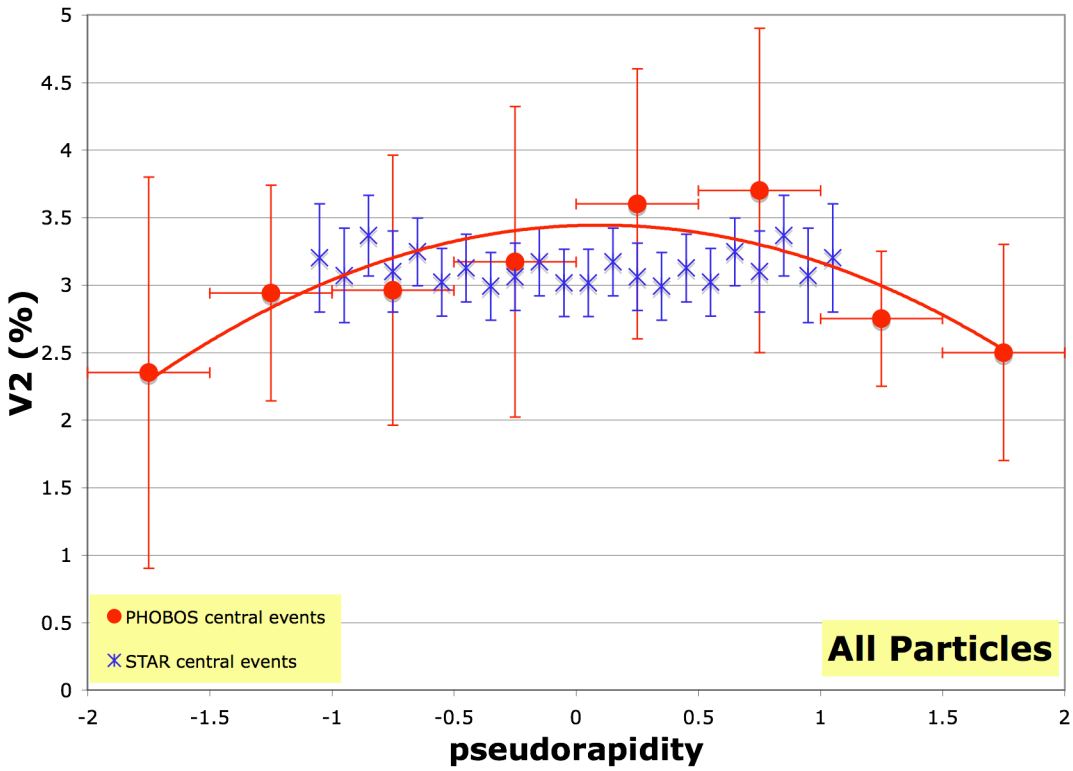

Figure 6.19: A plot of elliptic flow (v_2) versus pseudorapidity for the top 40% central events in PHOBOS and STAR.

6.3 Comparisons to CERES

The STAR data presented in this section were analyzed in a manner to compare most directly with the CERES results. CERES was an experiment at the SPS, which ran at a center of mass energy of 17.2 GeV per nucleon for Pb on Pb collisions. This is similar to the 19.6 GeV STAR data set which is presented in this thesis. The CERES experiment was briefly described in section 1.5.1. All of the CERES data in this section was extracted from the following reference, [Slivova 2003]. The NA49 data in this section was extracted from the following reference, [Alt 2003].

In order to compare to the CERES flow results, all charged particles were selected. The CERES events were separated into a centrality bin which represent the

15% to 30% centrality. The STAR centrality bin that most closely represented the CERES bin was the semi-central bin with a centrality between 10% to 30%.

Figure 6.20 shows a plot of elliptic flow (v_2) versus transverse momentum (p_T) for the semi-central events in CERES and STAR. The results agree with each other within error bars.

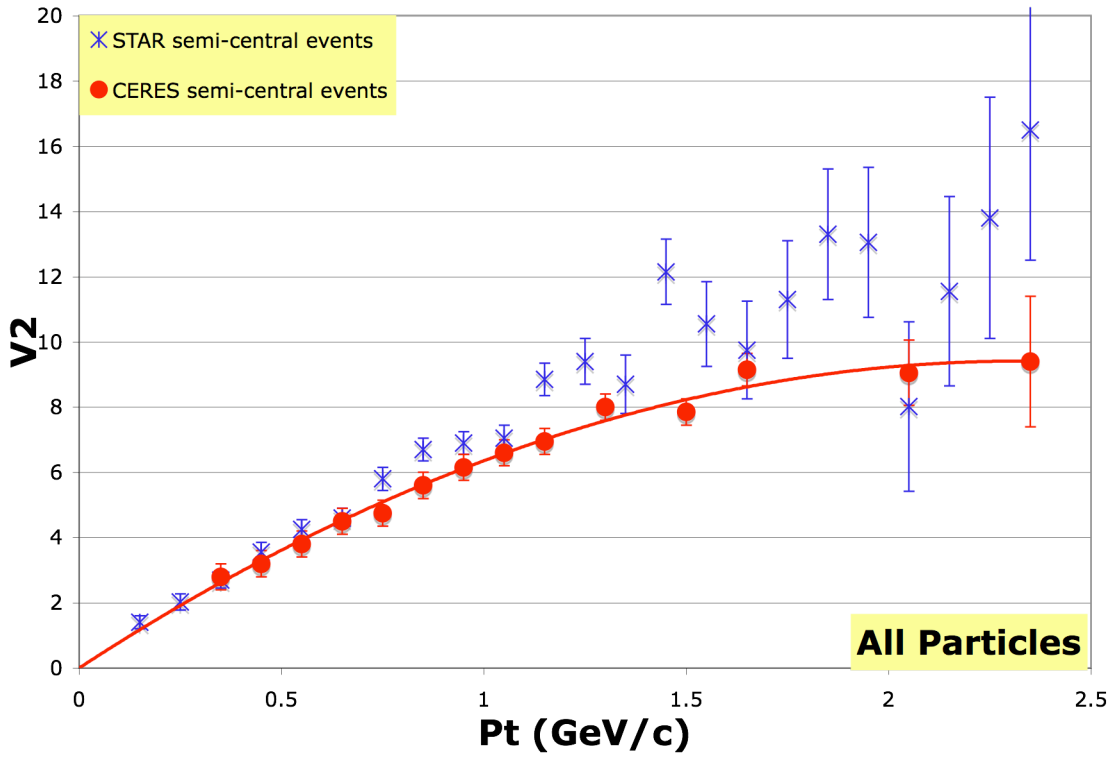

Figure 6.20: A plot of elliptic flow (v_2) versus transverse momentum (p_T) for the semi-central events in CERES and STAR.

Figure 6.21 shows a plot of elliptic flow (v_2) versus transverse momentum (p_T) for pions for semi-central events in NA49, CERES and STAR. The STAR results slightly favor the NA49 results for transverse momentum below 0.6 GeV/c.

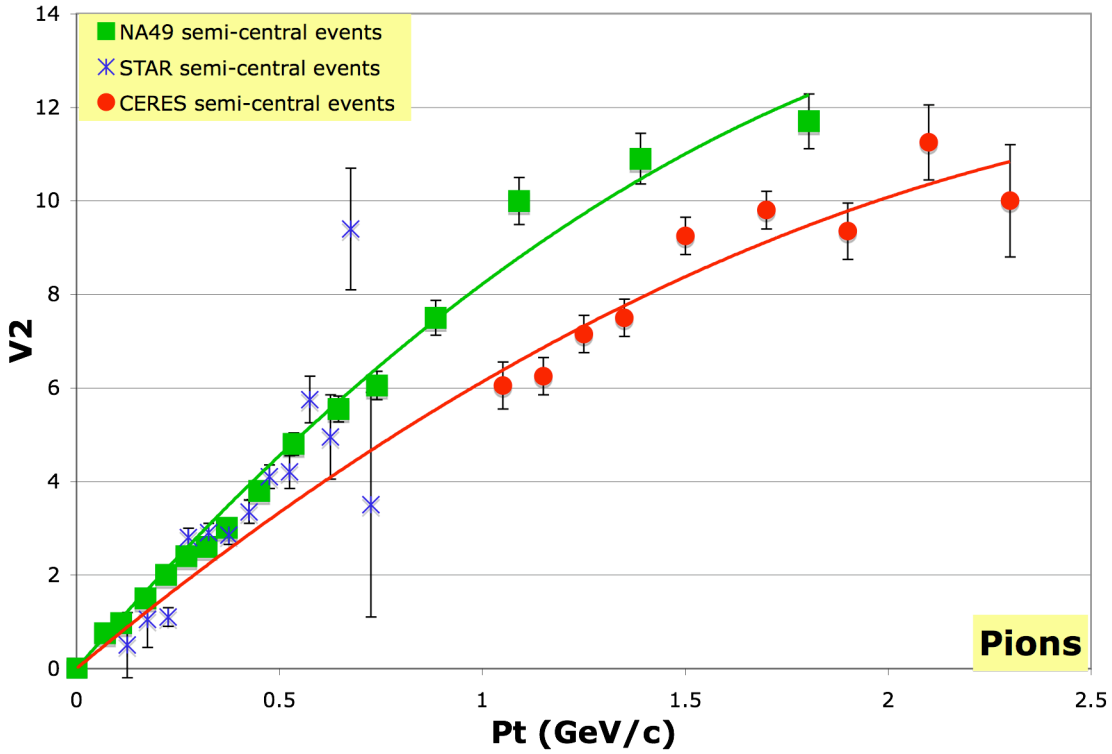

Figure 6.21: A plot of elliptic flow (v_2) versus transverse momentum (p_T) for pions for semi-central events in NA49, CERES, and STAR.

6.4 Excitation Function

A common comparison for various experiments at different energies is the "excitation function" plot. Here elliptic flow is plotted against center of mass energy.

Figure 6.22 shows an excitation function plot of elliptic flow (v_2) versus center of mass energy per nucleon-nucleon pair for various experiments. The events represented in this plot were mid-central collisions (approximately 10% to 33% centrality). All of the NA49, PHENIX, PHOBOS, CERES, and E877 data in this section came from the following reference, [Alt 2003]. The E895 data came from the following reference, [Pinkenburg 1999]. The STAR 20 GeV data included separate data points for pions and all charged particles. The NA49 data points were for pions. The STAR, PHENIX, PHOBOS, CERES, E895, and E877 data points were for all charged particles.

The STAR 20 GeV data points fit nicely with the rest of the data points. These STAR elliptic flow results are in agreement with the published SPS results, confirming consistency between the facilities and experiments. Elliptic flow increases monotonically with increasing center of mass energy with no signs of localized structure.

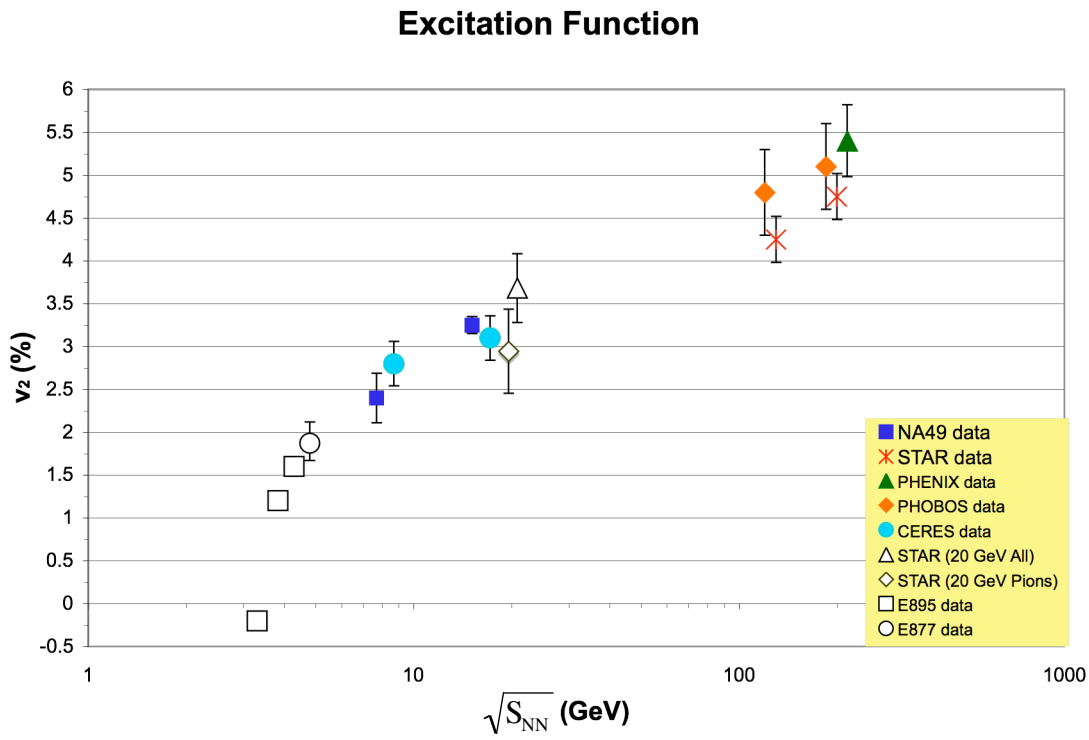

Figure 6.22: An excitation function plot of elliptic flow (v_2) versus center of mass energy per nucleon-nucleon pair for various experiments.

Chapter 7

Conclusions

Figure 7.1: An artist's interpretation of the writing of this thesis [Schultz 1965].

7.1 Conclusion

Writing this thesis has been a challenging experience. Figure 7.1 on the previous page shows an artist's interpretation of the writing of this thesis.

The elliptic flow results presented in this thesis are in agreement with the published SPS results, confirming consistency between the facilities and experiments. This can be easily observed by examining the excitation function in Chapter 6 (Figure 6.22). Elliptic flow (v_2) increases monotonically with increasing center of mass energy with no sign of structure.

The magnitude of directed flow (v_1) increases with pseudorapidity. This can be easily observed by examining directed flow plots in Chapter 5. There is an asymmetry of directed flow about zero pseudorapidity driven by the symmetry of Au+Au collisions. The magnitude of elliptic flow is maximum when pseudorapidity is zero. This can be easily observed by examining elliptic flow plots in Chapter 5. There is a symmetry of elliptic flow about zero pseudorapidity driven by the symmetry of Au+Au collisions. These conclusions are consistent with previous published results.

As a function of transverse momentum, p_T, directed flow is relatively flat within our statistics. This can be easily observed by examining directed flow plots in Chapter 5. As a function of transverse momentum, elliptic flow increases with transverse momentum up to about 1.5 GeV. This can be easily observed by examining elliptic flow plots in Chapter 5. These conclusions are consistent with previous published results.

Directed flow decreases as the collisions become more central due to simple symmetry. Perfectly central collisions should have $v_1 = 0$ and $v_2 = 0$. This tendency can be observed by examining the tables in section 5.4. These tendencies are consistent with previous published results.

Also, by comparing the results in section 5.2 and section 5.3 we find that the results do not change significantly when selecting only on pions as opposed to choosing all charged particles. This is largely because pions dominate the yields. The ratio of

yields of positively charged pions to protons is about 9.0 to one. The ratio of yields of all charged pions to protons plus anti-protons is about 17 to one. The ratio of yields of positively charged kaons to protons is about 0.20 to one. Also, the ratio of yields of all charged kaons to protons plus anti-protons is about 0.35 to one.

Abbreviations

ADC	Analog to Digital Converter
AGS	Alternating Gradient Synchrotron
AGeV	(mass number)xGeV/nucleon
ATR	AGS-to-RHIC transfer line
Au	Gold
BNL	Brookhaven National Laboratory
BRAHMS	Broad Range Hadron Magnetic Spectrometers
CTB	Central Trigger Barrel
DAQ	Data AcQuisition
DCA	Distance of Closest Approach
EMC	ElectroMagnetic Calorimeter
EOS	Equation Of State
FEE	Front-End Electronics
FTPC	Forward Time Projection Chambers
GeV	GigaElectronVolts
HBT	Hanbury-Brown-Twiss
ICARUS	Imaging Cosmic And Rare Underground Signal
LASER	Light Amplification by Stimulated Emission of Radiation
LBNL	Lawrence Berkeley National Laboratory

Abbreviations

MUSIC	MUltiple Sampling Ionization Chamber
MV	MegaVolt
MWPC	Multi-Wire Proportional Chamber
Nd-YAG	Neodymium-Yttrium Aluminum Garnet
NLO	Next-to-Leading-Order
Pb	Lead
PID	Particle IDentification
PMT	Photo-Multiplier Tube
pQCD	perturbative Quantum ChromoDynamics
p_T	transverse momentum
QGP	Quark-Gluon Plasma
RDO	ReaDOut
RF	Radio Frequency
RHIC	Relativistic Heavy-Ion Collider
RICH	Ring Imaging CHerenkov
SAS	STAR preAmplifier/Shaper
SCA	Switched Capacitor Array
SCA/ADC	Switched Capacitor Array/Analog to Digital Converter
SLAC	Stanford Linear Acclerator Center

Abbreviations

SPS	Super Proton Synchrotron
STAR	Solenoidal Tracker At RHIC
STP	Standard Temperature and Pressure
SVT	Silicon Vertex Tracker
TEC	Time Expansion Chamber
TOF	Time-Of-Flight
TPC	Time Projection Chamber
TtB	Tandem to Booster
ZDC	Zero Degree Calorimeter

Bibliography

Abbott T. *et al.*, the E917 Collaboration, *Nuclear Instruments and Methods* **A290**, (1990) 41.

Abele, J. *et al.*, the STAR Collaboration, *Nuclear Instruments and Methods* **A499**, (2003) 692.

Abreu, M.C. *et al.*, the NA50 Collaboration, *Nuclear Physics B – Proceedings Supplements* **92**, (2001) 55.

Abreu, M.C. *et al.*, the NA50 Collaboration, *Physics Letters* **B410**, (1997) 327.

Ackermann, K. *et al.*, the STAR Collaboration, *Physical Review Letters* **86**, (2001) 402.

Adamczyk, M. *et al.*, the BRAHMS Collaboration, *Nuclear Instruments and Methods* **A499**, (2003) 437.

Adams, J. *et al.*, the STAR Collaboration, *Physical Review Letters* **91**, (2003) 262301.

Adams, J. *et al.*, the STAR Collaboration, *Physical Review Letters* **92**, (2004) 062301.

Adcox, K. *et al.*, the PHENIX Collaboration, *Nuclear Instruments and Methods* **A499**, (2003) 469.

Adcox, K. *et al.*, the PHENIX Collaboration, *Physical Review Letters* **89**, (2002) 212301.

Adler, C. *et al.*, the STAR Collaboration, *Nuclear Instruments and Methods* **A470**, (2001) 488.

Adler, S. *et al.*, the PHENIX Collaboration, *Physical Review Letters* **91**, (2003) 182301.

Adler, S. *et al.*, the PHENIX Collaboration, *Physical Review Letters* **94**, (2005) 232302.

Afanasiev, S. *et al.*, the NA49 Collaboration, *Nuclear Instruments and Methods* **A430**, (1999) 210.

Agakichiev, G. *et al.*, the CERES Collaboration, *Nuclear Instruments and Method* **A371**, (1996) 16.

Bibliography

Aggarwal, M. *et al*., the WA98 Collaboration, *Nuclear Physics* **A610**, (1996) 200c.

ALEPH Collaboration, The ALEPH Handbook, ALEPH 89-77 (1989).

Alt, C. *et al.*, the NA49 Collaboration, *Physical Review* **C68**, (2003) 034903.

Anderson, M. *et al*., the STAR Collaboration, *Nuclear Instruments and Methods* **A499**, (2003) 659.

Arneodo, F. *et al*., *Nuclear Instruments and Methods* **A461**, (2001) 324.

Atwood, W. *et al*., *Nuclear Instruments and Methods* **A306**, (1991) 446.

Back, B. *et al.*, the E917 Collaboration, Prepared for Centennial Celebration and Meeting of the American Physical Society (Combining Annual APS General Meeting and the Joint Meeting of the APS and the AAPT), Atlanta, Georgia, 20-26 Mar (1999).

Back, B. *et al.*, the PHOBOS Collaboration, *Journal of Physics G* **31**, (2005) S41.

Barrette, J. *et al.*, the E877 Collaboration, *Physics Letters* **B485**, (2000) 319.

Barrette, J. *et al.*, the E877 Collaboration, *Physical Review* **C59**, (1999) 884.

Bass, S.A. *et al*., *Nuclear Physic*s **A661**, (1999) 205.

Bathe, S. for the PHENIX Collaboration, e-Print Archive: nucl-ex/0511041, (2005).

Bauer, G. *et al.*, *Nuclear Instruments and Methods* **A386**, (1997) 249.

Beddo, M. *et al.*, the STAR Collaboration, *Nuclear Instruments and Methods* **A499**, (2003) 725.

Bellwied, R. *et al*., the STAR Collaboration, *Nuclear Instruments and Methods* **A499**, (2003) 640.

Bergsma, F. *et al.*, the STAR Collaboration, *Nuclear Instruments and Methods* **A499**, (2003) 633.

Bibliography

Bieser, F. *et al.*, the STAR Collaboration, *Nuclear Instruments and Methods* **A499**, (2003) 766.

Bjorken, J.D. *Physical Review* **D27**, (1983) 140.

BNL, Images located at www.bnl.gov/RHIC/ (2006).

Bonner, B. *et al.*, the STAR Collaboration, *Nuclear Instruments and Methods* **A508**, (2003) 181.

Braem, A. *et al.*, the STAR Collaboration, *Nuclear Instruments and Methods* **A499**, (2003) 720.

BRAHMS Collaboration, Interim Design Report for the BRAHMS Experiment at RHIC, BNL Report, (1994).

Caines, H. for the STAR Collaboration, *Nuclear Physics* **A698**, (2002) 112c.

Cebra, D. for the STAR Collaboration, "dN/dy and mT distributions for charged pion, charged kaon, proton and antiproton production from AuAu Collisions at 19.6 GeV," poster presentation at *2002 Quark Matter in Nantes, France*, (2002).

Danielewicz, P. and Odyniec G., *Physics Letters* **B157**, (1985) 146.

Eckhardt, V. *et al.*, for the NA35 Collaboration, *Nuclear Instruments and Methods* **A315**, (1992) 33.

Enokizono, A. for the PHENIX Collaboration, *Nuclear Physics* **A715**, (2003) 595c.

Filimonov, K. for the E877 Collaboration, *Nuclear Physics* **A661**, (1999) 198c.

FTPC Collaboration, The Forward Time Projection Chamber For the STAR Detector, MPI-PhE/98-3, (1998).

Glauber, R.J. *Physical Review* **130**, (1963) 2766.

Gonin, M. for the NA50 Collaboration, *Nuclear Physics* **A610**, (1996) 404c.

Bibliography

Gutbrod, H. *et al.*, *Physical Review* **C42**, (1990) 640.

Hanbury-Brown, R. and Twiss, R. Q., *Philosophical Magazine Nature* **178**, (1956) 1046.

Hofman, W. "Recent Results from the PEP4-TPC on Quark Fragmentation," in *1983 Proceedings of the SLAC Summer Institute on Particle Physics: Dynamics and Spectroscopy at High Energy*, in Palo Alto, CA, (1983), available online at: http://www.slac.stanford.edu/pubs/confproc/ssi83/ssi83-022.html.

Johnson, I.J. for the STAR Collaboration, *Nuclear Physics* **A715**, (2003) 691c.

Kapusta, J. *et al.*, "High-Energy Photons from Quark Gluon Plasma Versus Hot Hadronic Gas," in *7th Winter Workshop on Nuclear Dynamics*, in Key West, FL, (1991).

Kolb, P. *Physical Review* **C68**, (2003) 031902.

Kolb, P., Sollfrank, J., and Heinz, U. *Physical Review* **C62**, (2000) 054909.

Lebedev, A. for the WA98 Collaboration, *Nuclear Physics* **A698**, (2002) 135c.

Lisa, M. e-Print Archive: nucl-ex/0512008 (2005).

Lohse, T. and Witzeling W. "The Time Projection Chamber," *European Organization for Nuclear Research***,** C.E.R.N., 1211 Geneva 23, Switzerland (n.d.).

Ludlam, T. and McLerran L. "What Have We Learned From the Relativistic Heavy Ion Collider," *Physics Today*, Volume 56, Issue 10, October (2003) 48.

Manly, S. for the PHOBOS Collaboration, *Nuclear Physics* **A715**, (2003) 611c.

Manzari V. for the NA57 Collaboration, *Nuclear Physics* **A715**, (2003) 140c.

Matsui, T. and Satz, H. *Physics Letters* **B178**, (1986) 416.

Mignerey, S. for the PHOBOS Collaboration, e-Print Archive: nucl-ex/0510030 (2005).

NA49, Images located at na49info.cern.ch (2006).

Bibliography

Nagle, J.L. and Ullrich, T.S. "Heavy Ion Experiments At RHIC: The First Year," Published in *Cargese 2001, QCD perspectives on hot and dense matter* (2002) 257.

Nouicer, R. for the PHOBOS Collaboratioin, *Nuclear Instruments and Methods* **A461**, (2001) 143.

Nygren, D. **PEP 198** (1975).

Ollitrault, J. *Physical Review* **D48**, (1993) 1132.

Ollitrault, J. e-Print Archive: nucl-ex/9711003 (1997).

Ollitrault, J. e-Print Archive: nucl-ex/9802005 (1998).

Pandey, S. for the STAR Collaboration, *Nuclear Physic*s **A661**, (1999) 686c.

PHENIX Experiment at RHIC – Preliminary Conceptual Design Report, PHENIX Collaboration Report (1992).

PHOBOS Collaboration, RHIC Letter of Intent to Study Very Low pt Phenomena at RHIC, PHOBOS Collaboration (1991).

Pinkenburg, C. *et al*., for the E895 Collaboration, *Physical Review Letters* **83**, (1999) 1295.

Picha, R. for the STAR Collaboration, "Midrapidity Charged Hadron Spectrra in STAR Au+Au Collisions at 19.6 GeV," presented at *2003 APS Meeting in Philadelphia, PA* (2003).

Poskanzer, A. and Voloshin, S. *Physical Review* **C58**, (1998) 1671.

Rafelski, J. and Muller, B. *Physical Review Letters* **48**, (1982) 1066.

Rai, G. *et al.*, *IEEE Transactions on Nuclear Science* **37**, (1990) 56.

Rischke, D. and Gyulassy, M. *Nuclear Physics* **A608**, (1996) 479.

Bibliography

Roser, T. *Nuclear Physics* **A698**, (2002) 23c.

Schlagheck, H. for the WA98 Collaboration, *Nuclear Physic*s **A661**, (1999) 337c.

Schultz, Charles M. Images located at www.unitedmedia.com/comics/peanuts (1965).

Shuryak, E.V. *Physical Review* **C66**, (2002) 027902.

Shuryak, E.V. *Soviet Journal Nuclear Physics* **28(3)**, (1978) 408.

Slivova, J. for the CERES Collaboration, *Nuclear Physics* **A715**, (2003) 615c.

Soff, S. *et al*., e-Print Archive: nucl-th/9903061 (1999).

Sorge, H. *Physical Review Letters* **82**, (1999) 2048.

STAR Collaboration, Images located at www.star.bnl.gov/STAR/img/images.html (2006).

STARTrig, Images located at www.star.bnl.gov/STAR/html/trg_l/.introduction/ (2006).

STAR Collaboration, Conceptual Design Report for the Solenoidal Tracker At RHIC, LBL/PUB-5347, (1992).

STARnote 229, Matis, H. *et al*., "STAR Geometry," (1998).

STARnote 270, Wells, R., "Gas System Operation at BNL," (1997).

STARnote 407, Betts, W., Anderson, M., and Wieman, H., "STAR TPC Temperature Monitoring System," (1999).

Suire, C. for the STAR Collaboration, *Nuclear Physic*s **A715**, (2003) 470c.

Tang, A. *et al*., the STAR Collaboration, *Journal of Physics G* **31**, (2005) S35.

Vogt, R. *Nuclear Physic*s **B360**, (1991) 67.

Bibliography

Voloshin, S. for the E877 Collaboration, *Nuclear Physic*s **A638**, (1998) 455c.

Wang, G. for the STAR Collaboration, *Quark Matter 2005* e-Print Archive: nucl-ex/0510034 (2005).

Wieman, H. *et al.*, the STAR Collaboration, *IEEE Transactions on Nuclear Science* Vol. 44, No. 3, (June 1997) 671.

Willson, R. "Three-Pion HBT Interferometry at the STAR Experiment," Ph.D. dissertation, The Ohio State University, (2002).

Wong, C.Y. "Introduction to High-Energy Heavy-Ion Collisions," *World Scientific Co. Pte. Ltd.* (1994).

Wood, L. "Transverse flow in 158 AGeV/c Pb+Pb at the CERN SPS," Ph.D. dissertation, University of California, Davis, (1998).

Zhang, B., Gyulassy, M., and Ko, C. *Physics Letters* **B455** (1999) 45.